
Position Reconstruction of Gamma-ray Interaction in Monolithic Scintillator Crystals

Faten A. Alsomali

Doctor of Philosophy

University of York

Physics

January 2021

Abstract

The localisation of the interaction position of γ rays in scintillator detectors are of interest for different applications such as nuclear medicine, astronomy, fundamental physics experiments and nuclear security. For instance, the localisation of the interaction position of gamma rays in a detector can provide information about reconstructing the actual source position such as the one used in Compton cameras meant for nuclear security. The 3D scintillator detector described in this thesis consists of a $50.44 \times 50.44 \times 50.44$ mm³ cubic CsI:Tl crystal coupled, for the first time, to six 8×8 SiPM arrays on all of the six faces of the crystal. 2D average and single light maps were generated to visualise the interaction positions. The measurements were also compared to Geant4 simulations and a simplistic geometrical model, and both showed a reasonable agreement with each other. The interaction position was successfully determined by using the light ratio method using both experimental and simulation data. Covering all of the six sides of the detector simplified the localisation and the 3D position reconstruction of the rays interaction inside the detector. All of the three coordinates were reconstructed using the χ^2 minimisation that uses the estimation based on the data of the simplistic model. The position resolution was measured at the edges and the central region of the detectors using the reconstructed data obtained from both these methods. At the edges, the resolution was found to be 1.4 mm and 2.6 mm, whereas in the central region, it was calculated to be 2.3 mm and 3.7 mm for the χ^2 minimisation and the light-sharing method respectively. The results obtained are exciting, and the interaction positions can be reconstructed using the light-sharing measurements obtained from all of the six arrays. Moreover, the position resolution can be quantified by using the reconstructed events light distribution.

Contents

List of Figures	vi
List of Tables	xvii
1 Introduction	1
1.1 Application of Scintillator Detectors	2
1.2 Position Reconstruction Methods	6
1.3 Motivation and Objectives of the Thesis	9
1.4 Outline of the Thesis	10
2 Theory and background	11
2.1 γ Rays Interaction with Matter	12
2.2 Scintillators	15
2.3 Optical Phenomena	18
2.4 Photo-detector	22
2.4.1 Photomultiplier	22
2.4.2 Semiconductor-based Photo-detectors	23
2.4.2.1 Photodiodes	23
2.4.2.2 Silicon Photomultipliers	25
2.5 Scintillator Detectors for γ ray Detection and Digital Pulse Processing	28
3 Methodology	32
3.1 Experimental set up and Measurements	33
3.1.1 1D CsI:Tl Detector	33

3.1.1.1	Detector Configuration	33
3.1.1.2	Measurements and Data Acquisition Systems	34
3.1.2	3D Cubic Detector	39
3.1.2.1	Detector Configuration	39
3.1.2.2	Data Acquisition Systems	43
3.1.2.3	Measurements	47
3.1.2.4	3D Position Reconstruction Methods	48
3.2	Geant4	51
3.2.1	Introduction to Geant4 and its Applications	51
3.2.2	General Overview of Geant4	51
3.2.3	Modeling Scintillator Detectors Using Geant4	52
3.3	Modelling 1 and 3D Detectors using Geant4	55
3.3.1	1D CsI:Tl Detector	55
3.3.2	3D CsI:Tl Detector	57
4	Results	59
4.1	1D Detector Results	60
4.1.1	Experimental Results	60
4.1.1.1	Energy Measurements	60
4.1.1.2	Position Sensitivity Measurement Methods	62
4.1.2	Simulation Results	66
4.2	3D Detector Results	70
4.2.1	Experimental Results	70
4.2.1.1	Energy Measurements	70
4.2.1.2	Experimental Average Light Maps	71
4.2.1.3	Average Light Maps of Pencil Beam Runs	71
4.2.1.4	Average Light Maps with the Coincidence Condition	75
4.2.1.5	Single Events Interactions Light Maps with the Co- incidence Condition	80
4.2.2	Simulation Results	82
4.2.3	Simplistic Model Results	87

4.2.4	Experimental vs. Simulation and Simplistic Models Results .	88
4.2.5	Position Reconstruction Methods	90
5	Discussion	101
5.1	1D Detector	102
5.2	3D Detector	106
6	Conclusion and outlook	113
	References	116

List of Figures

1.1	Illustration of the working principle of a PET scanner where a positron-emitting radioisotope is administered to patients for conducting a brain scan. The positron then annihilates to produce two 511 keV photons detected by the detectors positioned around the patients head. Reproduced from [4].	3
1.2	Illustration of the components and the working principle of a Compton camera. The camera consists of a scattering detector and an absorber detector separated by a known distance (blue cuboids). The position of the source can be reconstructed by several surface cones (green cones) that are constructed by using both the scattered and absorbed events energies E_1 and E_2 respectively. Reproduced from [10].	4
2.1	Illustration of the photoelectric effect mechanism where an incoming photon knocks out an orbital electron from the K shell, and the orbital electron becomes a photoelectron. Reproduced from [45]. . .	12
2.2	Illustration of the Compton scattering mechanism where an incoming photon knocks out an electron assumed to be at rest, which scatters with a portion of the incident photon energy.	13
2.3	Illustration of the pair production mechanism where an incoming photon with high energy ($E_\gamma \geq 1.022$ MeV) interacts with a nucleus and loses all of its energy in the process. This is followed by the creation of two particles, a positron and an electron.	14

2.4	Illustration of scintillation process for organic scintillators. In the singlet state labelled (S), the absorbed energy excites the molecules to the upper levels. The de-excited atoms from S_{10} to S_0 emit fluorescent light. The decay process that occurs between the triplet and singlet (T_1 to S_0) levels produce phosphorescence light, which can be distinguished by its longer wavelength and longer time of decay. Reproduced from [47]	15
2.5	Illustration of inorganic scintillation process. An electron is excited by an incoming photon and propagates through the material. The excited electron then moves to the conduction band, and if combined with a hole, it transits to the ground site. During this transition, if the pair passes through one of the activation excitation sites, then photons are emitted in the visible light range.	17
2.6	The image illustrates the emission intensities vs. the wavelengths for three different inorganic scintillators as well as the Quantum Efficiency as a function of wavelength for two photo-detectors. Reproduced from [48].	18
2.7	Diagram showing light reflections mechanism, absorbed and transmitted from a surface. The incident photon can be reflected from the surface in different directions (Diffusive reflection) or reflected in the same direction (Specular reflection). It can also be absorbed or transmitted out of the material. Reproduced from [49].	19
2.8	Illustration of light refracting at an interface between two media of different refractive indexes (n) and $n_2 > n_1$. When light travels from medium 1 to medium 2 with an angle, it changes its direction and speed, and the angle of refraction (θ_2) is less than the angle of incidence (θ_1).	21

2.9	Illustration of light passing from one medium to another with different refraction indexes and densities (glass to air). The first diagram (left) the incident angle (i) is smaller than the critical angle (c), whereas (middle) $i = c$ and (right) occurs when $i > c$	22
2.10	A diagram illustrating the components and the basic working principle of photomultipliers. Reproduced from [50].	23
2.11	A simple diagram illustrating a photodiode's internal structure and its circuit symbol. p^+ and n^+ represent the doped junctions and the area between labeled as (n) is the depletion region where electrons-holes are generated. Reproduced from [53].	24
2.12	Schematic structure of an SiPM micro-cell which shows the components and layers of dope combinations. The silicon (Si) resistor controls the current flow for resetting the bias and SiO_2 provides electrical and some optical isolation. The Guard ring provides a uniform electrical field across the pn junction area. Reproduced from [55].	25
2.13	An example of an SiPM that consists of $10\mu\text{m}$ micro-cells. Reproduced from [56].	26
2.14	Illustration of the equivalent electric circuit of an array of summed micro-cells and the quenching resistors that control the current flow. Reproduced from [57].	26
2.15	PDE vs. wavelength for two different overvoltages where the 5.0 V (solid black line) shows higher PDE compared to 2.5 V (dashed line). Reproduced from [57].	28
2.16	A diagram showing the digital accusation system following an analog electronic chain. The raw signals produced from the detector are amplified using the preamplifier, and the shaping amplifier filters out the noise. The signals produced are semi-Gaussian shaped, and they can be measured by an Analog to Digital Converter (ADC). Reproduced from [59].	29

2.17	An illustration of a spectroscopic system energy resolution definition. The resolution is calculated using the ratio between the FWHM and the centroid position of the peak (H_0). Reproduced from [60]	30
3.1	Examples of different wrapping materials used for the 1D scintillator detector (PTFE, 3M ESR sheet and Black tape).	34
3.2	(a) Illustration of the experimental setup for the 1D detector which is placed on a plastic holder (red). The holder along with the detector was then placed and stabilised on an xy linear drive for the xy measurements scan and (b) a schematic drawing showing where the source is located.	35
3.3	Schematic diagram showing both the SiPMs connected to a power supply and to a 16 channel CAEN V1730B digitiser. The signals were displayed on a Tektronix oscilloscope for monitoring.	36
3.4	An example of a signal recorded using a CAEN Model V1730B digitiser. The image shows the signal recorded after applying the parameters to select the correct accusation window.	37
3.5	(a) An image of the cubic CsI:Tl being measured.(b) An image of one of the 8×8 SiPM array that is coupled to one of the crystals faces for photons detection.	40
3.6	(a) The image shows two plastic 3D holders, each holding 3 8×8 SiPM arrays. (b) The image shows how the arrays are inserted inside the plastic holder. (c) The image shows the final detector configuration where all of the faces of the cubic scintillator are covered with the arrays and then wrapped with a black tape.	41
3.7	Experimental set up (a) Front image (b) top image where the main detector is placed at the left of the collimator and under the source. At the left of the slit collimator the coincidence detector is positioned to detect all Compton scattered rays events with a 90° scattering angle.	42

3.8	Illustration of the different γ -ray interaction mechanisms in a monolithic scintillator. (a) shows multiple Compton scattered events before exiting the detector. (b) shows one 90° Compton scattered event exiting the detector and (c) shows where the event deposits all of its energy (photoelectric absorption) and no Compton scattering events.	43
3.9	A schematic diagram of a left-handed coordinate system showing the collimated source hitting the middle of the main detector and scattering at 90° . The scattered γ ray then passes through the slit collimator and is detected in the coincidence detector. The diagram also shows the dimensions of each of the components of the experiment and the distances between them.	44
3.10	A schematic sketch of an individual FBEX3B card component. The FPGA is the main component used for defining the detected signal's height.	45
3.11	An image of the scanning table station and the DAQ system used for recording the events. The crates were used to power up 25 FEBEX3b cards and the SPF module. The NIM module provided the triggering condition and the SPF module.	46
3.12	A sketch of the external trigger logic was applied to the 6-sided readout. The corresponding summed SiPMs outputs from each of the preamplifier cards are seen.	47
3.13	A sketch showing the parameters used for calculating the Solid angle Ω . The source position is given by the S, and d represents the source distance from the photo-detector. The a and b symbols represent the horizontal and vertical coordinates of the photo-detector.	48

3.14	(a) shows the photon light (blue) propagating through the 1D scintillator detector model, and the yellow and white represent the SiPMs and the PTFE wrap respectively. (b) Shows the refractive index values of the materials used that are configured in the simulation code.	55
3.15	Simulated setup with dimensions comparable to the experimental setup. From left to right: coincidence detector with a single SiPM array (green-yellow) on the top surface of the crystal (blue), lead slit collimator (turquoise) and main detector with an SiPM array on each side. The γ rays from the ^{137}Cs source are illuminating the main detector from the top.	58
4.1	Energy spectrum obtained from ^{137}Cs and ^{152}Eu sources by a $6\times 6\times 76.2\text{ mm}^3$ 1D detector (see Figure 3.2 for detectors configuration). (a) Shows the PTFE-wrapped detector, (b) black-tape-wrapped detector and (c) the 3M-ESR-wrapped detector.	61
4.2	An example of the spectra measured at one end of the PTFE wrapped crystal (SiPM0, top) and the light measured by summing both SiPMs (SiPM0+SiPM 1, bottom) at different illumination interaction points along the long-axis of the 1D detector. The different colours represent the different interaction points.	63
4.3	The light ratio of the two opposite SiPMs as a function of the γ -ray interaction position for black tape (red), PTFE (blue) and 3M ESR sheet (green).	64
4.4	The Position resolution calculated at different interaction position for (blue) the 3M ESR, (orange) black tape and (black) is the PTFE wrapped detector.	64
4.5	The light ratio is plotted as a function of the γ -ray interaction position for the simulated 1D PTFE-wrapped detector. The light ratio is shown for both SiPM0 (red) and SiPM1 (blue).	66

4.6	A comparison between the experimental (blue) and the simulated (red) data for the 1D PTFE-wrapped detector (Figure 3.2 shows the detectors configuration). The image illustrates the light ratio detected at SiPM0 as a function of γ ray interaction position. . . .	67
4.7	Simulated slope value (g) as a function of surface polish (%) (crystal surface treatment). The slope was calculated by applying a linear fit at different positions for a PTFE wrapping material with 97% reflectivity.	68
4.8	The simulated light ratio obtains as a function of the γ -ray interaction position at one end of the crystal (SiPM0) for two different σ_α values of the UNIFIED model. The blue line represents the data obtained for $\sigma_\alpha=0.02$ (polished), and the red line represents $\sigma_\alpha=0.2$ (rough).	69
4.9	Energy spectrum of the main (left) and coincidence (right) detectors. The photopeaks of some of the lines of the ^{137}Cs and ^{152}Eu source are marked.	71
4.10	Average light maps for position $x = y = 25$ mm of the source for all six SiPM arrays of the main detector from the pencil beam runs. The colour scale axis represents the average value at the ADC. . . .	72
4.11	The raw experimental average light maps for SiPM 3, 4 and 6 are shown in the left column. The gain corrections obtained and applied to SiPM 3, 4 and 6 are shown in the middle column and the final obtained gain-matched light maps are shown in the right column of the figure. The light maps obtained are for pencil beam runs with the source illuminating at the middle of the detector $x = y = 25$ mm.	75

4.12	(Top) The detected energy in the coincidence detector vs. the detected energy in the main detector for position $x = y = z = 25$ mm. The cut on the coincidence events is shown with a red circle, which represents the events that scatter inside the main detector with a 90° angle. (Bottom) sketch showing the setup and indicating at which position the main detector was hit.	77
4.13	Average light maps after gain-matching applied for position $x = y = z = 25$ mm for all SiPM arrays of the main detector with the coincidence condition for the trigger and an energy cut on the coincidence events. Pixels coloured yellow represent the highest number of photons detected, whereas the blue coloured pixels denote the lowest number.	78
4.14	(left) Detected energy in the coincidence detector vs. detected energy in the main detector for position $x = 5, y = 45, z = 5$ mm. The cut on the coincidence events is pictured with a red circle. (Right) Sketch showing the position at which the main detector was hit. . .	79
4.15	Average light maps for position $x = 5, y = 45$ and $z = 5$ mm for all SiPM arrays of the main detector with the coincidence condition (gain-matching correction applied) for the trigger and an energy cut on the coincidence events.	80
4.16	The light maps obtained for a single event at position $x = 5, y = 45$ mm and $z = 5$ mm for all SiPM arrays of the main detector with the coincidence condition after gain-matching correction was applied for the trigger and an energy cut on the coincidence events.	81
4.17	The light maps after gain-matching was applied were obtained for a single event at position $x = y = z = 25$ mm for all SiPM arrays of the main detector with the coincidence condition for the trigger and an energy cut on the coincidence events. SiPM 3, 4 and 5 show more than one γ ray's hit.	82

4.18 The image illustrates the number of simulated single scattering coincidence events recorded at different positions. It also shows that the longer the path traversed by a γ ray through the main detector before being detected at the coincidence detector for different $x+z$ coordinates, the fewer were single coincidence events that were recorded. 84

4.19 Energy deposited in the coincidence detector vs. energy deposited in the main detector for simulations of the position x, y and $z = 5$ mm (top), x, y and $z = 25$ mm (middle), and x, y and $z = 45$ mm (bottom). For interactions at x, y and $z = 45$ mm, the Compton scattered events “blob” becomes less well-defined. 85

4.20 Simulated average light maps for all SiPM arrays of the main detector. The detector was hit at $x = 5$ mm, $y = 45$ mm and $z = 5$ mm (simulation coordinates $x = 0$ mm, $z = -20$ mm and $y = -20$ mm). Photons are represented in the colour code. 86

4.21 Simulated single-event light maps for all SiPM arrays of the main detector. The detector was hit on the back, left and top corner (position $x = 5$ mm, $y = 45$ mm and $z = 5$ mm). Photons are represented in the colour code. 87

4.22 The images illustrate light maps generated from a single event interaction using the Simplistic Model for (a) position x, y and $z = 25$ mm and (b) for $x = 5$ mm $y = 45$ mm and $z = 5$ mm. 88

4.23 The images show the number of photons detected at each pixel of the six 8×8 SiPM arrays obtained from the simulation (blue), experimental (red) and simplistic (green) models data for position x, y and $z = 5$. Images at the top show the arrays that are near the interaction position. The images at the bottom show the arrays that are far away from the interaction position. 89

4.24 Simulation: z (left), y (middle) and x (right) position determined from the ratio of the light deposited in the two opposite SiPM arrays. The distributions are shown for the three positions as follows: interaction at x, y and z = 5 mm (blue), x, y and z = 25 mm (red) and x, y and z = 45 mm (green). 90

4.25 The light ratio distribution calculated from the total signal from the opposite SiPM arrays at (a) x = y = z = 25 mm and (b) x = 5 mm, y = 45 mm and z = 5 mm for z (top/bottom SiPMs), y (back/front SiPMs) and x (right/left SiPMs). 92

4.26 The light ratio distribution calculated from a single pixel from opposite SiPM arrays (a) at x = y = z = 25 mm and (b) at x = 5 mm, y = 45 mm and z = 5 mm. z (top/bottom SiPM max pixel), y (back/front SiPM max pixel) and x (right/left SiPM max pixel). . . 93

4.27 Event-by-event position reconstruction for the x,y and z = 25 mm position using the coordinates obtained from each of the pairs of SiPMs. The left column is the χ^2 minimisation method using the simplistic model. The next three columns are the coordinates obtained from each pair of SiPMs. SiPM top/bottom, front/back and lift/right were obtained through the light ratio of the maximum pixel on opposite SiPMs. 95

4.28 Event-by-event position reconstruction for the x,y and z = 5 mm and x = 5 mm, y = 45 mm and z = 5 mm positions using the coordinates obtained from each pair of SiPMs. The left column is the χ^2 minimisation method using the simplistic model. The next three columns are the coordinates obtained from each opposite SiPM pairs. SiPM top/bottom, front/back and lift/right are obtained through the light ratio of the maximum pixel on opposite SiPMs. 97

4.29 Event-by-event position reconstruction for a γ -ray pencil beam entering the crystal at $x = 45$ mm and $y = 5$ mm and interacting at any depth (any z) with different reconstruction methods. The left column is the minimisation using the simplistic model. The next three columns are the coordinates obtained from each opposite SiPM pairs, i.e. SiPM top/bottom, front/back and left/right through light ratio of the maximum pixel on opposite SiPMs and through its position on the SiPM. 98

A.1 Images illustrating the 2D profiles obtained to find the beam position for the 1D detector in (a) the y and (b) the x axis. The detector was moved in 10 mm steps and the count rates were measured at different interaction positions and recorded 126

A.2 Circuit Diagram for 64 way SiPM Pre-Amplifier and Summing Amplifier 127

A.3 Illustration of an 8×8 J-series array by Sensl. The diagram also shows the dimensions of each component of the array (front, side and back). Adapted from [63] 128

A.4 An example of the spectra measured at one end of the black tape wrapped detector crystal (SiPM0,top) and the light measured by summing both SiPMs (SiPM0+SiPM1, bottom) at different illumination interaction points along the long-axis of the 1D detector. The different colours represent the different interaction point. . . . 128

A.5 An example of the spectra measured at one end of the 3M ESR wrapped detector crystal (SiPM0,top) and the light measured by summing both SiPMs (SiPM0+SiPM1, bottom)at different illumination interaction points along the long-axis of the 1D detector.The different colours represent the different interaction point 129

A.6 Number/Percentage of single coincidence events in the simulation. A longer path through the detector ($x+z$) leads to more multiple scattering events. 130

List of Tables

2.1	Types and properties of five different scintillators.	17
3.1	Properties of a CsI:Tl scintillator	33
3.2	Properties of the the CsI:Tl detector components as defined in the simulation.	56
3.3	Type and surface finish of each interfaces between two different components defined in the simulations.	57
4.1	Type of the wrapping material and the average energy resolution calculated for each material.	62
4.2	Different types of wrapping and the corresponding position resolution obtained the light-ratio distribution and the gradient from the linear fit.	65
4.3	Number of coincidence and recorded events for several x, y and z positions are summarised here. x, y and z positions are given in mm	76
4.4	Number of coincidence events for a total number of 10^{10} simulated events at different x, y and z coordinates. x, y and z are in mm. . .	83
4.5	Indicative position resolution values obtained by measuring the RMS of the light distribution for each of the reconstructed coordinates. The resolution was measured for both the χ^2 minimisation and the light ratio methods light distribution at different interaction positions.	99

Acknowledgements

I would like to thank the Ministry of Education of Saudi Arabia for the scholarship and Umm Al-Qura University for their support and the funds they provided to me to pursue my PhD degree at York University. I would also like to express my gratitude towards my supervisor, Dr Stefanos Paschalis, whose constant support and guidance in addition to his regular feedback and wonderful insights helped me a lot throughout this research. And special thanks to Professor David Jenkins for his support and gaudiness. Many thanks also to Dr Jamie Brown, for always finding time to answer my questions and for asking me stimulating questions that pushed me to explore more in my research area.

I would also like to thank Dr Pankaj Joshi for his help during the experimental work since the beginning of this project. I would also like to thank the mechanical workshop group and the technicians of the Department of physics for their help and support.

Thank you to all my colleagues in the Nuclear Physics group especially to Dr Rubena Binti Yusoff for her friendship, lovely support and the encouragement provided on a daily basis, Dr Luke Morris for the productive chats whereby he shared his knowledge and Rehab Yajzey for her motivating me with her kind words.

A big thank you to my close friends Dr Ashjan Bamahfouz and Dr Noheir Taha who were always there for me. I am sincerely grateful and thankful to my dearest friend Prof. Alia Abdullah Aljindi who always believed in me and encouraged me to be where am today.

I am grateful to my family in the UK and Saudi Arabia for their prayers, love

and support. I could not have completed this project without them. A special thank you to my Aunt Nimo Goth for being by my side as solid as a rock; her unquestioned support during this project and beyond has been precious.

Finally, my biggest and deepest expression of gratitude is towards my mother, Zohour Alsomali, for her unconditional love and prayers and for the reassuring chats had with her during which she never failed to tell that I will make it.

Declaration

The submission of this thesis for the degree of Doctor of Philosophy is in accordance with the regulations of the University of York. The work contained herein has not been previously submitted for any other degree or qualification. I declare that the work presented herein is my own, and where other sources of information have been used, they have been clearly marked and referenced. The experimental work outlined in this thesis was carried out by the author under the supervision of Dr Stefanos Paschalis. The simulation codes used in this work have been optimised and changed as advised by Dr James Brown, Dr Ina Syndikus¹ and Dr Sebastian Heil codes.

Signed

Faten A. Alsomali

Chapter 1

Introduction

This chapter briefly describes the use of scintillator detectors. The different applications that benefit from these detectors have been mentioned in Section 1.1. In Section 1.2, the different position reconstruction methods that are used to localise γ rays interactions inside the crystals volume are discussed. The research motivation and thesis objectives have been stated in Section 1.3, and the thesis outline has been presented in Section 1.4.

1.1 Application of Scintillator Detectors

The need for scintillator detectors is increasing in many fields such as nuclear medicine, astronomy, nuclear physics research and nuclear security. In the medical field, for instance, scintillator detectors are used in the devices meant for clinical and small animal imaging procedures/techniques like Positron Emission Tomography (PET) and Single Photon Emission Computed Tomography (SPECT). PET is used to trace and localise the positrons that are produced from the radioactive tracer admitted into a specific organ for diagnostic or therapeutic purposes. The positrons then annihilate inside the targeted organ and produce two photons (each with 511 keV energy) that then travel in opposite directions as shown in Figure 1.1. These photons are then detected by the detectors, and images of the organ of interest get produced by reconstructing the line of response. PET and SPECT can be used for identifying diseases such as soft tissue sarcoma [1] or central nervous system's infections such as the Lyme disease [2]. These techniques can also be used for small animal imaging research such as imaging the brain metabolism process in the diagnosis of Alzheimer's disease [3].

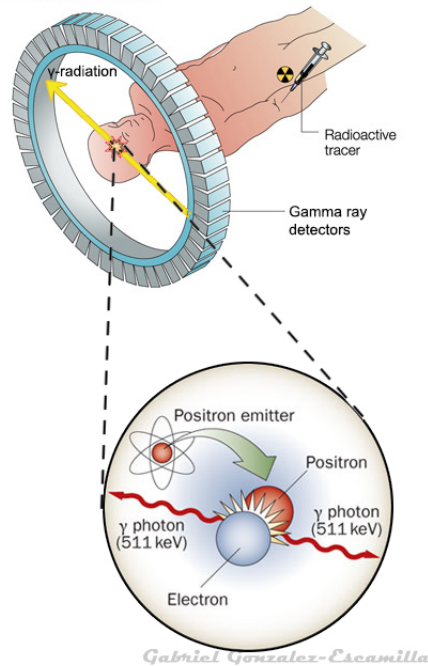


Figure 1.1: Illustration of the working principle of a PET scanner where a positron-emitting radioisotope is administered to patients for conducting a brain scan. The positron then annihilates to produce two 511 keV photons detected by the detectors positioned around the a patients head. Reproduced from [4].

Pixelated scintillators such as lutetium-yttrium oxyorthosilicate (LYSO) coupled to silicon photomultipliers are used for detecting γ rays and for localising the source position [5]. Detectors based on LYSO scintillators in PET imaging systems can also be used for brain PET scanners or can be integrated with other imaging models such as Magnetic Resonance Imaging (MRI) [6] [7]. SPECT imaging systems use γ -ray-emitting isotopes that are administered to a patient's body. The SPECT camera rotates around the patient's body and reconstructs an image of the γ -ray distribution. Scintillator detectors used in such systems must be dense, produce a large number of photons for each single γ ray (higher light yield) and have a short decay time. NaI(Tl) scintillator detectors are widely used in SPECT due to their low costs. These types of detectors, in large sizes, can be used for an Anger camera imaging system used in SPECT [8]. Some studies have reported on the characterisation and development of a phoswich detector using LYSO/YSO or LYSO/GAGG scintillators [9]. These types of scintillators are more dense,

1.1. Application of Scintillator Detectors

brighter and exhibit shorter decay times than NaI(Tl) scintillators which increase the SPECT detector sensitivity.

In the area of nuclear security, the need for monitoring and identifying hazardous materials has motivated many studies to develop and characterise new high-performance detectors for both γ rays and neutron detection systems. Compton Gamma cameras (CGC) are one of the many detection systems that can be used for homeland security. These cameras have two types of detectors, a scattering detector and an absorber detector as seen in Figure 1.2. For coincidence events, a γ ray interacts with the first detector which is less dense and scatters via the Compton scattering interaction to the second detector. The second detector is more dense and absorbs the photons via the photoelectric interaction. The source position can then be reconstructed by knowing the position of the photons interaction and the energies deposited in the detectors.

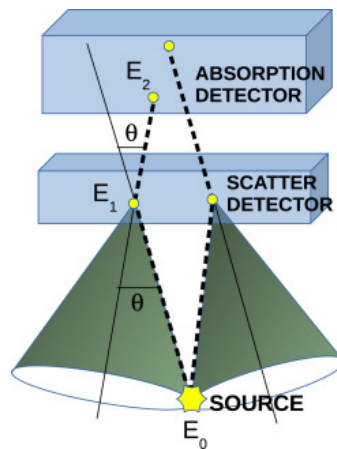


Figure 1.2: Illustration of the components and the working principle of a Compton camera. The camera consists of a scattering detector and an absorber detector separated by a known distance (blue cuboids). The position of the source can be reconstructed by several surface cones (green cones) that are constructed by using both the scattered and absorbed events energies E_1 and E_2 respectively. Reproduced from [10].

Although different types of detectors such as semiconductor detectors can be used in the design of a Compton camera, the scintillator-based detectors are relatively low in cost. They can also be manufactured in different sizes and shapes, which is an attractive choice for small compact detectors that can be used for handheld Compton camera devices [11] [12].

As mentioned earlier, the applications of scintillator detectors also include astrophysical research. In the oil and gas industry, scintillator detectors play an important role in measuring the formation of the soil surroundings. The measurements obtained from the detectors can be used for identifying petrophysical parameters, hydrocarbons and mineralogical structures depending on the type of the detected radiation [13].

The time-of-Flight (TOF) and particle tracking measurements carried out for nuclear experiments such as those related to the nuclear structure and particle physics utilise different scintillator detectors in their detection systems [14]. These include the use of plastic scintillators for beam counting systems and TOF measurements [15] because of their fast decay time. In experiments where a moving γ -ray source is detected at different positions and velocities, the measurements suffer from the Doppler effect. This causes a broadness in the spectra, which degrades the energy resolution. The use of a position sensitive scintillator detector can correct for such an effect using an event-by-event analysis [16].

In this project, the detector that has been developed is based on a CsI:Tl scintillator which is low in cost, high in density and slightly hygroscopic. It is broadly used in nuclear safety and nuclear medicine applications [17] [18]. It is also used in imaging instruments such as γ -ray Compton cameras for measuring angular and directional resolutions that are, in turn, used for reconstructing the actual source position [19] [20].

1.2 Position Reconstruction Methods

There are many radiation detectors that are used for position- sensitivity measurements. The detectors used for such measurements include silicon-strip detectors for detecting charged particles [21] or germanium-tracking-array detectors that can be utilised for γ - ray tracking for in-beam nuclear experiments [22]. Given the need for simplifying the designs of a radiation detection system for many different applications, including those where position-sensitivity measurements are crucial, many researchers have utilised scintillator detectors. For example, High-purity Germanium (HPGe) detectors require to be cooled down using liquid nitrogen to reduce the noise that can affect the energy resolution.

Segmented scintillator detectors such as those used in some Compton camera systems provide 2D- and 3D-interaction position images [23] [24]. However, the use of such detectors increases the complexity and cost of designing them. An alternative approach that can overcome these limitations is the use of a monolithic scintillator detector [25] [26].

There are several position reconstruction methods that have been reported over the years that utilise monolithic scintillator detectors. The early methods such as the centroid and Anger logic approaches were developed for 2D position reconstruction [27] [28]. The use of such algorithms were limited to localising the interaction position on the X and Y axes with no Depth of Interaction Information (DOI). Moreover, the abilities of these methods to reconstruct the interaction positions were degraded at the edges of the detector. The alternative methods that were developed integrated the third dimension (z) which represents the size of the scintillator volume and interactions along that axis.

In general, the process of extracting 3D interaction position information can be carried out by measuring the scintillation light distribution that is detected by the photodetectors. Although several different fields benefit from the DOI reconstruction techniques, the majority of the literature published on this subject

focuses on the medical imaging field (e.g. PET) [29] [30]. A double-sided readout can be used for extracting the DOI information by building lookup tables that relate the light distribution detected inside the crystal by the photosensors to the scintillation position [31].

Estimating DOI can also be achieved by using the analytical fit models for localising event-by-event γ -ray interactions such as the one described in [32], which implements the inverse square law and an exponential factor. This model was later modified by adding the intensity of the scintillation light reflected inside the detector [33]. The algorithms based on machine learning such as the Artificial Neural Network (ANN) [34], Gradient Tree Boosting (GTB) [35] and Deep Neural Networks (DNNs) [36] are considered new algorithms for 3D position reconstruction. However, these algorithms require long training periods to obtain information such as that related to the interaction position.

These other approaches compare the distribution of an unknown light generated inside the crystal to predefined light distributions at different positions to reconstruct the DOI coordinates. This can be carried out by fitting the light distribution with different statistical methods such as the Chi-square method (χ^2) [37] and Maximum Likelihood (ML) [38]. Although these methods reacquire long and time-consuming measurements for constructing the reference points, the fitting process does not depend on predictions such as the analytical approach. The former approach extracts the DOI positions by utilising practical information provided by light distribution such as the width of the distribution.

The reconstruction of the 3D coordinates of the γ -ray interactions inside the crystal and the estimation of the position resolution depend on the size, type of the scintillator crystal, detector configuration and the methodologies applied. For instance, the best position resolution measured for a $50 \times 50 \times 30$ mm³ thick crystal using the K-Nearest Neighbours (K-NN) method was found to be 4.5 mm FWHM at 662 keV in the x and y direction [39]. For DOI measurements (z-coordinates), 1.9 mm and 2 mm position resolutions were obtained using $42 \times 42 \times 10$ mm³ LSO

1.2. Position Reconstruction Methods

and $50 \times 50 \times 4$ mm³ LaBr₃ scintillators [40] [41]. Looking at thicker crystals, In Ref [42], the DOI resolution for a $50 \times 50 \times 20$ mm³ LYSO scintillator was found to be 5 mm. This indicates that localising the depth of the γ -ray interactions inside the crystal degrades as the thickness of the crystal increases.

1.3 Motivation and Objectives of the Thesis

The information obtained from the DOI is important for solving some of the limitations of the detection systems. One such limitation is the Parallax error which affects both the sensitivity of the detectors used, for instance, in small animal PET imaging systems [43] and their spatial resolutions. The localisation of the DOI for charge-coupled detectors that are used for γ -ray cameras improve the spatial resolution that is affected by the scintillator's thickness. [44]. Such limitations have motivated the current research to focus on building and characterising a new position-sensitive detector. Moreover, the need for cost-effective, small-in-size and less time-consuming 3D reconstructing methods drive future research and developments in improving position-sensitive monolithic detectors. The aim of this thesis is to construct a position-sensitive monolithic detector using a low-cost inorganic scintillator. The goal is also to characterize the detectors sensitivity performance by implementing 3D position reconstruction methods that can be used for different applications.

In summary, the objectives of this thesis are to:

- Construct and characterise new position-sensitive scintillator detectors for γ -ray detection.
- Testing different position reconstruction methods to locate γ -ray interactions inside the detector volume.
- Develop a simulation and an analytical model for estimating the scintillation light distribution in the monolithic scintillator.

1.4 Outline of the Thesis

Chapter 2 describes the interaction of γ rays with matter, the different types of scintillators and the scintillation processes. The optical phenomena that describe the behavior of the light generated inside the scintillator and the different photodetectors that are used to detect the light have also been discussed in this chapter. Further, this chapter details how scintillator detectors operate along with providing a brief description on digital signal processing. In Chapter 3, the experimental set up for both the detectors has been described. Measurements and calculations on energy and position resolution have also been detailed in this chapter, and the methods of 3D position reconstruction have been described. The modelling of the 1D and 3D using the Geant4 simulation models has been presented and explained. Chapter 4 presents the results obtained from the detector measurements and the simulation models. In Chapter 5, the results are discussed and explained. The conclusion deriving from the project and suggestions for future research have been stated in Chapter 6.

Chapter 2

Theory and background

In this chapter, Section 2.1 discusses the theory and background of the mechanism of γ -ray interactions with matter. In Section 2.2 the different types of scintillators and their different scintillation processes have been discussed. The behaviour of the generated light inside the scintillator and the different mechanisms that occur at the boundaries have been discussed in Section 2.3, whereas in Section 2.4 the different photo-detectors that are used for detecting scintillation light have been discussed and reviewed. Finally, in Section 2.5 a brief description of how the scintillator detectors operate and an example of digital signal processing have been discussed.

2.1 γ Rays Interaction with Matter

Although there are several mechanisms for interaction of γ rays with matter, the three most common interactions are photoelectric absorption, Compton scattering and pair production. The photoelectric absorption dominates at low energies ($= < 200$ keV), and it is proportional to the atomic number Z^5 . When a photon interacts with a bound atomic electron, it transfers all of its energy to the freed electron which escapes its orbit as illustrated in Figure 2.1. As a result of this transformation, a photoelectron (PE) is produced, and its kinetic energy is given by:

$$E_e = E_\gamma - E_b \quad (2.1)$$

where E_e is the electron's kinetic energy produced, E_γ is the energy of the incident photon and E_b is the binding energy between the electron and the nucleus.

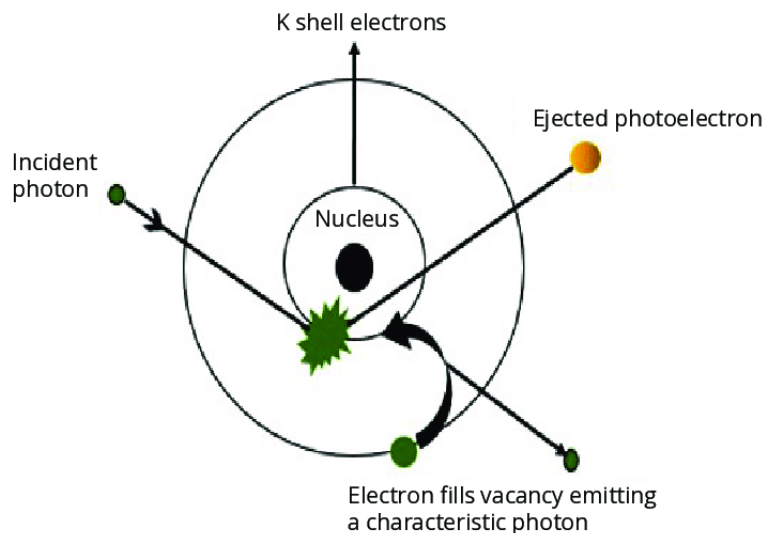


Figure 2.1: Illustration of the photoelectric effect mechanism where an incoming photon knocks out an orbital electron from the K shell, and the orbital electron becomes a photoelectron. Reproduced from [45].

At higher energies (200 keV to 1.5 MeV), the Compton scattering (CS) mechanism dominates and is independent of the atomic number. The incident photon

2.1. γ Rays Interaction with Matter

interacts with an electron and partially transfers its energy to that electron. (Figure 2.2). The photon is then scattered from its original trajectory by an angle where both the energy deposited and the scattered photon can be linked by the following equation:

$$E'_\gamma = \frac{E_\gamma}{\left(1 + \frac{E_\gamma}{m_e c^2}\right)(1 - \cos \theta)} \quad (2.2)$$

where

- E'_γ : Energy scattered γ ray
- E_γ : Energy incident γ ray
- $m_e c^2$: Rest mass of electron
- θ : Scattering angle of the photon with E'_γ energy

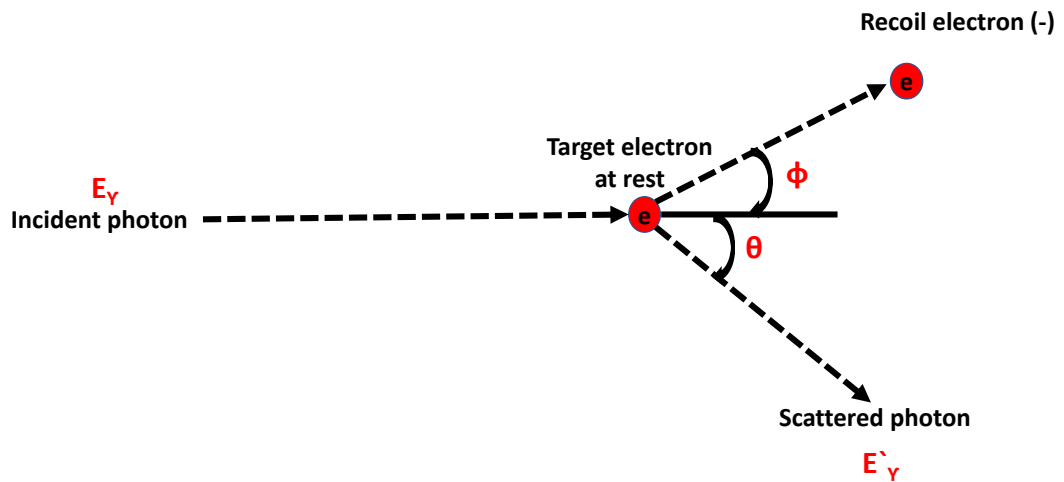


Figure 2.2: Illustration of the Compton scattering mechanism where an incoming photon knocks out an electron assumed to be at rest, which scatters with a portion of the incident photon energy.

2.1. γ Rays Interaction with Matter

In the cases of the above interactions, the incident photon interacts with an orbital electron of the atom. However, when the γ -ray energy exceeds 1.022 MeV, pair production occurs when the photon interacts with the electric field of the nucleus producing a pair of an electron and positron as shown in Figure 2.3. The kinetic energy of the electron E_{e^-} and positron E_{e^+} that is produced is equal to the difference between the energy of the incoming photon E_γ and is equivalent to the energy of two electron masses as shown in the following equation:

$$E_{e^+} + E_{e^-} = E_\gamma - 1.022[\text{MeV}] \quad (2.3)$$

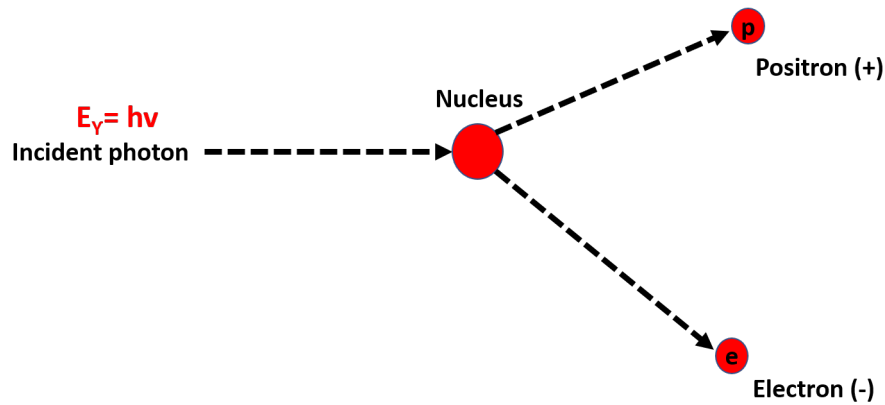


Figure 2.3: Illustration of the pair production mechanism where an incoming photon with high energy ($E_\gamma \geq 1.022$ MeV) interacts with a nucleus and loses all of its energy in the process. This is followed by the creation of two particles, a positron and an electron.

2.2 Scintillators

Scintillators can be found in different shapes, sizes and material types. When a γ ray interacts with a scintillator, one of the three methods mentioned above take place, and some of this energy is converted into visible or near UV range photons. This mechanism is known as the scintillation process, and the number of photons produced is proportional to the energy deposited in the crystal by the γ rays. There are two types of scintillators, organic and inorganic, and they have different scintillation processes, sensitivity and detection efficiency.

Organic scintillators are aromatic hydrocarbons that can be found in the forms of crystals, solid, liquids and plastics [46]. Figure 2.4 illustrates the scintillation mechanism when a particle interacts with an organic material.

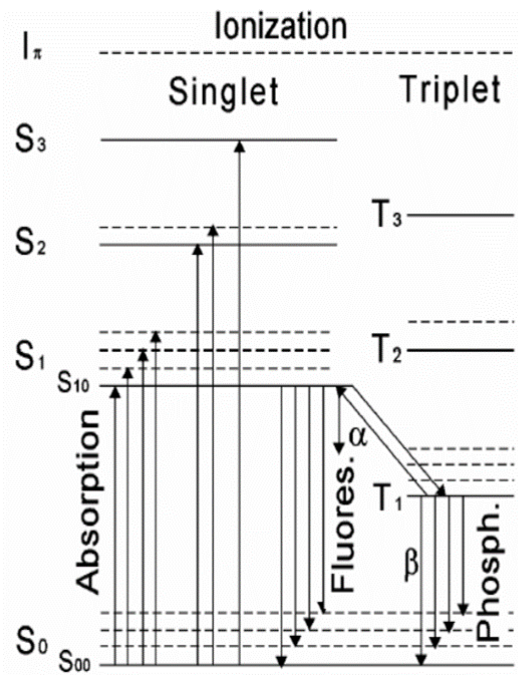


Figure 2.4: Illustration of scintillation process for organic scintillators. In the singlet state labelled (S), the absorbed energy excites the molecules to the upper levels. The de-excited atoms from S_{10} to S_0 emit fluorescent light. The decay process that occurs between the triplet and singlet (T_1 to S_0) levels produce phosphorescence light, which can be distinguished by its longer wavelength and longer time of decay. Reproduced from [47]

When a particle passes through the crystal, the atoms of the molecules are excited from the S_0 ground level to the higher levels. In some cases where the frequencies are less than 10^{13} or 10^{14} Hz, an electron in the triplet state decays back to the T_1 state through a radiationless transition. They can then transit to the ground S_0 and produce the excess energy in the form of optical photons in the singlet state. Molecules that are excited from the triplet states can produce fluorescence or phosphorescence lights where the later can be identified by its longer wavelength. Depending on the emission time if the re-emission of the photons is from 10^{-9} S to 10^{-6} S, the process is called fluorescence. But if the re-emission is between 10^{-3} S and 100 S for transitions from T_1 to S_0 the process is called phosphorescence. The non-radioactive decay process can occur for transitions that take place between S_1 to S_0 for emission times between 10^{-7} S and 10^{-5} S. Other processes such as inter-system crossing, vibrational relaxation, internal conversion and light absorption occur for time emissions that are $\leq 10^{-6}$ S.

Organic scintillators show fast decay time compared to inorganic scintillators, but due to their lower density and atomic numbers, more material is needed to stop high energy γ rays (up to 15 cm thickness).

Inorganic scintillators are high in density, light yield and atomic number (Z) compared to the organic scintillator. The scintillation process in this type of crystals does not depend on the molecules energy transition between different energy states but on the characteristics of the electron band structure of the crystal [46]. Figure 2.5 illustrates the scintillation process when an incoming particle interacts with an inorganic scintillator and scatters an e^- with high kinetic energy. As this e^- slows down via energy loss, it transfers energy to the crystal and excites more electrons in the process. As the electrons fall back to the valance to recombine with a hole, visible light is emitted. When an electron propagates through the crystal, it may be absorbed or captured depending on the purity of the material. Most inorganic crystals are doped with activators that introduce sites of impurities in the crystal lattice. These sites are important to produce optical photons, resulting

2.2. Scintillators

from the de-excited electron in the visible spectrum from such sites [47].

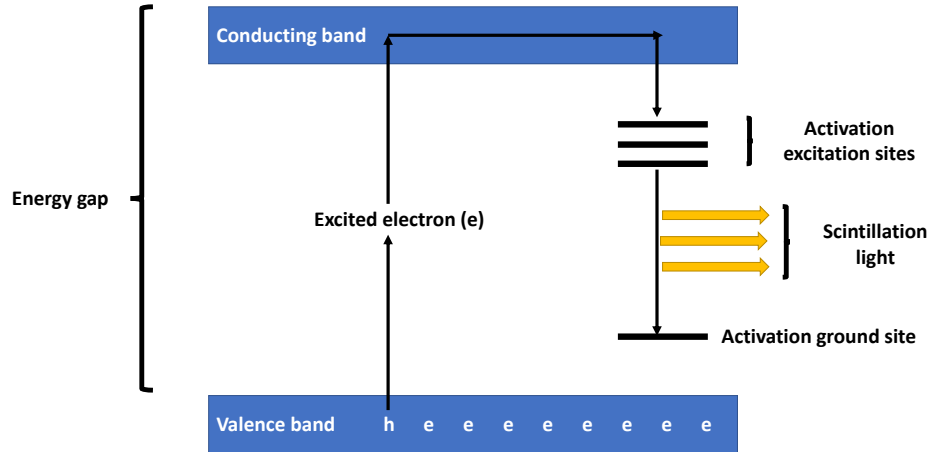


Figure 2.5: Illustration of inorganic scintillation process. An electron is excited by an incoming photon and propagates through the material. The excited electron then moves to the conduction band, and if combined with a hole, it transits to the ground site. During this transition, if the pair passes through one of the activation excitation sites, then photons are emitted in the visible light range.

One drawback of this type of material is that some of the inorganic scintillators used are hygroscopic and have to be managed in a sealed tight enclosure. Table 2.1 illustrates different types of scintillators and their properties.

Table 2.1: Types and properties of five different scintillators.

Scintillator	CsI:Tl	CsI:Na	CeBr ₃	LYSO:Ce	LaBr ₃ :Ce
Density, g/cm^3	4.51	4.51	5.2	7.1	5.1
Light yield, ph/Mev	54000	41000	60000	32000	63000
Hygroscopic	slightly	yes	yes	no	yes
Decay time, ns	1000	630	17	40	16
Refractive Index	1.79	1.84	2.09	1.81	1.9
Typical cost for $1 \times 1 \times 1$ inch, £	300	300	2000	2000	3000

2.3. Optical Phenomena

Another important property of scintillators is the scintillation emission spectrum intensity that varies depending on the type of the scintillator used and also on the type of impurities added to the crystal. Figure 2.6 illustrates the emission intensity as a function of the wavelength for different inorganic scintillators and two types of photo-detectors. This type of spectra provide important information that helps to ensure that the wavelengths of the photon lights generated inside the crystal match with the wavelengths detected by the chosen photo-detector.

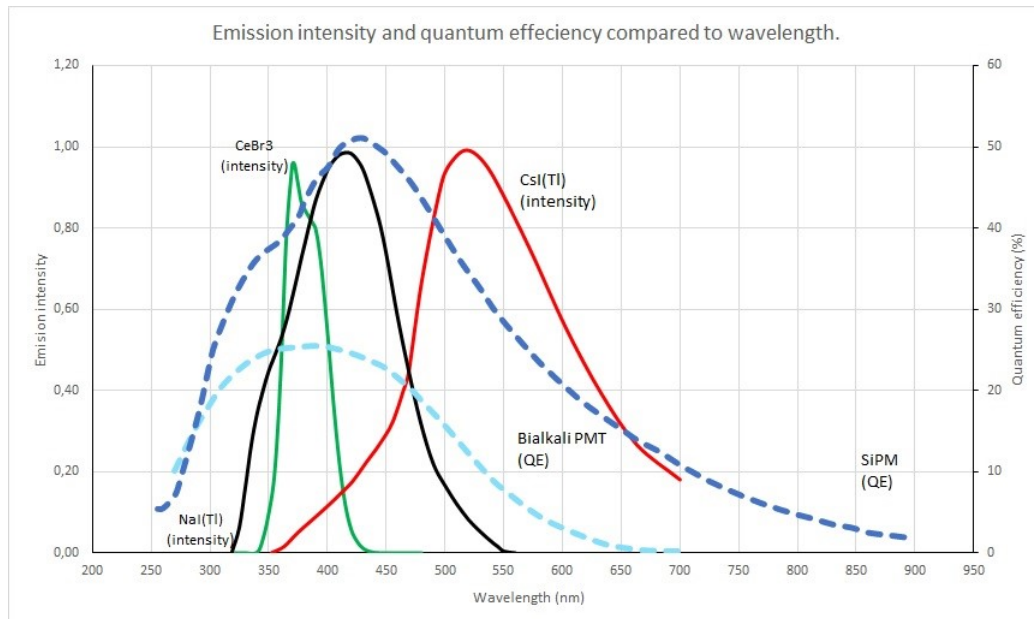


Figure 2.6: The image illustrates the emission intensities vs. the wavelengths for three different inorganic scintillators as well as the Quantum Efficiency as a function of wavelength for two photo-detectors. Reproduced from [48].

2.3 Optical Phenomena

The scintillation photons that are emitted following the γ -ray interaction with the scintillator can go through different processes which are the following:

- Reflection: This is the phenomenon that depends on the type of the surface

that the light reflects from. Mirror-like surfaces show that:

$$\theta_1 = \theta_2 \quad (2.4)$$

where θ_1 is the angle of the incident ray that is measured between the ray and a line normal to the surface that intersects the surface at the same point as the ray, and θ_2 is the angle of the reflected ray that is measured from the reflected ray to the surface normal. The latter mechanism is known as the specular reflection, and the light rays that reflect from a rough surface and scatter in all directions are known as diffusive reflection. This is illustrated in Figure 2.7.

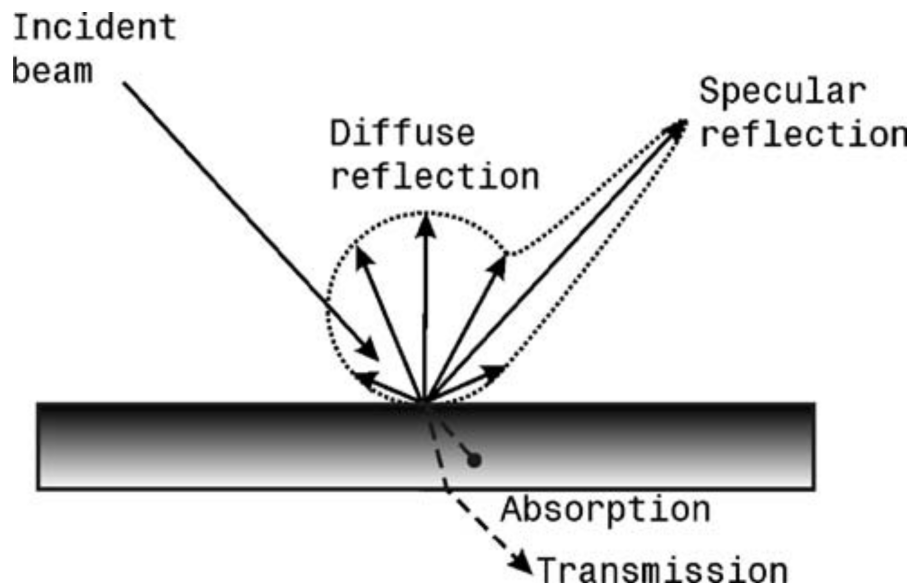


Figure 2.7: Diagram showing light reflections mechanism, absorbed and transmitted from a surface. The incident photon can be reflected from the surface in different directions (Diffusive reflection) or reflected in the same direction (Specular reflection). It can also be absorbed or transmitted out of the material. Reproduced from [49].

- Refraction: This is the change of direction when the speed of the photons changes as they travel from one medium to another as shown in Figure 2.8.

This phenomenon can be explained quantitatively by using Snell's law as follows:

$$\frac{n_1}{n_2} = \frac{\sin \theta_2}{\sin \theta_1} \quad (2.5)$$

where θ_1 , θ_2 are the incidence angle and refraction angle respectively. The angle of incidence is measured between the incidence angle ray and the normal line (a perpendicular line to the surface at the point of incident). The refraction angle is the angle the refracted ray makes with the normal line. The n symbol is known as the refractive index that is given by:

$$n = \frac{c}{v} \quad (2.6)$$

where c is the speed of light in vacuum and v is the speed of light in material. Reflection and transmission of light at an interface can also be described by Fresnel's law. The law is used to calculate the power of the light reflected or transmitted for both parallel (\parallel) and perpendicular (\perp) to the plane of incidence. The description of the wave's geometrical orientation is known as the polarisation state. There are two states which are the S polarization which describes the wave's electrical field that is normal to the plane's polarisation and the P polarisation that represents the polarisation of the electrical field in the plane of incidence. They can be estimated using reflection (ρ) and transmission (τ) coefficients with the help of the following expressions:

$$\rho_{\parallel} = -\frac{\sin(\theta_i - \theta_t)}{\sin(\theta_i + \theta_t)} \quad (2.7)$$

$$\rho_{\perp} = \frac{\tan(\theta_i - \theta_t)}{\tan(\theta_i + \theta_t)} \quad (2.8)$$

$$\tau_{\parallel} = \frac{2n_1 \cos \theta_i}{n_2 \cos \theta_i + n_1 \cos \theta_t} \quad (2.9)$$

$$\tau_{\perp} = \frac{2n_1 \cos \theta_i}{n_1 \cos \theta_i + n_2 \cos \theta_t} \quad (2.10)$$

2.3. Optical Phenomena

The angles of the reflected and transmitted light at an interface boundary are given by θ_i and θ_t respectively. The power of the reflected (R) and transmitted (T) lights for both (\parallel) and (\perp) polarisation can be calculated using the following equations:

$$R = | \rho^2 | \quad (2.11)$$

$$T = \left[\frac{(n_2 \cos(\theta_t))}{(n_1 \cos(\theta_i))} \right]^2 t^2 \quad (2.12)$$

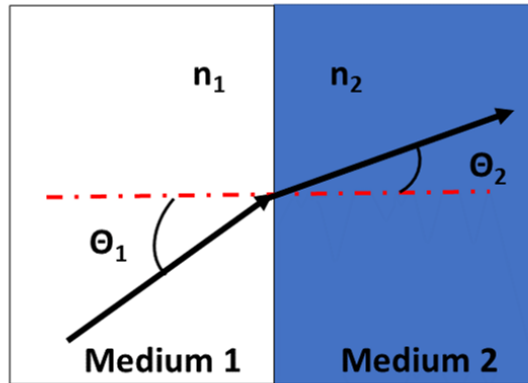


Figure 2.8: Illustration of light refracting at an interface between two media of different refractive indexes (n) and $n_2 > n_1$. When light travels from medium 1 to medium 2 with an angle, it changes its direction and speed, and the angle of refraction (θ_2) is less than the angle of incidence (θ_1).

- Total internal reflection: This optical phenomenon depends on the critical angle that can be calculated based on Equation 2.6 by selecting the refracting angle to be 90° :

$$\sin \theta_c = \frac{n_2}{n_1} \quad (2.13)$$

where θ_c is the critical angle, and there are two conditions for it to occur:

- The optical photons that are only considered for this process are those that travel from a medium having higher density to a less dense medium.
- θ_i must be larger than the θ_c .

2.4. Photo-detector

Figure 2.9 shows an example of the different light behaviour that can occur when photons reach a boundary between two media (glass and air).

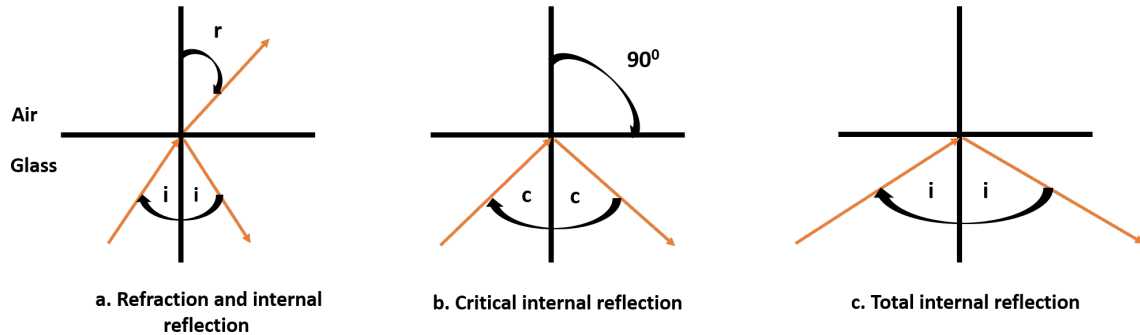


Figure 2.9: Illustration of light passing from one medium to another with different refraction indexes and densities (glass to air). The first diagram (left) the incident angle (i) is smaller than the critical angle (c), whereas (middle) $i = c$ and (right) occurs when $i > c$.

2.4 Photo-detector

2.4.1 Photomultiplier

One of the most commonly utilised photo-sensors in many applications is the Photomultiplier Tube (PMT). The PMT is a vacuum tube that consists of a photocathode, multiple dynodes and an anode and they are all encapsulated inside an evacuated glass vessel. The optical photons pass through the input glass window and hit the cathode. This excites the cathode electrons, and photoelectrons are produced, but they are not enough to produce a current flow through the tube. To overcome this issue a focusing electrode is used to direct the photoelectrons to the first dynode where they are accelerated due to the presence of the electric field. At each dynode the photoelectrons are multiplied, and they continue to produce more secondary photoelectrons until they are detected at the anode to output the current. Figure 2.10 illustrates the components and the basic working principle of a PMT.

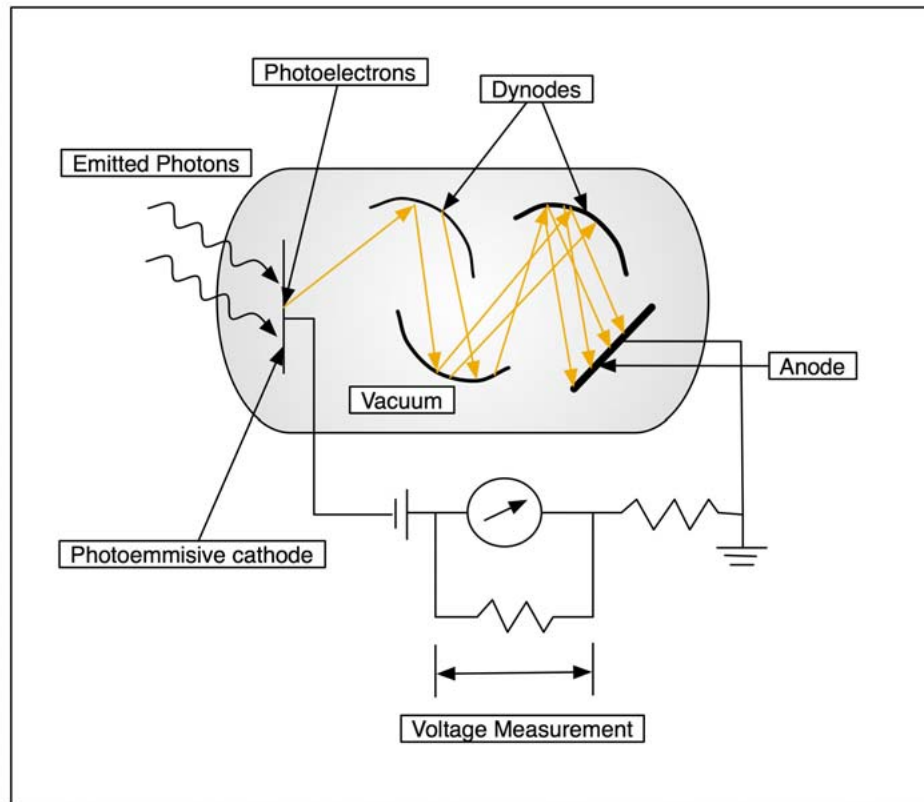


Figure 2.10: A diagram illustrating the components and the basic working principle of photomultipliers. Reproduced from [50].

Although PMTs provide high gain, large detection area, good signal-to-noise ratio and low dark current [51], they suffer from low quantum efficiency (QE) and high operating voltage, and they are sensitive to electromagnetic fields [52].

2.4.2 Semiconductor-based Photo-detectors

2.4.2.1 Photodiodes

A photodiode is a semiconductor that consists of two doped junctions known as p and n that form a depletion region as shown in Figure 2.11. If a photon strikes the photodiode and is absorbed in the depletion region, a pair of electron-holes is created. The presence of an electric field in the depletion region moves the holes towards the cathode, and the electrons towards the anode. As a result, a current

is produced which is proportional to the number of photons detected.

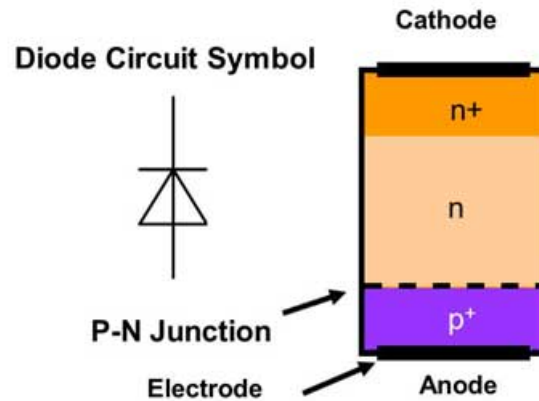


Figure 2.11: A simple diagram illustrating a photodiode's internal structure and its circuit symbol. p^+ and n^+ represent the doped junctions and the area between labeled as (n) is the depletion region where electrons-holes are generated. Reproduced from [53].

Other types of photodiodes include PIN photodiodes and Avalanche Photodiodes (APD). The operational principles of both are similar to the photodiode, but they are more sensitive and provide faster response time. The PIN photodiode provides a larger depletion area by applying an extra undoped semiconductor layer which, as a result, increases the active area. One drawback is that the signals produced by the PIN photodiode are not amplified, and the detection of low energy photons becomes more difficult. APDs were developed to overcome this issue by applying a high external voltage which increases the velocity of the electrons towards the depletion region. This increases the number of pairs produced in the region and causes an avalanche of sorts. Due to this process, the signals are amplified, and they allow for low number of photons to be detected.

APDs are small in size, insensitive to magnetic fields and provide a higher quantum efficiency but lower gain compared to PMTs. Moreover, temperature and reverse bias must be controlled when using APDs where these two factors can lead to fluctuation in the gain [54].

2.4.2.2 Silicon Photomultipliers

With the development of new photo-sensors over the past few years, Silicon Photomultipliers (SiPMs) have shown promising results as an alternative sensor to PMTs. SiPMs are semiconductors that have the same high gain as PMTs but require a lower voltage to operate.

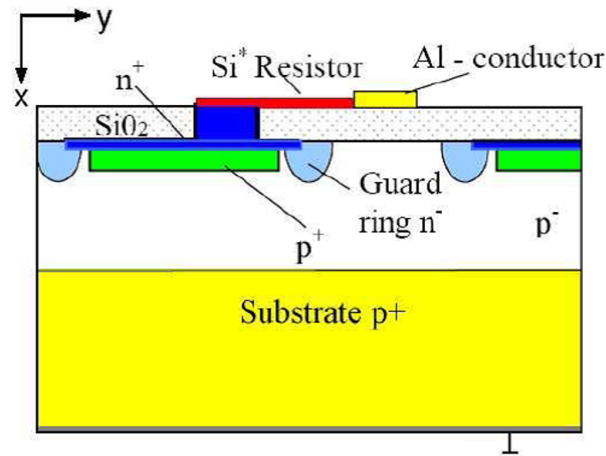


Figure 2.12: Schematic structure of an SiPM micro-cell which shows the components and layers of dope combinations. The silicon (Si) resistor controls the current flow for resetting the bias and SiO₂ provides electrical and some optical isolation. The Guard ring provides a uniform electrical field across the *pn* junction area. Reproduced from [55].

SiPMs consist of individual Geiger Avalanche Photodiodes (G-APD) known as micro-cells that are connected in parallel as shown in Figures 2.13 and 2.14. The G-APD are APDs operate in Geiger-mode above the breakdown voltage, and their operating voltage can be given by:

$$V_{bias} = V_{br} + \Delta V \quad (2.14)$$

where V_{br} is the breakdown voltage which is the minimum voltage required to generate a high-enough electric field for G-APD to avalanche. The ΔV is the applied overvoltage above the V_{br} . This gives rise to the gain, and the electric

2.4. Photo-detector

field which excites the electrons and holes and the avalanche process occur, and the G-APD discharges. The current continues to flow throughout the G-APDs as long as the bias voltage is above the breakdown voltage. A quenching resistor is added in the series along with the G-APDs as shown in Figure 2.14. This is done to control the flow and allow enough time for the G-APDs to recharge and reset the bias.

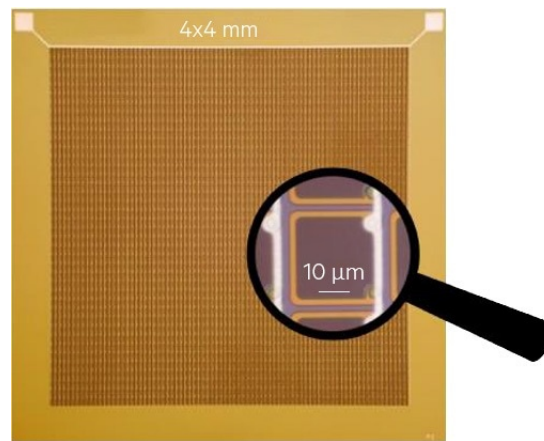


Figure 2.13: An example of an SiPM that consists of $10\mu\text{m}$ micro-cells. Reproduced from [56].

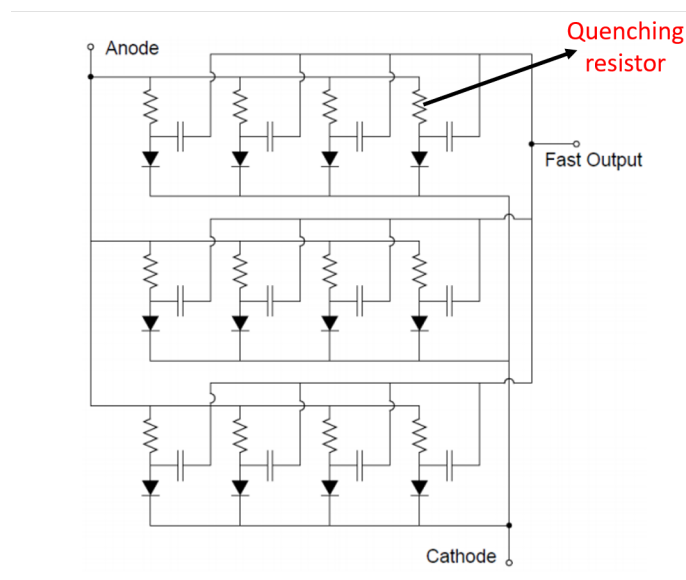


Figure 2.14: Illustration of the equivalent electric circuit of an array of summed micro-cells and the quenching resistors that control the current flow. Reproduced from [57].

The parameters that evaluate the performance of an SiPM can be summarised as follows:

- The gain which depends on the number of charges released for each photo-electron produced.
- Dark count rate (noise) produces measurable pulses that arise from thermally excited electrons and are effected by the temperature and the size of the active area.
- Optical cross talk is another source of noise that can affect the accuracy of real pulses measurements. When a G-APD is discharged, this can cause another discharge in one of its neighbouring G-APDs.
- Afterpulsing occurs when a discharged current is captured in the silicon lattice and re-released and recorded. The time of the delay of afterpulses characterises the level of impact on the measurements.

The performance of an SiPM is also evaluated by its Photon Detection Efficiency (PDE). This is an important parameter that defines the sensitivity of the SiPM to detect photons and includes the insensitive areas that are located between the micro-cells. However, the number of photons that interact with micro-cells are not equal to the number of avalanches produced. This is why the PDE parameter is used to calculate the percentage of light detected by the SiPM, and it is given as :

$$\epsilon = QE \times \epsilon_G \times \frac{A_{pixels}}{A_{total}} \quad (2.15)$$

where QE is the Quantum Efficiency which measures the probability of converting a photon to photo-electrons, ϵ_G is the probability of an electron-hole pair to be created and an avalanche being induced in the micro-cell, and $\frac{A_{pixels}}{A_{total}}$ is known as the fill factor and represents the ratio between the active and the total area of the

SiPMs. Figure 2.15 shows an example of the effect of two overvoltage values on the PDE curve. This indicates that the G-APD efficiency increases by increasing the overvoltage bias which, as a result, provides higher PDE values. However, Figure 2.15 also shows that the PDE depends on the photons wavelengths that interact with the SiPMs and that at wavelengths approximately higher than 450 nm, a decrease in the PDE can be observed. The SiPM's compactness, insensitivity to magnetic fields and the fact that it could come in different sizes makes it an ideal choice for light photon detection in many fields [58].

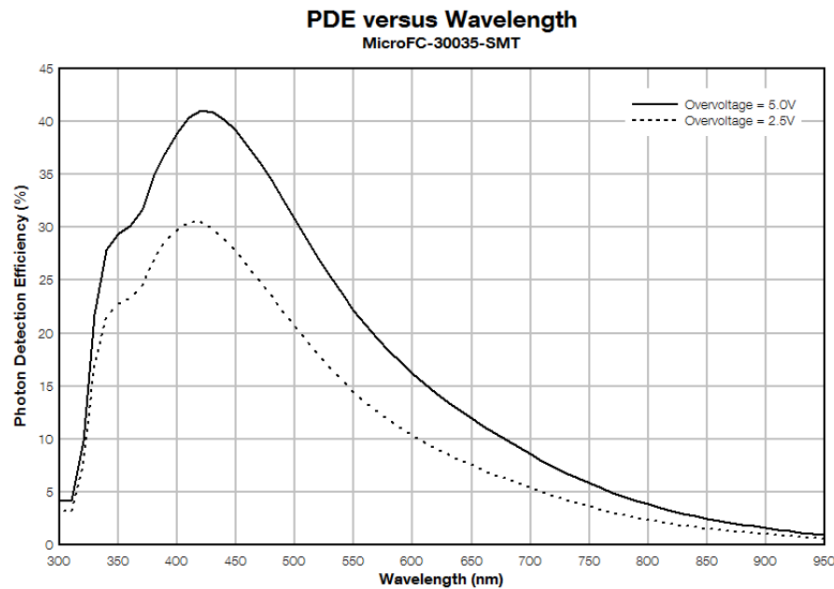


Figure 2.15: PDE vs. wavelength for two different overvoltages where the 5.0 V (solid black line) shows higher PDE compared to 2.5 V (dashed line). Reproduced from [57].

2.5 Scintillator Detectors for γ ray Detection and Digital Pulse Processing

γ -ray scintillator detectors consist of a dense scintillator that can stop the γ rays and the energy deposited by each interaction is converted into optical photons as mentioned in Section 2.2. The produced photons then travel through the scinti-

lator until they reach the photo-detector to be detected and are converted into electrical signals that are proportional to the energy that the γ -ray photon deposited in the detector. The signals that are produced are often weak and need to be amplified before further processing using a preamplifier. However, the signals that are produced can also be noisy, and a shaping amplifier is needed to filter the signals which later produce semi-Gaussian shaped pulses within a reduced bandwidth that can be processed and digitised. Figure 2.16 shows an example of signal processing chain that can be used for spectroscopy measurements.

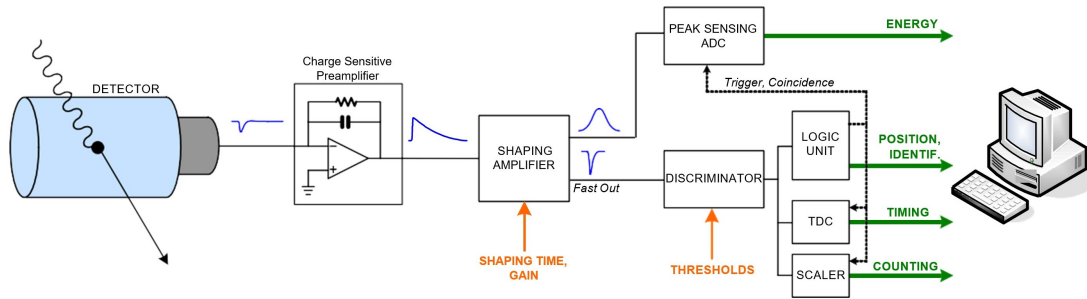


Figure 2.16: A diagram showing the digital acquisition system following an analog electronic chain. The raw signals produced from the detector are amplified using the preamplifier, and the shaping amplifier filters out the noise. The signals produced are semi-Gaussian shaped, and they can be measured by an Analog to Digital Converter (ADC). Reproduced from [59].

As mentioned before the number of the photons detected are proportional to the energy deposited by the incident photon, and it can be calculated using:

$$N_{ph} = E_{\gamma} \times LY \times PDE \quad (2.16)$$

where E_{γ} is the energy deposited in the scintillator, LY represents the light yield, i.e. the number of scintillation photons produced per MeV and PDE gives the percentage of photons that are detected by the photosensor.

Another important property of such a system is the percentage energy resolution that can be defined by the following ratio :

$$\left(\frac{\Delta E}{E}\right) = \frac{FWHM}{H_0} \times 100 \quad (2.17)$$

where FWHM represents the full width half maximum of the peak and H_0 is the centroid position of the full energy peak as shown in Figure 2.17.

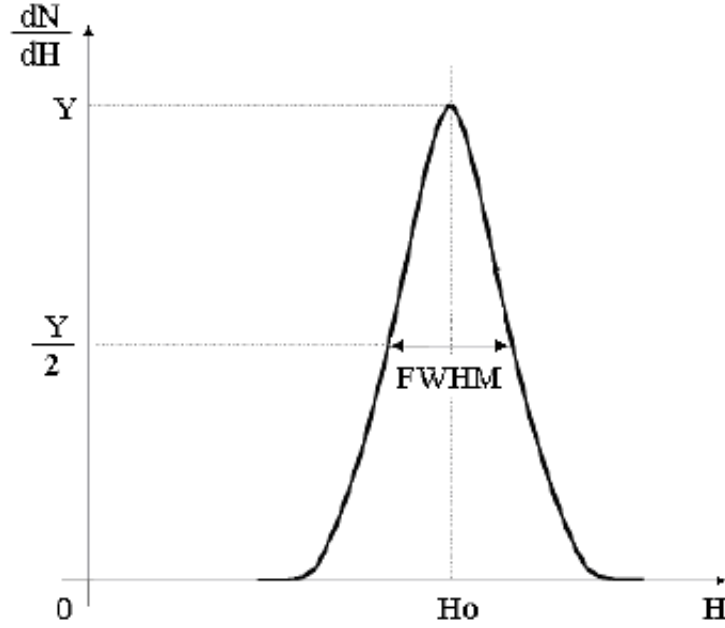


Figure 2.17: An illustration of a spectroscopic system energy resolution definition. The resolution is calculated using the ratio between the FWHM and the centroid position of the peak (H_0). Reproduced from [60]

However, there are different factors that must be taken into account when calculating energy resolution that can affect the performance of the system. The calculation can be expressed as follows: [61]:

$$\left(\frac{\Delta E}{E}\right)^2 = (\delta_{int})^2 + (\delta_p)^2 + (\delta_{st})^2 \quad (2.18)$$

where

- δ_{int} is the intrinsic resolution that expresses the contribution of the non-proportionality of the scintillator.

2.5. Scintillator Detectors for γ ray Detection and Digital Pulse Processing

- δ_p is the transfer resolution that represents how many photons successfully reach the photosensor.
- δ_{st} are the statistical fluctuations that are a result of the photosensor's characteristics such as the PDE and scintillation light fluctuations.

δ_{st} is directly affected by the number of photons detected N_{ph} and can be expressed as follows:

$$\delta_{st} = \sqrt{N_{ph}} \quad (2.19)$$

This indicates that increasing the number of photons improves the statistical fluctuation which contributes to improving the energy resolution of the detector. This can be improved, for instance, by wrapping the detector with a reflective material (excluding the areas where the scintillator and the photosensor are joined together). As a result, photons that escape the crystal can be reflected back and detected.

Chapter 3

Methodology

Chapter 3 presents the processes carried out for designing and fabricating a $6\times 6\times 76.2$ mm CsI:Tl long crystal coupled to two 6×6 mm² SiPMs at both ends (1D detector) and a $50.44\times 50.44\times 50.44$ mm³ cuboid CsI:Tl crystal coupled to six 8×8 SiPM arrays (3D detector). This chapter also details the experimental setup, including the scanning table, electronics and data acquisition system. The related energy, position resolution measurements and 3D position reconstruction methods have also been discussed. Finally, the Geant4 simulation model and modelling of the 1D and 3D detectors have been introduced in this chapter.

3.1 Experimental set up and Measurements

3.1.1 1D CsI:Tl Detector

3.1.1.1 Detector Configuration

A $6\times 6\times 76.2$ mm² CsI:Tl crystal manufactured by Hilger crystals was used. The properties of the crystal are presented in Table 3.1.

Table 3.1: Properties of a CsI:Tl scintillator

Density, g/cm ²	4.51
Light yield,ph/MeV	54000
Decay time, ns	1000
Refractive Index	1.79
Wavelength of peak emission, nm	540

Two 6×6 mm² C-type silicon photomultipliers manufactured by SensL were then optically coupled using a silicon optical grease (EJ550) at both extremities of the crystal. The crystal and the SiPMs surfaces were cleaned using isopropanol and lint-free tissues. This type of SiPM consists of 60035 micro-cells, and each micro-cell is 35 μ m in size [62].

The crystal was wrapped with three different wrapping materials for both energy and position resolution measurements. Figure 3.1 shows an example of the three different wrapping materials PTFE, a black tape and a highly reflective 3M Enhanced Specular Reflector (ESR) sheet that were used in this test. For the PTFE, eight layers were used on all sides of the detector's surfaces excluding the surfaces with the SiPMs. To secure the SiPMs position, the whole detector was covered with the tape, and the same procedure was done with the black tape.

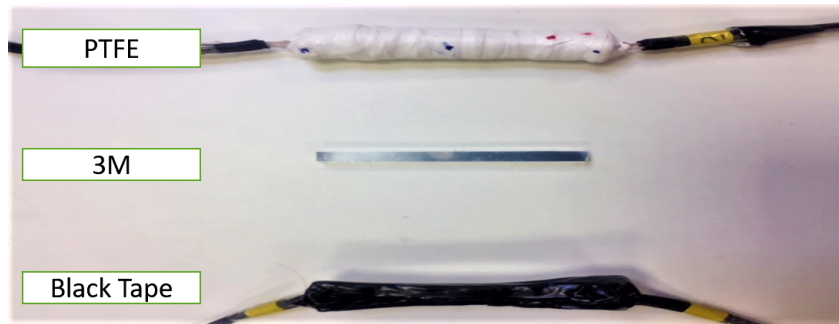


Figure 3.1: Examples of different wrapping materials used for the 1D scintillator detector (PTFE, 3M ESR sheet and Black tape).

The 3M ESR sheets were less flexible than the other materials, which made it hard to bend it around the detector which led to scratching symmetrical lines on the surface of the sheets using a CO₂ laser cutter. The 3M ESR sheets were placed under the focused laser beam, programmed to move in the y direction and burn four equal rectangular shapes. This process made the 3M ESR sheets more flexible to be bent and handled. The sheets were then placed on each of the faces of the crystal; the PTFE tape was used to secure the 3M ESR sheets. and both the SiPMs on the scintillator's surface. The detectors were wrapped with an aluminum foil to shield them from ambient light.

3.1.1.2 Measurements and Data Acquisition Systems

The energy calibration measurements were carried out using ¹³⁷Cs and ¹⁵³Eu sources. The signals from both SiPMs were summed together and connected to an Ortec amplifier model 571. The amplified signals were then connected to a Multi-channel Analyser (MCA) and energy spectra were recorded for each detector. The energy resolution ($\frac{\Delta E}{E}$) was obtained using Equation 2.17.

γ rays interaction positions were measured by taping the detector to a plastic holder to stabilise its movement during the experiment. It was then mounted on an xy linear drive placed inside a scanning table built at the nuclear physics laboratory at the University of York as shown in Figure 3.2.

3.1. Experimental set up and Measurements

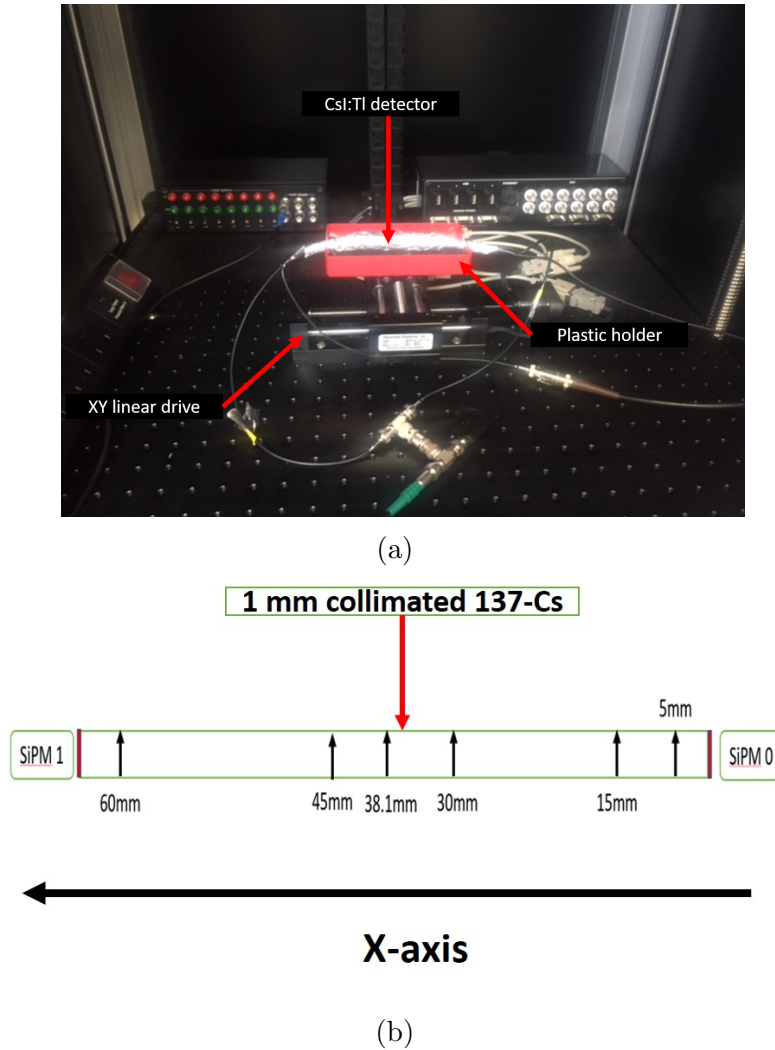


Figure 3.2: (a) Illustration of the experimental setup for the 1D detector which is placed on a plastic holder (red). The holder along with the detector was then placed and stabilised on an xy linear drive for the xy measurements scan and (b) a schematic drawing showing where the source is located.

A ^{137}Cs source with an activity of 370 MBq is positioned at the top of the cabinet above the detector and is housed in a tungsten collimator 1 mm hole and further surrounded by lead. At the end of the collimator, a safety shutter is placed that shields the source when the door of the cabinet is opened. The detector was placed 74 mm from the exit of the collimator and was moved in 5 mm steps along the x direction of the scintillator for fifteen positions, and each position was irradiated for five minutes.

3.1. Experimental set up and Measurements

To record the signals from each SiPM, they were split and connected to a sixteen channel CAEN Model V1730B digitizer where only two channels were used. The signals connected to the CAEN V1730B were digitized and controlled by a console application called WaveDump where trigger levels, offsets and the trace length of the recorded pulse can be pre-programmed. Figure 3.3 depicts a sketch of the experimental set up and the Data Acquisition system (DAQ), and Figure 3.4 shows an example of a recorded signal before data processing. The following parameters were preset:

- Trigger level 2070 mV.
- Offset set: 0.
- Recording length : 2100 samples = 31.5 μ s.
- Post Trigger : 80%.

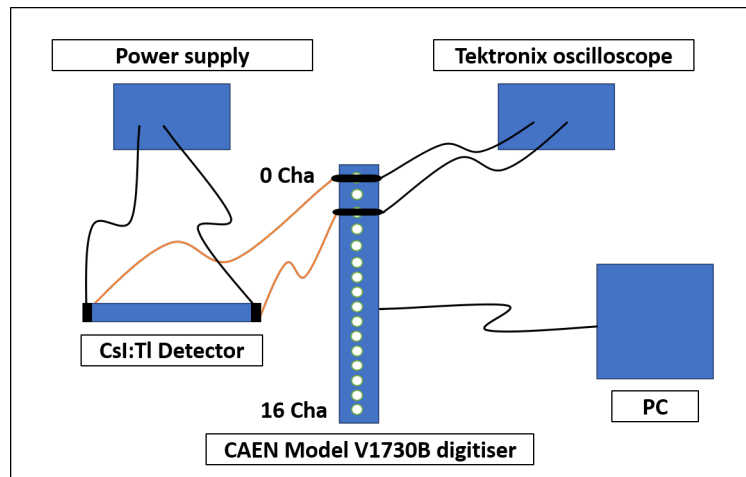


Figure 3.3: Schematic diagram showing both the SiPMs connected to a power supply and to a 16 channel CAEN V1730B digitiser. The signals were displayed on a Tektronix oscilloscope for monitoring.

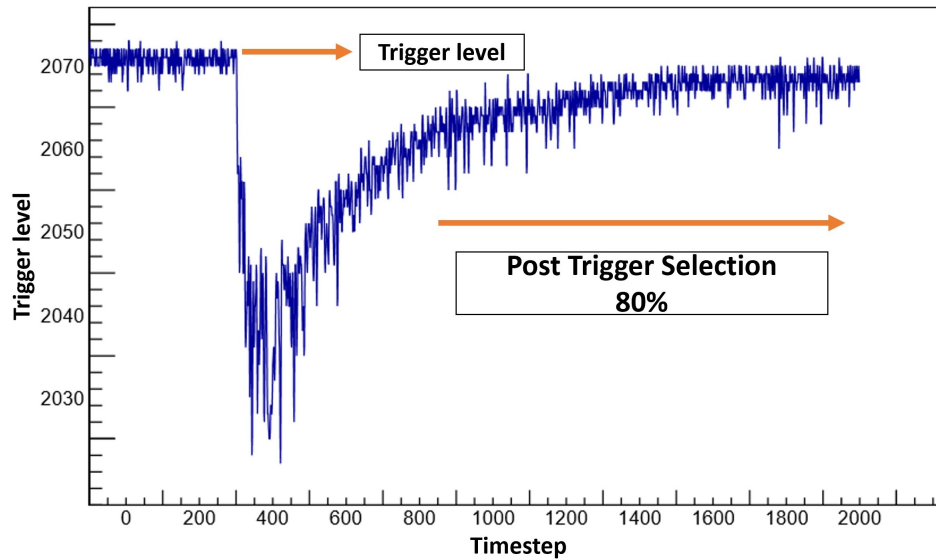


Figure 3.4: An example of a signal recorded using a CAEN Model V1730B digitiser. The image shows the signal recorded after applying the parameters to select the correct accusation window.

This type of signal acquisition has some advantages over analog processing. The advantages are that trigger level, post-trigger and sampling rate can be pre-programmed to select the accusation window. Further, the information stored can be processed without being affected by changes such as in the temperature and additional noise that can affect the data output.

For the beam position measurements, each detector was moved in 10 mm steps along the x and y direction to build a 2D profile of the detector (Appendix Figure A.1). The count rates for each position were recorded, for this provides a clear indication of when the detector is within the beam profile. The electronics noise level was measured without the source and found to be < 2 mV. The light ratio distribution measured at both SiPMs, at each position, was calculated using the following equation:

$$r = \frac{SiPM0}{(SiPM0 + SiPM1)} \quad (3.1)$$

where SiPM0 and SiPM1 are the amplitudes of the signals from each of the

3.1. Experimental set up and Measurements

SiPMs. The light ratio distribution was then fitted with a Gaussian function to obtain the centroid and FWHM for each position. Each light ratio distribution was then plotted against each interaction position and was fitted with a linear fit (see Section 4.1 for the illustration). This calibration procedure allowed for measuring the interaction position from the signals measured at the two SiPMs. To calculate the average position resolution, the average FWHM and the gradient obtained from the linear fit were used as follows:

$$X = \frac{FWHM}{g} \quad (3.2)$$

where X is the measured position resolution, g is the gradient value obtained from the linear fit and the FWHM is the full width half maximum of the ratio light distribution and can be calculated as follows:

$$FWHM = 2.355 \times \sigma \quad (3.3)$$

where σ is the standard deviation that measures the variation of the distribution. However, the position resolution that is measured does not take into account the beam divergence due to the thickness, diameter and length of the collimator to the detector. As a result, the size of the beam spot (BSP) hitting the detector is broadened and the BSP FWHM is found to be 2 mm and the actual position resolution (R) calculated using the following equation:

$$R = \sqrt{X^2 - BSP^2} \quad (3.4)$$

The BSP was calculated based on the geometry of the collimator and by knowing the length and diameter of the collimator (90 mm, 1 mm). The divergence of the beam was found to be 0.318°. This allowed an easy and suitable approach to calculate the BSP at different distances of the source. The results of the three

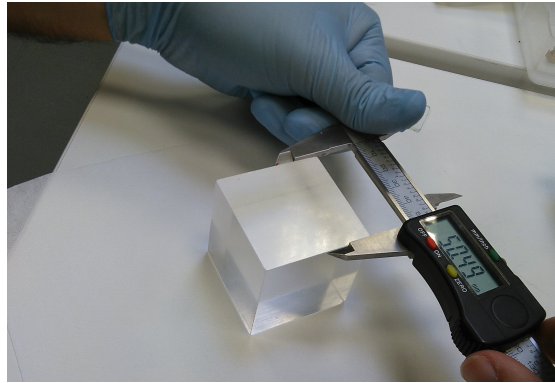
detector configurations were collected, and they have been compared in Section 4.1.

3.1.2 3D Cubic Detector

3.1.2.1 Detector Configuration

Two detectors were utilised for this setup. They have been defined as the main detector and the coincidence detector. The main detector was constructed from a $50.44 \times 50.44 \times 50.44 \text{ mm}^3$ cubic CsI:Tl crystal with the same properties as those presented in Table 3.1. The faces of the crystal were covered with six 8×8 SiPM arrays of SensL J-type and each SiPM array consisted of $6.13 \times 6.13 \text{ mm}^2$ pixels with a total area of $50.44 \times 50.44 \times 50.44 \text{ mm}^3$ as shown in Figure 3.5. This type of SiPM provides two Samtec 80-way connectors, type QTE040-03-F-D-A connectors [63] that can be connected to the preamplifiers boards (made at the University of York), which can be used to sum up the output of all 64 pixels and can also amplify the individual signals (Appendix Figure A.2).

3.1. Experimental set up and Measurements



(a)



(b)

Figure 3.5: (a) An image of the cubic CsI:Tl being measured.(b) An image of one of the 8×8 SiPM array that is coupled to one of the crystals faces for photons detection.

The surfaces of the SiPM arrays were cleaned with isopropanol, and each SiPM was placed into a socket of a 3D plastic structure as shown in Figure 3.6 to cover all of the faces of the cube. To light couple the arrays to the crystal's surface, a silicon optical grease (EJ550) was spread as evenly as possible on the surface of each array. The CsI:Tl was then placed into the first half of the 3D structure, and it was checked that the three faces of the crystals were totally covered by the arrays and then the second half was used to cover the remaining faces. A PTFE tape was then used to hold the structure and to ensure that the SiPM arrays are positioned correctly.

3.1. Experimental set up and Measurements

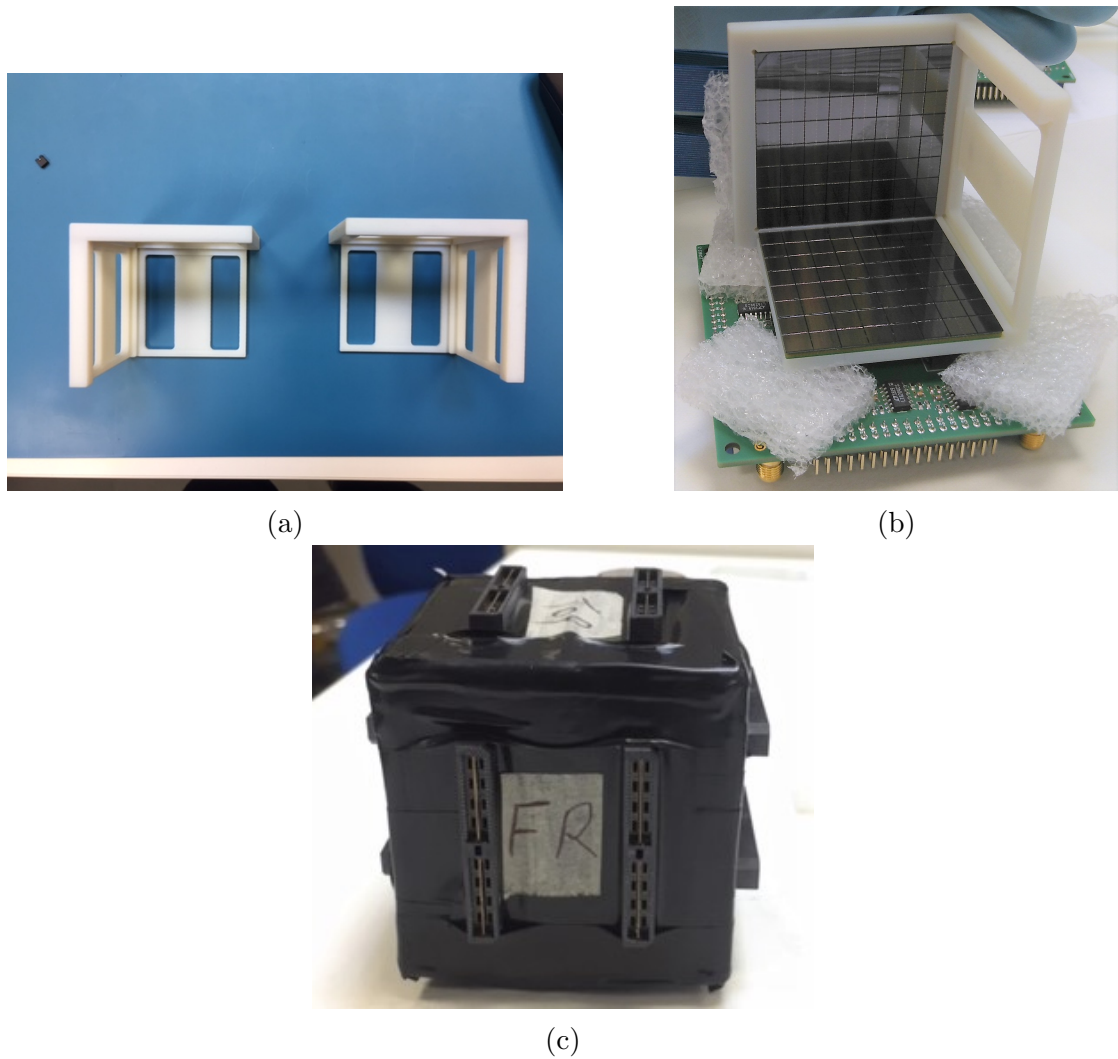
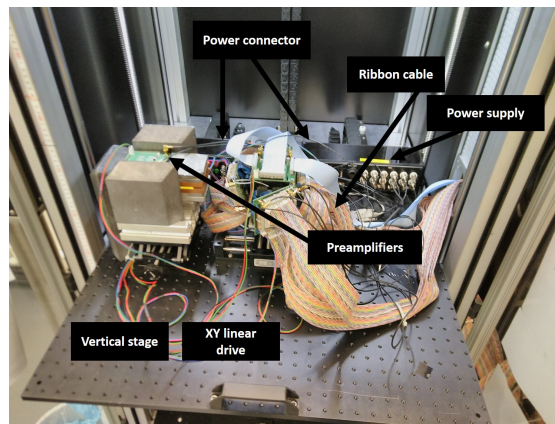


Figure 3.6: (a) The image shows two plastic 3D holders, each holding 3 8×8 SiPM arrays. (b) The image shows how the arrays are inserted inside the plastic holder. (c) The image shows the final detector configuration where all of the faces of the cubic scintillator are covered with the arrays and then wrapped with a black tape.

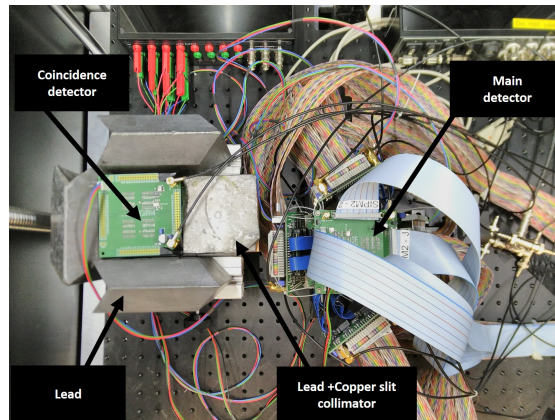
Figure 3.6 shows the 3D detector at various stages during the assembly. The arrays were then connected to preamplifiers boards that were made at the University of York and were mounted on the same xy linear drive placed inside the scanning table cabinet. The position of the 1 mm collimated source provided a pencil-like beam of γ rays that hit the main detector at well-defined x and y positions. Defining the third coordinate (z) required the use of a second independent detector (coincidence). This detector consisted of a $50.44 \times 50.44 \times 25.44 \text{ mm}^3$ CsI:Tl crystal and a single SiPM array of the same type as those used for the

3.1. Experimental set up and Measurements

main detector. The crystal and the array surfaces were cleaned using the same procedure as the one used for the main detector. The array was coupled at the top of the cuboid crystal using a silicon optical grease (EJ550) and then wrapped with a PTFE tape. The detector was then placed on a manually adjustable vertical stage behind a horizontal 4.5 mm slit collimator made of lead and copper, and the spot size obtained from such a slit was found to be 3.5 mm. Figure 3.7 shows the experimental setup and the positions of the main and coincidence detector inside the cabinet.



(a)



(b)

Figure 3.7: Experimental set up (a) Front image (b) top image where the main detector is placed at the left of the collimator and under the source. At the left of the slit collimator the coincidence detector is positioned to detect all Compton scattered rays events with a 90° scattering angle.

3.1.2.2 Data Acquisition Systems

The γ rays that interact with the scintillator may be absorbed (Photoelectric absorption) or scattered (Compton scattered) once or multiple times as shown in Figure 3.8. In the present experiment, the coincidence detector was used to select the events that go through the slit collimator after scattering at an angle of 90° from the main detector. A schematic sketch of the setup is shown in Figure 3.9, which shows an example of a coincidence event and the dimensions and distances of the different components. The angular coverage in the vertical direction without the energy cut was found to be $90^\circ \pm 3$, and the uncertainty depth was found to be ± 7 mm.

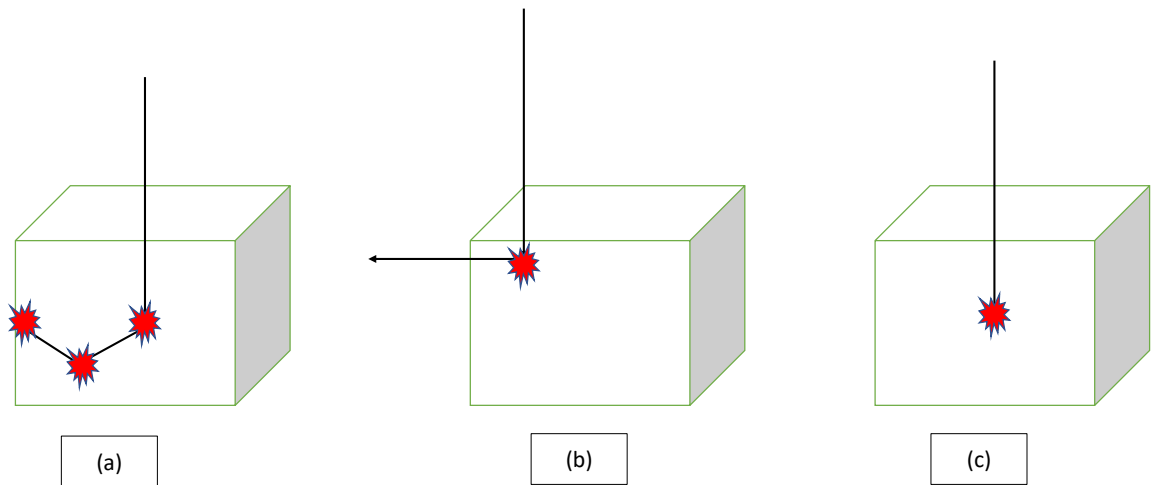


Figure 3.8: Illustration of the different γ -ray interaction mechanisms in a monolithic scintillator. (a) shows multiple Compton scattered events before exiting the detector. (b) shows one 90° Compton scattered event exiting the detector and (c) shows where the event deposits all of its energy (photoelectric absorption) and no Compton scattering events.

3.1. Experimental set up and Measurements

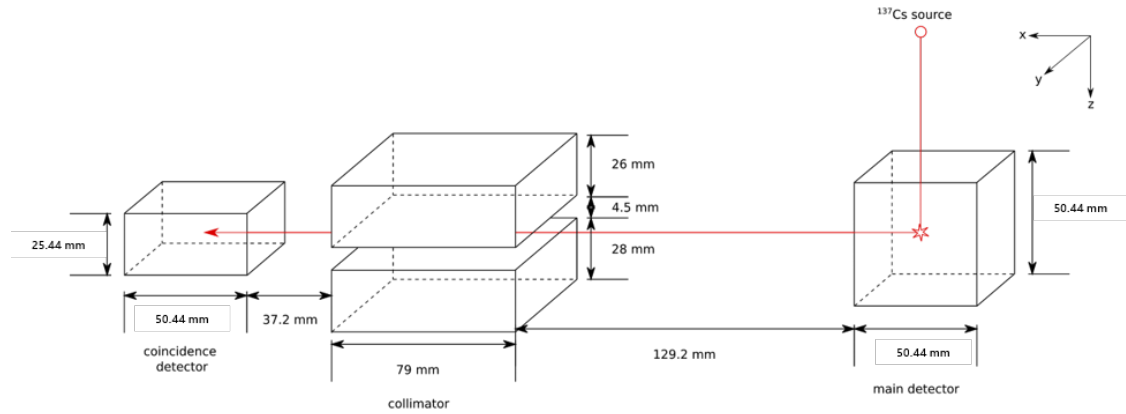


Figure 3.9: A schematic diagram of a left-handed coordinate system showing the collimated source hitting the middle of the main detector and scattering at 90° . The scattered γ ray then passes through the slit collimator and is detected in the coincidence detector. The diagram also shows the dimensions of each of the components of the experiment and the distances between them.

Optical photons that were generated inside the main detector were detected by the six SiPM arrays which convert them to electrical signals. These signals are then read out by the preamplifier boards attached at the back of each array. Each board outputs the 64 channels of the array into groups of 16, amplifies the individual pixel signals with x10 gain (but without shaping filter). A sum of all of the 64 channels of the array were connected to a separate output for triggering and energy calibration measurements. Both the individual and the sum signals were sent to the FEBEX3b boards that were placed inside a crate. FEBEX3b is a 16 channel, 50 MHz (ADC) with a resolution of 14-bit [64]. It was equipped with Field Programmable Gate Arrays (FPGAs) that determine the pulse height of the incoming signal using a moving-average filter with user-defined parameters. An example of the FEBEX3b card components is shown in Figure 3.10.

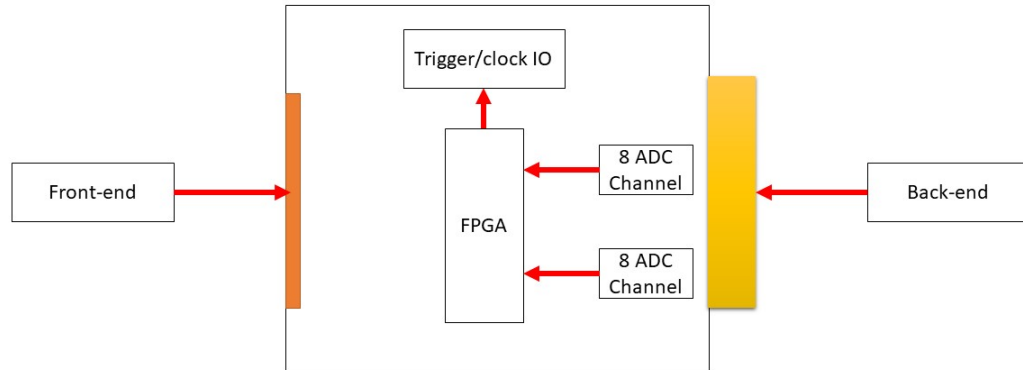


Figure 3.10: A schematic sketch of an individual FEBEX3B card component. The FPGA is the main component used for defining the detected signal's height.

The crate powered up the boards for signal processing and was connected to the Exploder which managed the triggers and communicated with the FEBEX crate via a ribbon cable [65] to the SFP module. The SFP module was connected to the crate via a peripheral component interconnect express (PCIe) connector which connected the crate to the external world.

The Multichannel Branch System (MBS) developed at the GSI center that contains a PEXOR (reads the signals sent from the FEBEX3b) and a TRIXOR (manages the triggers sent from the Exploder) was also used and operated using an external computer [66]. Figure 3.11 shows parts of the DAQ system used in this experiment. The triggering condition is generated in the Nuclear Instrument Module (NIM).

3.1. Experimental set up and Measurements

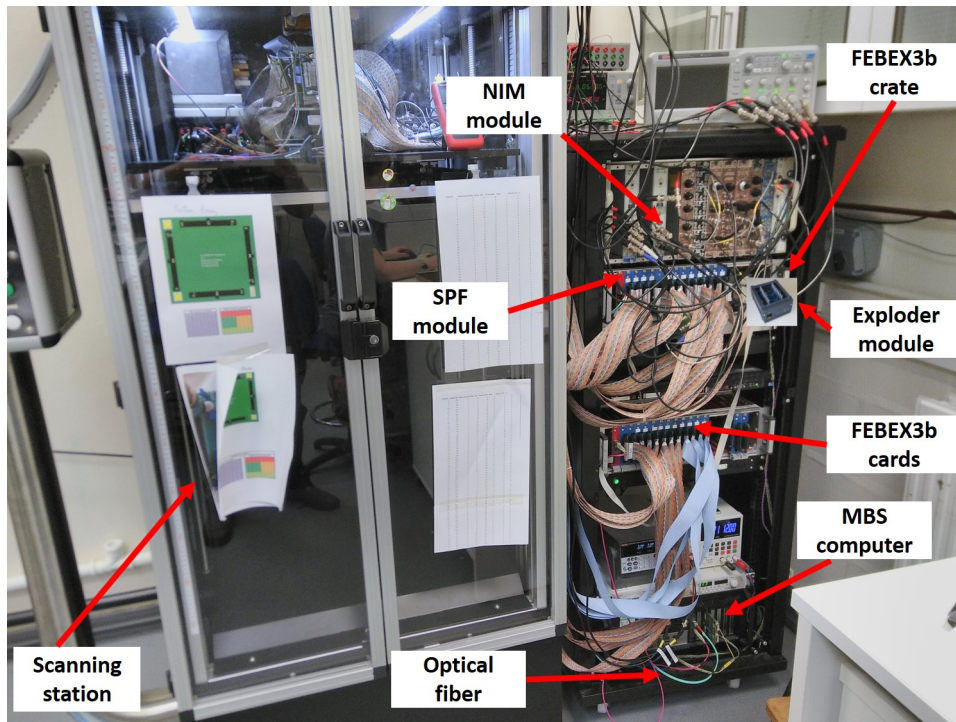


Figure 3.11: An image of the scanning table station and the DAQ system used for recording the events. The crates were used to power up 25 FEBEX3b cards and the SPF module. The NIM module provided the triggering condition and the SPF module.

The triggering signals were generated in the Exploder module and sent to the Febex cards. The Exploder module was connected to an SFP module via a ribbon cable at the crate side and the TRIXOR card at the PC end which managed the triggered signals sent by the Exploder. Data sent from the Febex cards were read out by the PEXOR card that was connected via an optical fiber cable to the SFP module.

In total, 25 Febex3b modules were used to readout the $6 \times 64 = 384$ pixel channels as well as the sum and coincidence signals. The DAQ system was triggered by summing all of the six signals from each SiPM array into one total signal from the detector. The signal was then sent to a Timing Filter Amplifier (TFA) and was then converted to a logical signal using a timing discriminator. A sketch of the trigger logic applied for this setup is shown in Figure 3.12

3.1. Experimental set up and Measurements

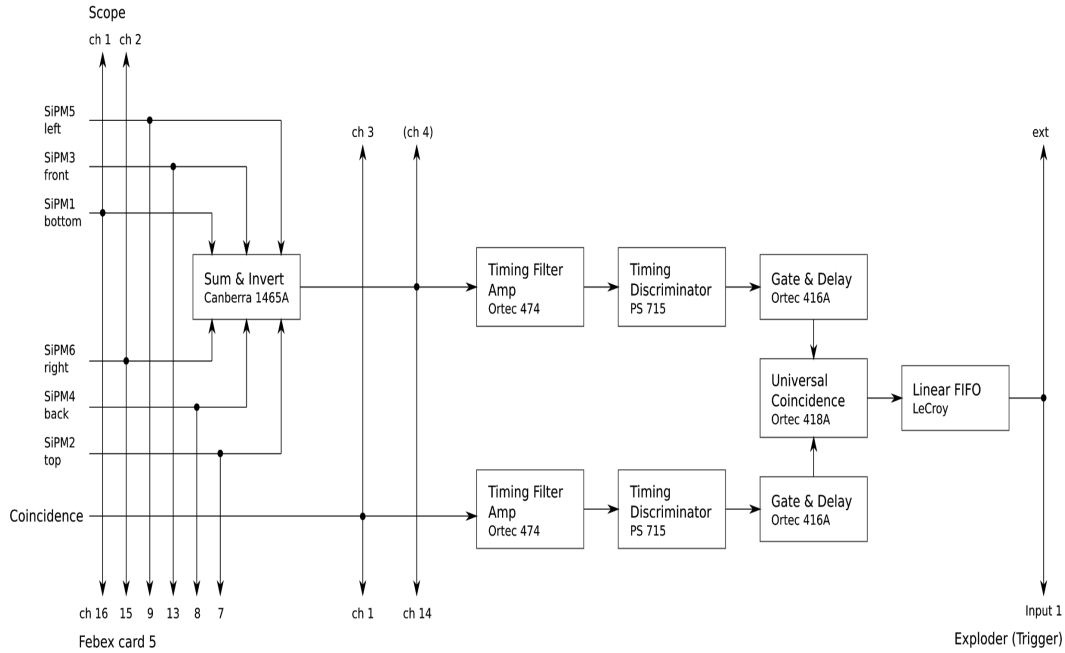


Figure 3.12: A sketch of the external trigger logic was applied to the 6-sided readout. The corresponding summed SiPMs outputs from each of the preamplifier cards are seen.

3.1.2.3 Measurements

The energy resolution for both the detectors was investigated using ^{137}Cs and ^{153}Eu sources. The measurements were carried out individually for each of the detectors and without the coincidence condition. The detectors energy resolutions were calculated using the Equation 2.17 and compared.

γ -rays interaction position measurements were carried out by moving the main detector to various x and y positions. The depth of the γ -rays interaction inside the main detector were defined by adjusting the height of the side slit collimator using the vertical stage. Hence, the position of the a 90° Compton scattered γ -rays interaction could be known in all of the three dimensions. By using Equation 2.2 it was found that for a coincident event the deposited energy in the main detector was 374 keV and that of the scattered γ rays was 288 keV, and a total of 27 positions were irradiated. The measurements acquisition time was between 1 to 3 days depending on how far the interaction position was from the coincidence

detector which affected the number of counts recorded. The measurement time was also effected by the stability of the DAQ system, which sometimes crashed, so no counts were recorded, and had it to be restarted.

3.1.2.4 3D Position Reconstruction Methods

The γ rays interaction positions were estimated by employing different reconstruction methods. First, 2D average and single event light maps were generated from experimental and simulation data and from a geometric simplistic model. The 2D light maps that were generated showed the number of photons that were being detected by each SiPM array at each face of the cube. The simplistic model (SM) is a function that was developed using the solid-angle (Ω) coverage of a rectangular pixel relative to the interaction point and the solid angle. Figure 3.5 illustrates the parameters that were used for calculating the Ω , and in such a case it can be calculated by using the following equation [67]:

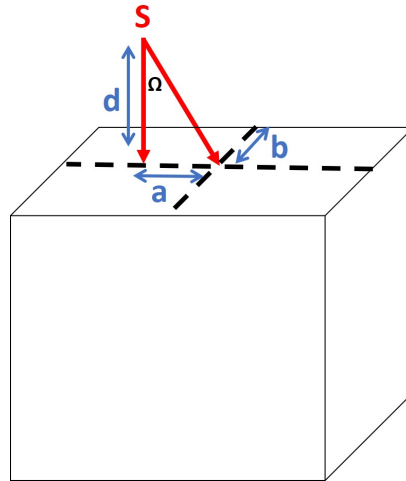


Figure 3.13: A sketch showing the parameters used for calculating the Solid angle Ω . The source position is given by the S, and d represents the source distance from the photo-detector. The a and b symbols represent the horizontal and vertical coordinates of the photo-detector.

$$\Omega = \arctan \frac{ab}{d\sqrt{a^2 + b^2 + d^2}} \quad (3.5)$$

where a and b are the length and width of the photodetector and d is the distance between the source location and the photodetector. The proposed SM model estimated the number of photons that were detected by each SiPM of the six arrays at different interaction positions including the solid angle effect. This effect describes the relationship between the origins of the interaction position and the photons measured by the pixels and can be calculated by:

$$SM = \frac{36}{(4 \times \pi \times r_1^2 \times r_2^2) \times N_p \times PDE} \quad (3.6)$$

where r_1 is the distance between the interaction point and any pixel of the array. The r_2 is the term that adjusts for the incident angles of the photons hitting the SiPMs located further away from the source location and N_p is the number of photons produced for each γ -ray interaction and the PDE of the arrays.

Position reconstruction is performed by two different approaches:

- Light ratio method.
- The χ^2 minimisation method.

For the light ratio method, the light ratio of opposite arrays obtained from the average signals for both experimental and simulation data using Equation 3.1 were used, and the results were compared as shown in Section 4.2. The same method was applied for the pixels with the highest number of photons detected at opposite SiPM arrays (experimental data). The 3D reconstruction was carried out by processing 100 events for different interaction positions, and x, y and z coordinates were obtained through the light ratio of the maximum pixel located at opposite SiPMs.

The Chi-square minimisation (χ^2) test was applied, which is, in general, an estimation of how much the data and a model match. The following equation was applied:

$$\chi^2 = \sum \frac{(O - E)^2}{(\sigma)^2} \quad (3.7)$$

where O is the observed data (the normalised signal amplitude in each pixel), E is the expected data, which can be obtained from the signal amplitude estimated from the simulation data or the normalised signal amplitude from the geometric simplistic model, and $(\sigma)^2$ is the weighted uncertainties in the individual points (variance). In this case, it corresponds to $\sqrt{N_p}$. The χ^2 method was used to extract the x , y and z coordinates for 100 events that reproduce the experimental light distribution well where the interaction position for which the estimator is minimal was taken as the determined position.

The position resolution was estimated measuring the Root Mean Square (RMS) the light distribution obtained from both 3D reconstruction methods. Both methods were used to obtain the interaction positions at various interaction sites using the coincident data (restricted in x , y and z) and pencil beam (restricted in x and y) measurements. The two methods were compared by looking at the shape of the light distributions for each of the reconstructed interaction coordinates at different interaction positions and their position resolution values in terms of RMS.

3.2 Geant4

3.2.1 Introduction to Geant4 and its Applications

Geant4 is a Monte Carlo object-oriented computational tool based on C++ language that can simulate particles propagating through a material and it covers a wide range of energies, materials and different types of particles. Moreover, it performs some key functions such as defining complicated geometries, tracking and visualising that can be used in designing or optimising radiation detectors [68]. The 1D and 3D detectors were simulated using the GEANT4 toolkit (version 4.10.1), incorporating optical photon transportation. The physics models and optical properties were tested and validated by comparing them with the data reported in [69]. The same models were then modified to simulate the detectors presented in this thesis to compare the output with the experimental data. In this project, the aim of using such a simulation code was to construct a working model that can be used for predicting the interaction positions inside the crystal for different type of scintillators.

3.2.2 General Overview of Geant4

Certain key parameters that are included in the Geant4 framework as packages include:

- Material package is used to define the materials properties such as type of scintillator, density and its light yield. Some of this information can be found stored within its library, and if not possible, the user can specify their own list of component properties.
- Geometry package is used to construct geometrical structures for both simple and complex volume shapes. This is carried out by defining the components

and the positioning of logical volumes in respect to the mother volume. The defined volumes can also be duplicated or subtracted depending on the structure's design.

- The physics process is where the interaction of particles with matter can be defined, where Geant4 covers a wide range of processes including electromagnetic interactions and hadronic physics for high- energy research.

Other packages include a primary generator that allows the user to select the type, energy and position of the source or sources of interest. The particle's propagation through matter can be tracked, and its behaviour can be predicted depending on the user's specifications [70].

3.2.3 Modeling Scintillator Detectors Using Geant4

As described in 3.2.2, Geant4 has many packages that can be used for modelling detectors and comparing their outputs with experimental data. To achieve this goal, the many parameters included in these packages have to be configured before running the simulation.

The first step was to define the mother volume dimensions where they represent the outside environment that the detector is placed in. All physical processes and the detectors components were placed within the mother logic. In other words, any process that occurred outside the mother logic was ignored.

Secondly, the detector's shape and size must be defined with respect to the mother logic. The properties of the detector material such as the scintillator's density, doping type and the number of elements can be selected from the materials category in the GEANT4 library or determined by defining new elements depending on the user's choice.

The modelling of a scintillator detector must include the optical-photons process that was generated from the γ -ray interactions with the scintillator. When these optical photons meet an interface, they go through different interactions as described in 2.3. Information such as the scintillators refractive index, absorption length and the scintillation process for both fast and slow decay components were some of the key properties to implement in the code.

Several types of the particles were also carefully added to the physics list, for instance, γ rays, electrons and positrons. Moreover, different scattering process could be enabled such as Compton scattering. On the other hand, the physical volume dealt with the positioning and ensuring that all of the components were within the mother volume.

The third step dealt with the type, energy and position of the radiation source, and it could also be placed inside the detector depending on the user's requirements. There are two types of particle sources, the G4ParticleGun and the Genral Particle Source for modelling both simple and more complex sources.

Finally, the surface properties that the different components of the scintillator detectors were constructed of had to be carefully implemented in the simulation code. This could be achieved by selecting the model method (UNIFIED, GLISUR), type of the boundary which can be between two dielectric materials or dielectric-metal and the surface finishing which controlled the smoothness of the surface [71]. To detect the optical photons, the boundary between the photo-sensor and the scintillator material type was defined as a dielectric-metal which can absorb or reflect photons. The user also had an option to select between two dielectric surfaces that allow the optical photons to be absorbed, reflected and refracted as when defining between a scintillator and a wrapping material (PTFE, paint and black tape).

As mentioned above, UNIFIED and GLISUR are the two models that control how the optical photons interact with different types of the surface finishing. The

GLISUR model provides only polish and ground finishes and allows the user to control the roughness of the surface between 0 and 1 where 1 represents a fully polished surface, and optical photons reflect from the boundary according to Snell's law. If the user selects polish number < 1 , this increases the roughness of the surface, and the optical photons get reflected according to the Lambertian Distribution. The UNIFIED model describes the physical processes that optical photons undergo between two dielectric materials. Moreover, it provides more surface finishes such as GroundBackPainted, PolishedBackPainted, GroundFrontPainted, PolishedFrontPainted, ground and polish, which allow to simulate different reflection processes (Lambertian, Specular Spicke, Specular Lobe and Backscatter). To control the roughness of the crystal surface in the UNIFIED model, a parameter known as SigmaAlpha (σ_α) must be set and chosen, and zero corresponds to a fully polished smooth surface. This parameter introduces random microfacets with a Gaussian distribution which σ is defined as the width of that distribution [72].

3.3 Modelling 1 and 3D Detectors using Geant4

3.3.1 1D CsI:Tl Detector

As described in 3.2.3 there are several parameters that must be predefined that are based on the experimental setup, materials and components. Figure 3.14b shows the detector's design and a schematic sketch of the detector's components.

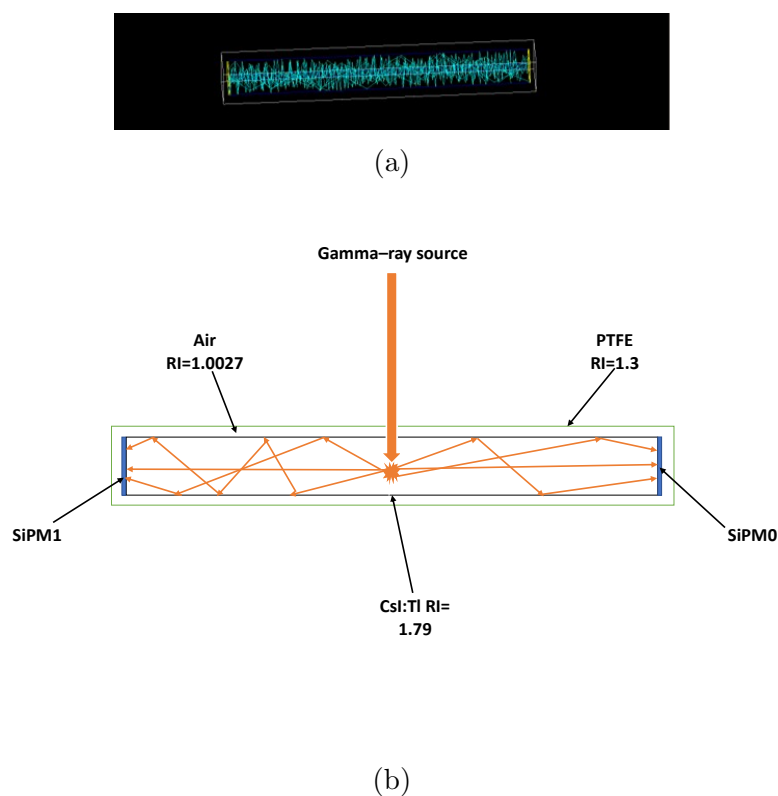


Figure 3.14: (a) shows the photon light (blue) propagating through the 1D scintillator detector model, and the yellow and white represent the SiPMs and the PTFE wrap respectively. (b) Shows the refractive index values of the materials used that are configured in the simulation code.

The CsI:Tl was designed as a $6 \times 6 \times 76.2$ mm³ bar and placed inside an air filled box that represented the outer atmosphere, and two 6×6 mm² epoxies were defined and placed at each of the long ends of the crystal. The whole detector was then placed inside another box that mimicked the PTFE wrapping material used in the experiment such that a small gap remained between the crystal and PTFE, which can be defined as air. Some of the parameters used are summarised in Table 3.2.

Table 3.2: Properties of the the CsI:Tl detector components as defined in the simulation.

CsI:Tl Density, g/cm ³	4.51
Light yield, ph/Mev	54000
CsI:Tl Refractive Index	1.79
Air Refractive Index	1.0027
PTFE Refractive Index	1.3
Epoxy Refractive Index	1.59

Optical photons behaviour at the interfaces between the components of the detector were also taken into account in the simulation. This included defining the model, type and finish of the surface. For example, the interface between the CsI:Tl and PTFE tape was defined as UNIFIED because the boundary was located between two dielectric surfaces. GroundBackPainted was selected for the surface finishing which defined it as a diffusive coating [72]. The (σ_α) is a parameter that controls the roughness of the surface provided by the UNIFIED model as discussed in 3.2.3. Table 3.3 shows each model, type, finish and (σ_α) value used in modelling this detector. A 662 keV γ ray emitted from a ¹³⁷Cs source was modeled using the G4ParticleGun and the number of particles fired was set to be 10000. The shape of the gun was chosen to be circle to mimic the 1 mm collimated beam. The source was moved in 5 mm steps along the x-axis (Figure 3.2 shows the coordinates of the system), and a total of fifteen positions were irradiated. Information such as the number of optical photons that reach the photodetectors, the energy of the γ

ray deposited in CsI:Tl crystal and the mechanism of the interaction (PE and CS) were stored in two hit classes for analysis.

Table 3.3: Type and surface finish of each interfaces between two different components defined in the simulations.

Boundry	Model	Type	Finish	σ_α
Crystal/PTFE	UNIFIED	dielectric-dielectric	GroundBackPainted	0.02
Crystal/Epoxy	GLISUR	dielectric-metal	Ground	-
Epoxy/PTFE	UNIFIED	dielectric-dielectric	GroundBackPainted	0.02

3.3.2 3D CsI:Tl Detector

In this model, the same physics list and optical photons properties model developed in 3.3.1 was used. This intensive simulation was undertaken on the Viking Cluster [73], which is a high performance computer facility provided by the University of York. The simulated model geometry is shown in Figure 3.15 which was set to mimic the experimental set up described in 3.1.2.1. As for the 1D detector, a ^{137}Cs source was modelled using the G4ParticleGun as the γ -ray source with an energy of 662 keV, and the number of γ rays fired was set to be 10^{10} .

To obtain the 3D coordinates of each single γ -ray interaction, the main detector was programmed to move in the x and y direction relative to the γ -ray source, which was at 0, 0. The coincidence detector along with the collimator were moved in the z direction to obtain the depth of the interaction point inside the main detector as in the case of the experiment. The only events recorded were the coincidence events generated from the γ rays that scattered into the coincidence detector and deposited the expected energy of about 288 keV. In addition, optical photons generated from such events were recorded, and as a result, the computational time and the disk space improved drastically.

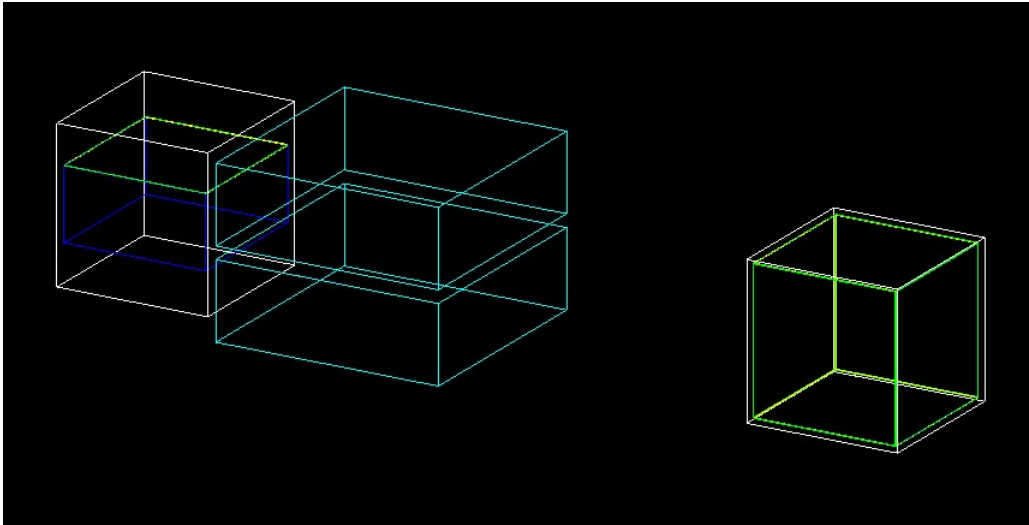


Figure 3.15: Simulated setup with dimensions comparable to the experimental setup. From left to right: coincidence detector with a single SiPM array (green-yellow) on the top surface of the crystal (blue), lead slit collimator (turquoise) and main detector with an SiPM array on each side. The γ rays from the ^{137}Cs source are illuminating the main detector from the top.

The simulation was performed for eighty-one positions spread over the entire detector volume. Two Hit classes were used, the `crystalHit` and the `SiPMHit`; the former recorded the energy that the coincidence events deposited in the main crystal, and the latter recorded the light photons detected by each SiPM. The `SiPMHit` class also recorded the type of interaction, number of interactions, coordinates of the interactions (x,y and z) and the number of the SiPM that detected the photons, which was defined as the SiPM id.

Chapter 4

Results

Chapter 4 presents the results obtained from both the 1D and 3D detectors. Section 4.1 presents the 1D detector experimental and simulation results for the experimental set up shown in Figure 3.2. In particular, it presents the energy resolution and the position resolution obtained using the light ratio method from both experimental and simulation model data. Section 4.2 presents the energy and position resolution results obtained for the 3D detector obtained from the experimental setup shown in Figure 3.7. The position reconstruction was achieved through the straightforward light-ratio method discussed in Section 3.1 and through the more sophisticated χ^2 minimisation method discussed in Section 3.1, which compared, on an event-by-event basis, the experimental 2D light maps of each SiPM array with those obtained by the models (Geant4 simulations and simplistic geometrical model).

4.1 1D Detector Results

4.1.1 Experimental Results

4.1.1.1 Energy Measurements

Three energy calibration measurements were carried out for the same detector using three different wrapping materials PTFE, Black tape and a highly retro-reflective 3M ESR sheet. The measurements were carried out using ^{137}Cs and ^{152}Eu sources. Figure 4.1 shows some of the different photo-peaks expected from both sources for all three detectors.

The average energy resolution values were calculated using Equation 2.17 for the three configurations and are summarised in Table 4.1. The average energy resolution for the 662 keV peak was obtained by calculating the energy resolution at each interaction position and dividing it by the number of positions (15 interaction positions). As expected from the three different wrapping materials, the black tape exhibited the worst energy resolution, which can simply be explained by looking at Equation 2.18. The equation shows that $(\delta_{int})^2$, $(\delta_p)^2$ and $(\delta_{st})^2$ affect the detectors energy resolution. However, for the three measurements the same crystal and SiPMs were used and, therefore, the effect of the terms one and two remain the same. This leaves $(\delta_{st})^2$, which depends on the number of photons that the SiPMs detect. In the case of black tape wrapping, the number of photons that were detected are lower than the photons detected by the PTFE and the 3M ESR configurations, as the black tape does not reflect back the photons that escape from sides of the detector.

4.1. 1D Detector Results

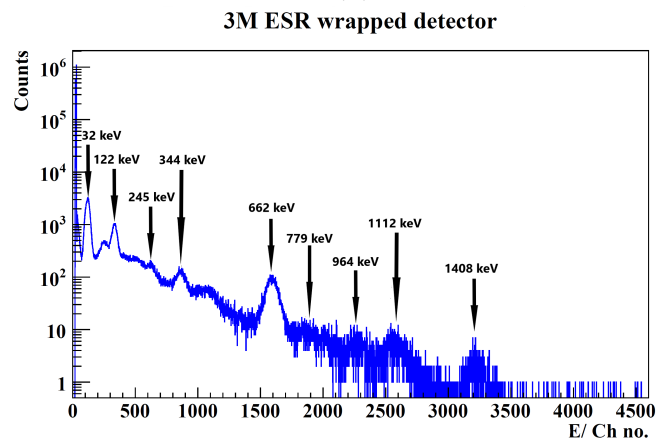
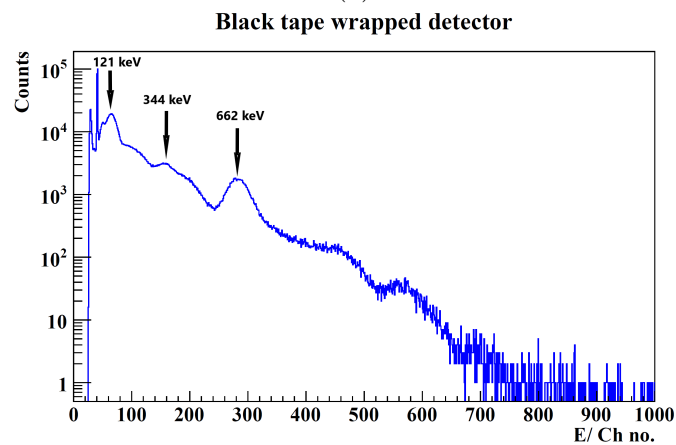
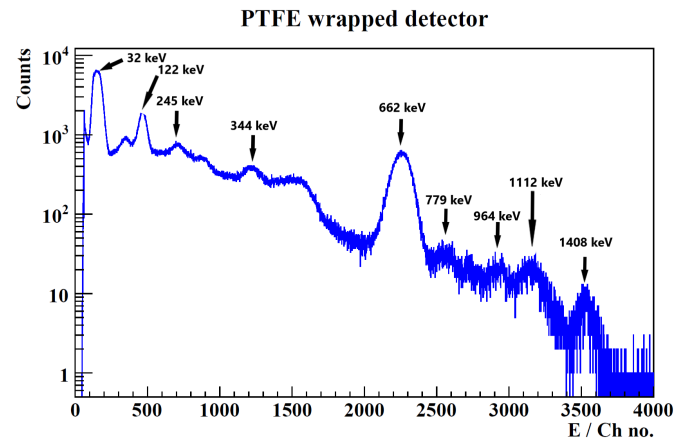


Figure 4.1: Energy spectrum obtained from ^{137}Cs and ^{152}Eu sources by a $6\times 6\times 76.2\text{ mm}^3$ 1D detector (see Figure 3.2 for detectors configuration). (a) Shows the PTFE-wrapped detector, (b) black-tape-wrapped detector and (c) the 3M-ESR-wrapped detector.

4.1. 1D Detector Results

Table 4.1: Type of the wrapping material and the average energy resolution calculated for each material.

Wrapping material	Average energy resolution
PTFE	$7.3 \pm 0.1\%$
Black Tape	$14.3 \pm 0.2\%$
3M ESR sheets	$6.8 \pm 0.2\%$

4.1.1.2 Position Sensitivity Measurement Methods

The position resolution measurements were carried out for the 1D detector configuration as described in Section 3.1.1.2 (Figure 3.2). Figure 4.2 shows a comparison of the total light detected by summing the two SiPMs and the spectrum measured at one end of the crystal bar for 15 γ ray interaction positions. For the summed (SiPM0+SiPM1) spectrum a shift in the light detected near the SiPM (black and red labelled peaks) is shown. This shift can be attributed to the increase in the number of photons being reflected at the crystal edges.

It also shows that the change in light collection for different interaction positions was more evident when measuring the light that reaches one SiPM (see Appendix Figure A.4 and A.5 for the black and 3M ESR wrapped detectors).

4.1. 1D Detector Results

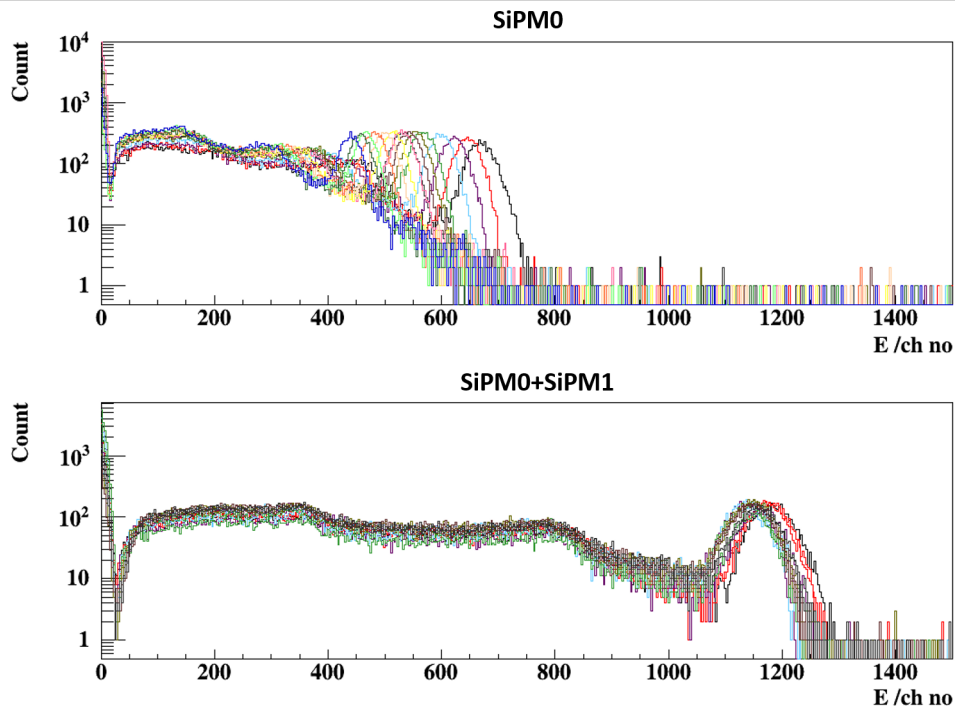


Figure 4.2: An example of the spectra measured at one end of the PTFE wrapped crystal (SiPM0, top) and the light measured by summing both SiPMs (SiPM0+SiPM 1, bottom) at different illumination interaction points along the long-axis of the 1D detector. The different colours represent the different interaction points.

Figure 4.3 illustrates the light ratio collected at one end of the crystal (SiPM0) for the three different wrapping materials as a function of the interaction position. It shows that the amount of light collected by SiPM0 varied more strongly with illumination positions compared to the other two wrapped detectors. Hence the same crystal and SiPMs were used for all of the three tests, and the main effect observed on the fraction of the light detected that came from the type of the wrapping material.

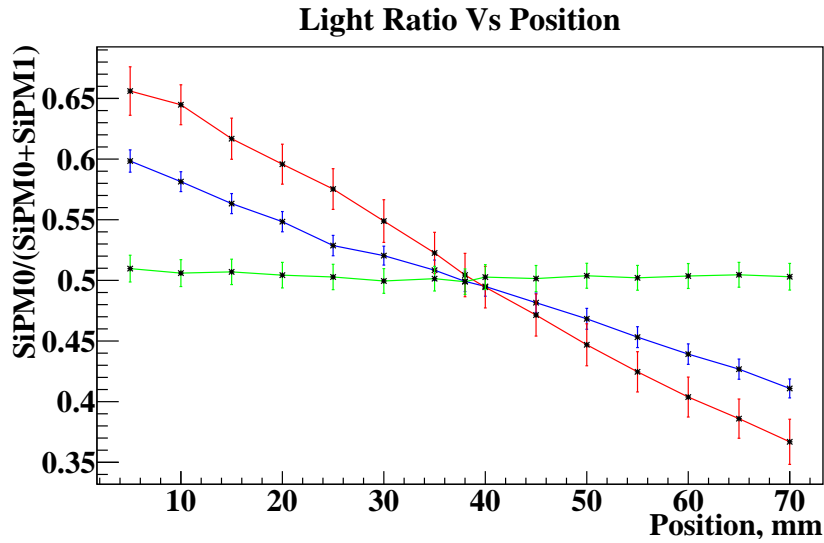


Figure 4.3: The light ratio of the two opposite SiPMs as a function of the γ -ray interaction position for black tape (red), PTFE (blue) and 3M ESR sheet (green).

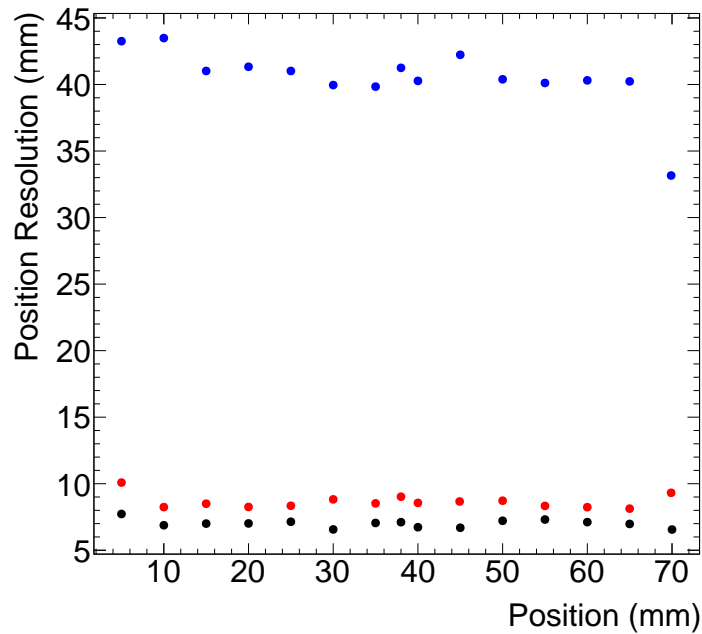


Figure 4.4: The Position resolution calculated at different interaction position for (blue) the 3M ESR, (orange) black tape and (black) is the PTFE wrapped detector.

Table 4.2 shows the average position resolution, average FWHM and average g values obtained for all three detectors. Although the g value of the black tape configuration was found to be 1.5 times larger than the PTFE detector, the FWHM was found to be 4 times larger than the latter, which slightly worsened

4.1. 1D Detector Results

the position resolution. This means that the black tape has a strong dependency on the interaction position which provides a higher g value, but due to the low number of light collected, a slightly worse position resolution is measured.

Table 4.2: Different types of wrapping and the corresponding position resolution obtained the light-ratio distribution and the gradient from the linear fit.

Wrapping material	Average position resolution	Average FWHM	Average g
PTFE	7.0 mm \pm 2.9 mm	0.01	0.003 mm
Black Tape	8.7 mm \pm 3.6 mm	0.04	0.05 mm
3M ESR sheets	40.5 mm \pm 18 mm	0.02	0.0 mm

Figure 4.4 shows the position resolution calculated at different irradiation positions along the crystal long-axis using Equation 3.2 for all three detectors. The 3M-ESR-wrapped version was expected to provide a similar outcome as the PTFE detector with a small g value and a good position resolution. However, it showed the worst position resolution out of the remaining two detectors. By looking at Figure 4.3, it can be seen that the light ratio collected by SiPM0 for the 3M-ESR-wrapped detector remained almost constant at all of the fifteen illumination points. Several attempts were carried out to correct this, including cutting the sheets separately to cover each face of the crystal, force bending the sheets around the crystal and, finally, using a laser cutter to etch the surface of the sheets to allow them to bend easier. All of the above techniques gave the same insensitivity and poor position resolution. It remains unclear whether this is due to bad light coupling of the SiPM or whether the specular reflection of the 3M ESR film is behind this observation.

4.1.2 Simulation Results

The PTFE-wrapped detector was modelled as described in Section 3.3, and Equation 3.1 was used to calculate the ratio of the signal detected in the SiPMs. Figure 4.5 shows the light ratio distribution detected for SiPM as a function of the position. As expected at position 38.1 mm, which corresponds to the middle of the crystal, both SiPMs detected 50% of the light emitted from the γ ray interactions. The light ratio distribution of an SiPM also showed a decrease as the interaction of the γ rays position moved further away from this SiPM.

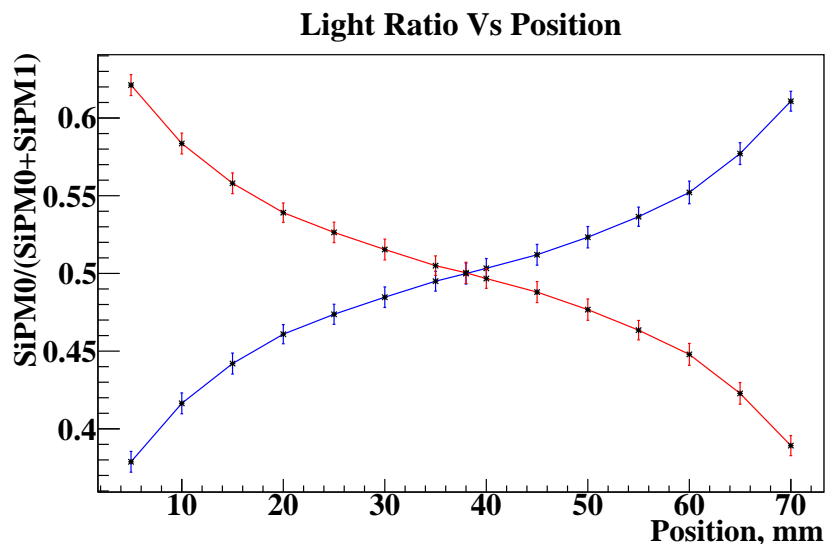


Figure 4.5: The light ratio is plotted as a function of the γ -ray interaction position for the simulated 1D PTFE-wrapped detector. The light ratio is shown for both SiPM0 (red) and SiPM1 (blue).

Figure 4.6 shows a comparison between the light ratio measured at SiPM0 for both experimental and simulation data. The figure illustrates that the ratio of the total signal measured experimentally and calculated using the Geant4 model at one end of the crystal (SiPM0) shows a strong position dependency. This dependence shows that the distance between the interaction positions and SiPMs has a strong influence on the light-sharing mechanism. The light ratio distribution for both the methods showed good agreement, excluding interaction positions near the edges. The difference of the light ratio distribution at the edges may be caused by the

difference in the number of the reflected photons, calculated by the simulation and measured experimentally.

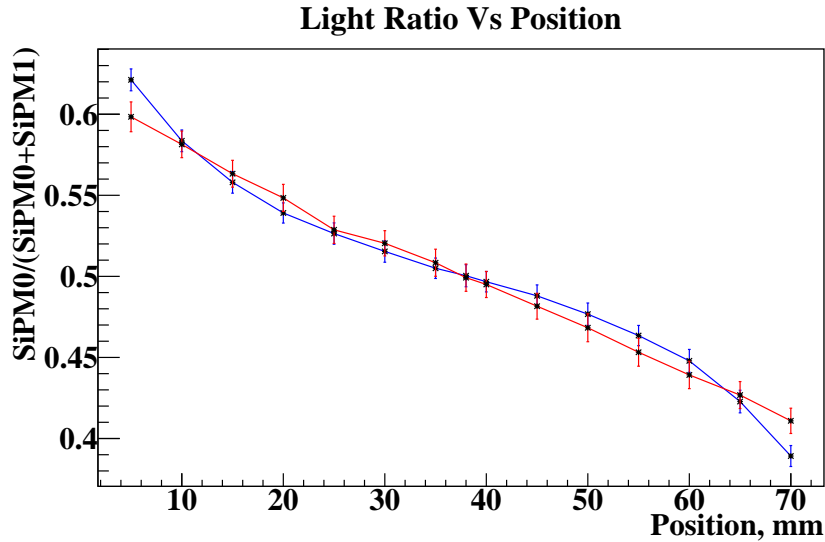


Figure 4.6: A comparison between the experimental (blue) and the simulated (red) data for the 1D PTFE-wrapped detector (Figure 3.2 shows the detectors configuration). The image illustrates the light ratio detected at SiPM0 as a function of γ ray interaction position.

Equation 3.2 was used to predict the position resolution value that can be obtained from such a configuration. The FWHM of the light ratio distribution at each position was measured using a Gaussian fit, and g was found from the linear fit of the light ratio. The simulation model predicts a position resolution of $5.3 \text{ mm} \pm 2.3 \text{ mm}$, which is close but somewhat better than the position resolution measured experimentally and given in Table 4.2.

The surface finishing type is one of the parameters that affect the interaction position estimation as has been reported [74]. In their study they compared the light ratio distribution for two surface finishing types (ground, polish) for a 15 mm thick CsI:Tl crystal at different interaction depths, and they reported that ground finish improved the estimation of the γ rays interaction depth position. To understand the effect of the surface treatment on the gradient of the linear fit, an investigation using the GLISUR mode in Geant4 that defines the surface treatment as polished or ground was performed. Different slope values (g) were

4.1. 1D Detector Results

calculated for a 97% reflective PTFE-wrapping using a number of different surface polishes (10-100%). The polish percentage parameter defines the roughness of crystal surface, and by increasing the percentage, the roughness of the crystal surface decreases till the surface becomes 100% fully polished. Figure 4.7 shows that the g value degrades exponentially by increasing the percentage of the surface polish. This exponential decrease is influenced by changing the surface from a diffusive (ground surface) to a more specular surface (polished surface) which changes the angle of the reflected light from reflecting in multiple directions to a singular predictable angle as shown in Figure 2.7 in Section 2.3. This also gives a preliminary prediction of what range of g values one expects when calculating the position resolution using Equation 3.2. An important note is that the gradient varies depending on the reflectivity of the wrapping material.

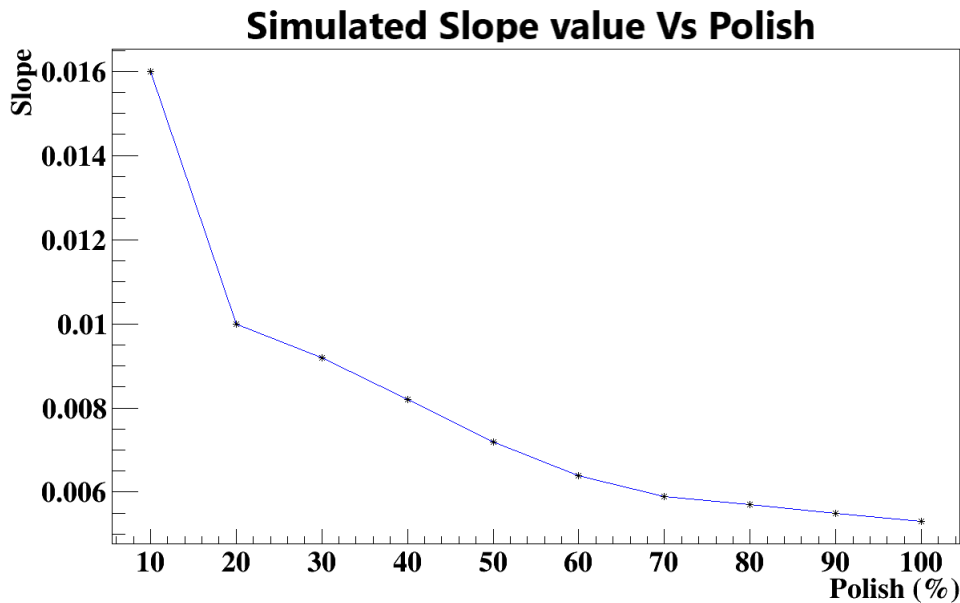


Figure 4.7: Simulated slope value (g) as a function of surface polish (%) (crystal surface treatment). The slope was calculated by applying a linear fit at different positions for a PTFE wrapping material with 97% reflectivity.

This effect was further tested using the UNIFIED mode in Geant4 simulations. As mentioned before, the σ_α parameter was available in this mode to set the roughness of the surface, and two values were explored (0.02, 0.2) for the same 97% reflective PTFE-wrapped detector as shown in Figure 4.8. The former repre-

sents a nearly polished surface (blue line) and the later refers to a ground surface (red line). As expected, the light ratio distribution obtained from both simulated models showed that there was a position dependency. However, the model with the smaller σ_α value provided a lower variation of the ratio of the total signal detected compared to the model where the $\sigma_\alpha = 0.2$. The latter model showed that by increasing the roughness of the surface, a steeper slope can be obtained.

The g values were found to be 0.003 and 0.0069 for σ_α of 0.02 and 0.2 respectively, and the light ratio detected at one of the extremities increased approximately by 18% when the σ_α was increased. Both models the GLISUR (Figure 4.7) and the UNIFIED (Figure 4.8) agree that by increasing the roughness of the crystal surface the expected g value increases. However, with the UNIFIED model, the experimental PTFE gradient (0.003 mm) was very well reproduced.

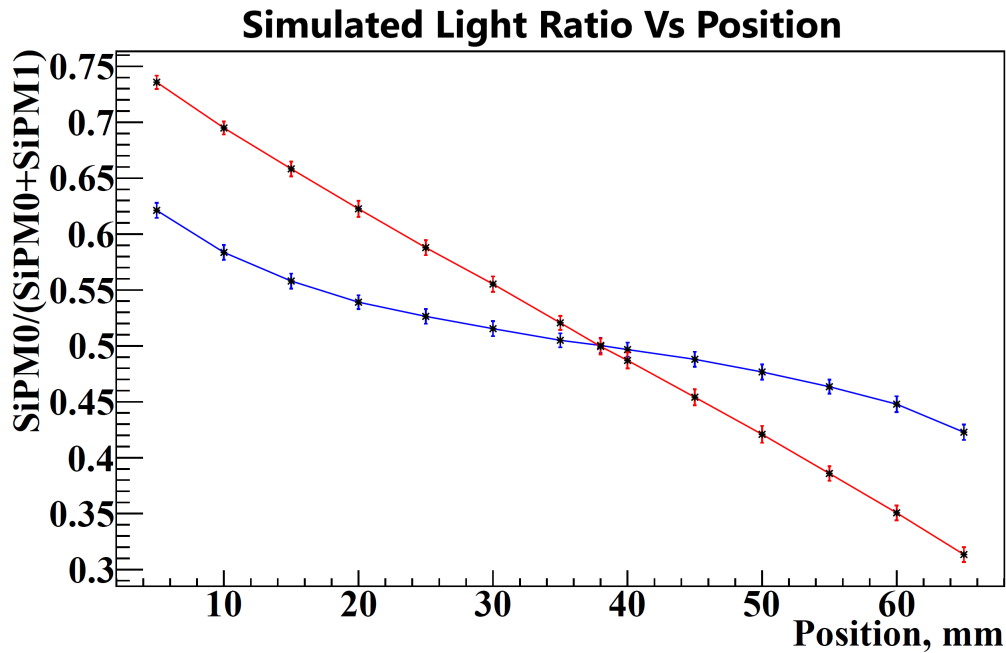


Figure 4.8: The simulated light ratio obtains as a function of the γ -ray interaction position at one end of the crystal (SiPM0) for two different σ_α values of the UNIFIED model. The blue line represents the data obtained for $\sigma_\alpha = 0.02$ (polished), and the red line represents $\sigma_\alpha = 0.2$ (rough).

Equation 3.2 was used, and it was found that an average of 5.3 ± 2.3 mm position resolution can be achieved using this model. The model also showed that by increasing the roughness of the surface ($\sigma_\alpha = 0.2 \text{ m}^{-1}$) a $2.3 \pm$, a 1 mm position resolution could be achieved.

4.2 3D Detector Results

4.2.1 Experimental Results

This subsection presents the results obtained from the cubic CsI:Tl crystal, which was read by six SiPM arrays. This was referred to as the main detector, while the auxiliary detector that was used for the coincidence measurements was referred to as the coincidence detector. Details of the experimental setup are in Section 3.1. The first results that were presented were the average 2D light maps from each SiPM array collected during pencil runs where no coincidence condition was applied. Then, the results of both average and single-event 2D light maps were shown for the coincidence measurements which constrained the interactions in the 3 dimensions.

4.2.1.1 Energy Measurements

The energy calibration measurements were carried out separately for each detector. Figure 4.9 shows that the coincidence detector identified almost double the number of photo-peaks compared to what the main detector could resolve. The main reason for this probably originated in the different number of SiPM pixels of the main detector (with the total number being 384) compared to that of the coincidence detector (64 pixels) and the corresponding contribution from the dark counts. A further reason could be a gain mismatch between the six different SiPM arrays of the main detector. The energy resolution for the main detector was found to

4.2. 3D Detector Results

be 9.0% at 662 keV. The energy resolution expected from a CsI:Tl scintillator is about 7%, but this can vary depending on, for instance, the size of the crystal and the wrapping material. The gain mismatch found between the six arrays could also have contributed to the energy resolution measured, and by correcting this mismatch the energy resolution may improve. As the main objective of this project was to explore the position sensitivity, this modest energy resolution of the main detector was not investigated further.

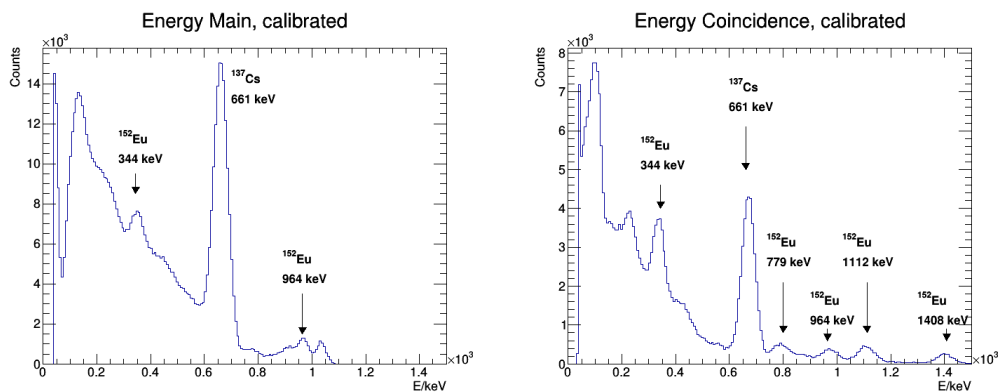


Figure 4.9: Energy spectrum of the main (left) and coincidence (right) detectors. The photopeaks of some of the lines of the ^{137}Cs and ^{152}Eu source are marked.

4.2.1.2 Experimental Average Light Maps

The measurements were carried out at various x , y , and z positions by utilising the Compton Scattering coincidence method described in Section 3.1 to characterise the main detector in terms of reconstructing the γ -ray interaction position.

4.2.1.3 Average Light Maps of Pencil Beam Runs

The average light maps showed, for each pixel, the sum of the signals collected for that pixel from all events, divided by the number of events. The following 2D average light maps showed average light distribution recorded without the coincidence condition, i.e. for the pencil beam runs. The light maps were produced by selecting the photons that originated from the γ rays that deposited their full

4.2. 3D Detector Results

energy (662 keV) in the main detector. This caused the first γ -ray interaction to lie along the direction defined by the pencil beam (i.e. the well-known x , y position), while the z position was not confined. However, the mean free path of 662 keV in CsI:Tl crystal was found to be around 2.5 cm, which means that the first γ -rays interaction was highly likely to occur at z positions that were near the γ rays entrance point. Figure 4.10 shows average light maps obtained from γ -rays interactions when the source is shining from the top side and in the middle of the crystal, which corresponds to x and $y = 25$ mm.

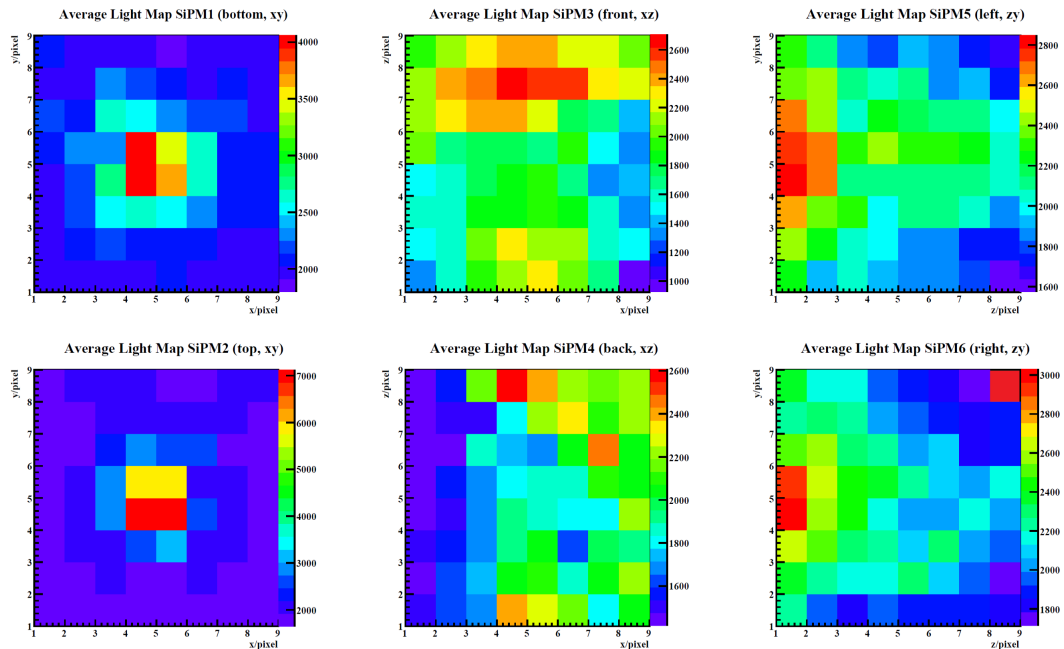


Figure 4.10: Average light maps for position $x = y = 25$ mm of the source for all six SiPM arrays of the main detector from the pencil beam runs. The colour scale axis represents the average value at the ADC.

The top and bottom SiPM arrays are labelled as SiPM 2 and 1 respectively. Both arrays show that the detected photons were distributed at the expected position in this case the center of the crystal. The left and right (SiPMs 5 and 6) arrays show the y and z coordinates of the photons detected (Figure 3.9 depicts the coordinates). The y coordinate is in agreement with the y obtained from SiPM 1 and 2, which shows that the source is hitting the detector in the middle. With the z coordinate which represents the depth of the crystal, the trend was different.

The intensity of the photons detected was found to be higher at small z values, and it decreased for the larger values, thus, demonstrating that more interactions occur close to the entrance of the surface. Thus, both SiPM 5 and 6 arrays showed the expected light distributions for this pencil beam run.

SiPMs 3 and 4, which are placed at the front and back of the crystal faces respectively, show the light distribution in the x and z directions (Figure 3.9 shows the coordinates). As expected, the light distribution is higher at the central region for the x values and continuously decreases for the z values as seen for the left and right arrays. However, SiPMs 3 and 4 were found to be less clear than SiPMs 5 and 6. The suggested reason for this is that the optical grease was less at the top region of the SiPM arrays, and with time, it moved towards the bottom. This agrees with what was observed in the 2D average light maps where the light distribution detected at SiPM 3 and SiPM 4 are more clear at large z values (towards the bottom). The effect of the unevenly coupled SiPMs become more prominent when the number of the detected photons at the pixels are low. To overcome such an effect a gain-matching calibration can be performed.

This gain-matching was carried out relative to SiPM5 and SiPM6 where the light maps were obtained from both arrays as shown in Figure 4.10, and they showed that the expected light distribution, when using the pencil beam runs, have no bias on coincidence geometry. For example, γ rays that enter from the top-middle of the detector should induce the same light distribution on all of the four SiPMs that are placed on the sides (front, right, back and left). This is also the case for the pencil beam runs where symmetry was used to gain-match SiPM 3 and SiPM 4 relative to the other two arrays. An example of such gain-matching performed for SiPM 3, 4 and 6 at $xyz = 25$ mm is shown in Figure 4.11 where the γ rays can be seen entering from the top-middle of the detector and should induce the same light distribution on all of the four SiPMs that are placed on the sides (front, right, back and left).

The gain-matching was applied to each pixel of the arrays using SiPM5 (z and y) as the reference for the gain values. It became clear that by applying such a correction the lightmap distribution was more evident compared to the non gain-matched case shown in Figure 4.10. As mentioned before because there were no coincidence conditions applied, and due to the strong attenuation of the γ rays in the CsI:Tl crystal, the intensity of the interactions was maximum, and thus, the photons were detected at the upper region of the detector. This gain-match correction was applied to all of the experimental data measured and presented in Section 4.2.

4.2. 3D Detector Results

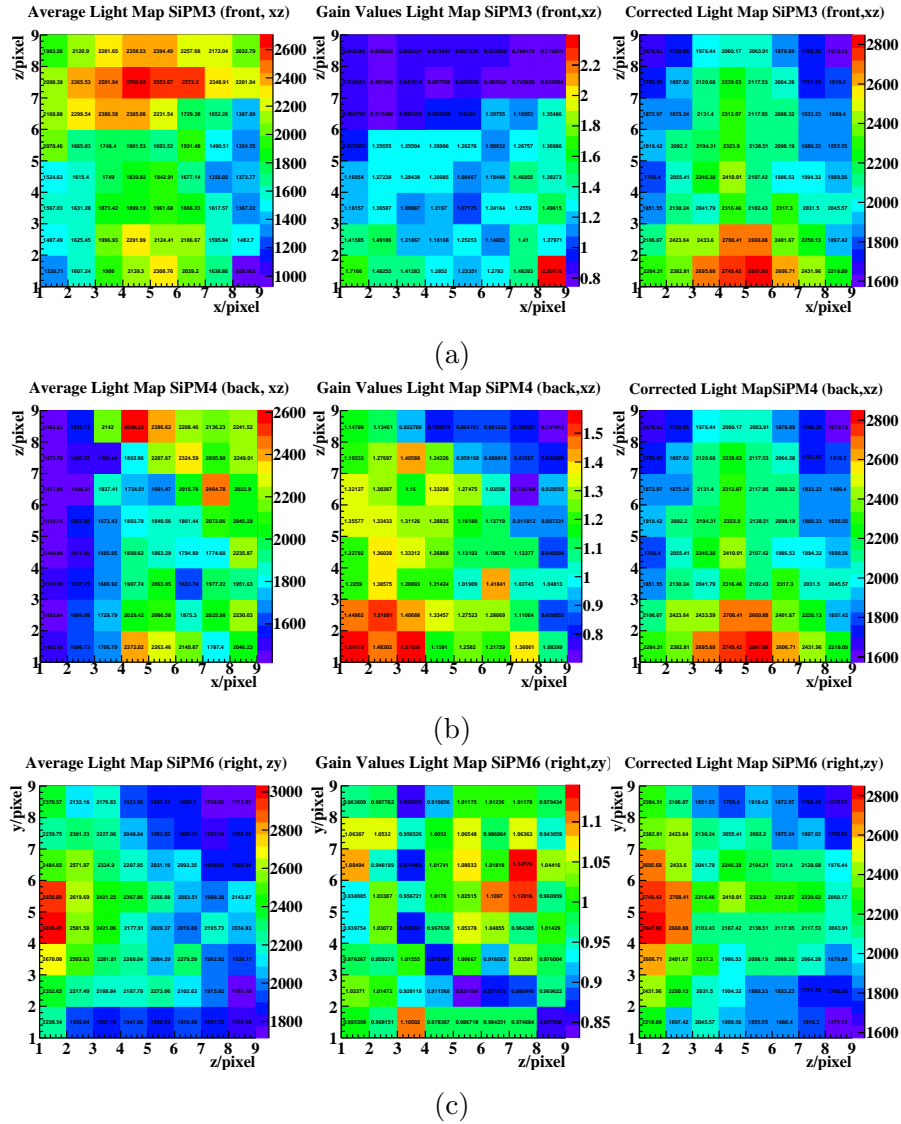


Figure 4.11: The raw experimental average light maps for SiPM 3, 4 and 6 are shown in the left column. The gain corrections obtained and applied to SiPM 3, 4 and 6 are shown in the middle column and the final obtained gain-matched light maps are shown in the right column of the figure. The light maps obtained are for pencil beam runs with the source illuminating at the middle of the detector $x = y = 25$ mm.

4.2.1.4 Average Light Maps with the Coincidence Condition

In the following description, the events that were recorded by using the coincidence condition are presented. The sets of coincidence position measurements together with the total events (total number of all events) and coincidence events (number

4.2. 3D Detector Results

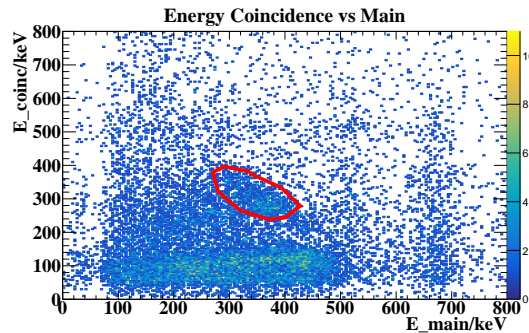
of events that scatter inside the main detector with a 90° angle) and that are recorded by the DAQ system are listed in Table 4.3. The x, y and z columns represent different γ ray interaction positions in all of the three coordinates. It is clear from the table that the number of the coincidence events decrease as the interactions take place further away from the slit collimator (x,y and z = 5 mm near the collimator's side).

Table 4.3: Number of coincidence and recorded events for several x, y and z positions are summarised here. x, y and z positions are given in mm

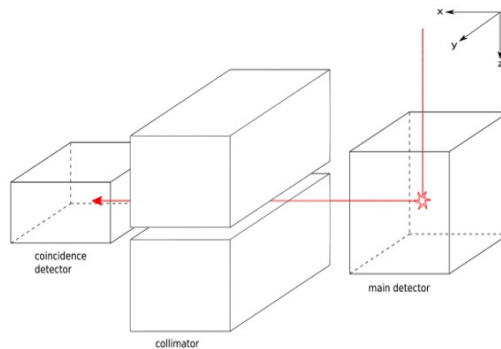
x	y	z	#recorded events	error (\pm)	#coincidence events	error (\pm)	percentage(%)
5	5	5	16205	127	1700	41	10.5
5	25	5	18687	137	2284	48	12.2
5	45	5	32163	179	3910	63	12.2
25	5	5	28608	169	1190	35	4.2
25	25	5	24742	157	966	31	3.9
25	45	5	30527	174	1186	34	3.9
25	25	25	32364	180	1023	32	3.2
45	5	5	36271	190	1085	33	3.0
45	25	5	26815	164	849	29	3.2
45	45	5	43132	208	1342	36	3.1
45	45	45	16106	127	273	17	1.7

For this setup, only those events with the expected energy deposition of about 374 keV in the main detector and the remaining 288 keV in the coincidence detector-based on the Compton formula were taken into account. Figure 4.12 illustrates the energies of the two detectors plotted against each other when x, y and z are equal to 25 mm. The events that are within the red cut were used to extract the interaction position.

4.2. 3D Detector Results



(a)



(b)

Figure 4.12: (Top) The detected energy in the coincidence detector vs. the detected energy in the main detector for position $x = y = z = 25$ mm. The cut on the coincidence events is shown with a red circle, which represents the events that scatter inside the main detector with a 90° angle. (Bottom) sketch showing the setup and indicating at which position the main detector was hit.

Although the energy sharing corresponding to the 90° scattering coincidence events is visible in Figure 4.12, other coincidence events with lower energy deposition in the coincidence detector were also detected. In Figure 4.12 where x, y and $z = 25$ mm, the red cut contains information about the scattered coincidence events inside the main detector with a 90° angle by applying a 2D gate.

Figure 4.13 shows 2D average light maps for all 6 SiPM arrays for x, y and z at 25 mm. Comparing this to the light maps shown in Figure 4.10, an overall enhancement was observed for all 6 SiPM arrays except for SiPM 4, which is attributed mainly to the non-uniform light coupling. Although the collimator should limit the interactions to those that take place at x, y and $z = 25$ mm, SiPM 2 shows a more narrow light distribution compared to the opposite array

4.2. 3D Detector Results

(SiPM 1). This is a result of the γ rays entering from the top side (SiPM 2) and causing interactions near the top of the crystal that still manage to reach the coincidence detector. As a result, there will always be some interaction that occurs above this point, enhances the average light maps seen by SiPM 2 and diffuses the light maps seen by SiPM 1. Looking at SiPM 3, 4, 5 and 6, the light distribution detected is not as narrow as SiPM 2.

The 2D light maps can also be used to resolve multi-hit events that occur as the γ rays escape towards the coincidence detector. As shown in Figure 4.12, the coincidence detector is placed towards the left side of these light maps (large x pixel number), so a γ ray manages to reach the coincidence detector or scatters through this part of the detector. This can also partially explain the enhancement observed for larger x pixel numbers.

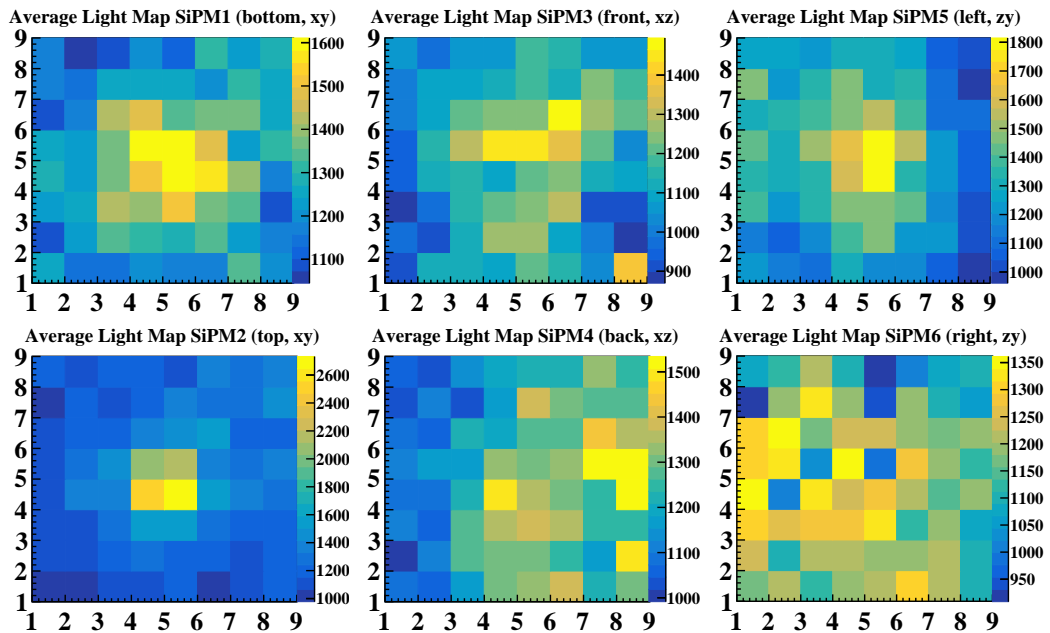


Figure 4.13: Average light maps after gain-matching applied for position $x = y = z = 25$ mm for all SiPM arrays of the main detector with the coincidence condition for the trigger and an energy cut on the coincidence events. Pixels coloured yellow represent the highest number of photons detected, whereas the blue coloured pixels denote the lowest number.

4.2. 3D Detector Results

Another position is presented where $x = 5$ mm, $y = 45$ mm and $z = 5$ mm. As shown in Figure 4.14, the interactions occur near the detector corner that is close to the collimator (larger x values). The energy correlation plot between the two detectors is cleaner compared to the energy correlation plot shown in Figure 4.12. Moreover, the red cut contains more evident coincidence events detected at the energy ranges selected. This can be attributed to the fact that the γ rays travel a minimum distance through the detector volume minimising any secondary scattering.

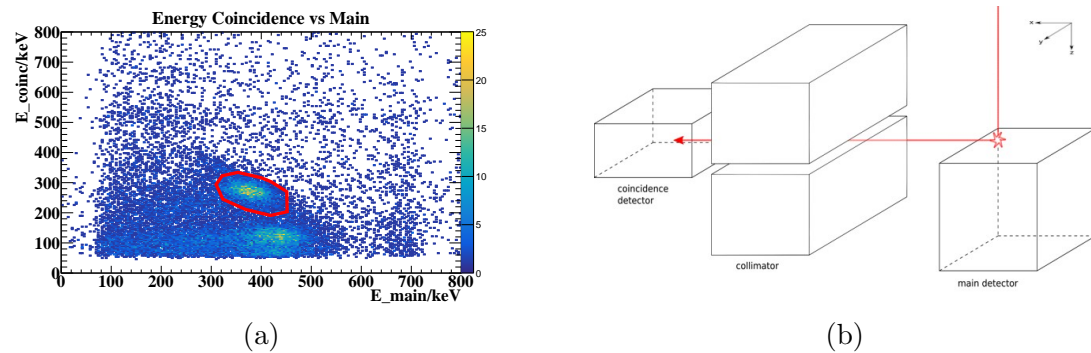


Figure 4.14: (left) Detected energy in the coincidence detector vs. detected energy in the main detector for position $x = 5$, $y = 45$, $z = 5$ mm. The cut on the coincidence events is pictured with a red circle. (Right) Sketch showing the position at which the main detector was hit.

Figure 4.15 shows the 2D light maps obtained from the above interaction position. It shows that the arrays near the interaction sites (SiPM 2, 4 and 5) see much higher light intensities and show much narrower light distribution compared to SiPM 1, 3 and 6 which are located further away from the interaction site and opposite to this corner. However, the information about the interaction position can still be resolved from the latter SiPM arrays. The light distribution seen by pixels 8, 8 and 1 (x,y,z) for SiPMs 2, 4 and 5 respectively were found to be 2-3 times higher than the blue plateaus.

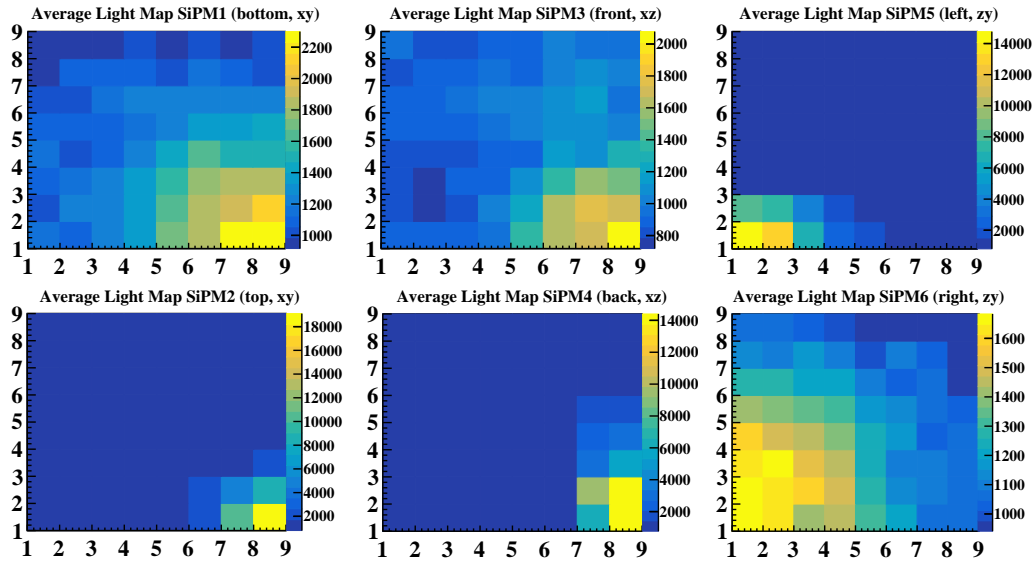


Figure 4.15: Average light maps for position $x = 5$, $y = 45$ and $z = 5$ mm for all SiPM arrays of the main detector with the coincidence condition (gain-matching correction applied) for the trigger and an energy cut on the coincidence events.

4.2.1.5 Single Events Interactions Light Maps with the Coincidence Condition

In Figure 4.16, the aim was to examine the event-by-event light distribution from a single γ -ray interaction at $x = 5$, $y = 45$ mm and $z = 5$ mm (at one of the detector top corners) inside the crystal with the coincidence restriction applied. This location corresponds to locations in front of SiPM arrays 2, 4 and 5. By comparing these individual events light maps with the average light maps, it is clear that the former are much more sparse. For events near the surfaces of the detector, where the SiPMs are located, there is indeed a very prominent signal induced at the SiPM pixels nearby. Such signals can often be more than 20 times higher than the signals detected by the rest of the SiPM pixels. As a result, identifying the position interaction became relatively obvious.

Looking at pixels 8, 8 and 1 (x,x,z) for SiPMs 2, 4 and 5 respectively, the light distribution was found to be 30-40 times higher (red coloured) than the blue plateaus. The opposite SiPM arrays 1, 3 and 6 also detected photons, and the number of photons detected were less than the number of photons detected by the

4.2. 3D Detector Results

other three arrays. The light maps also showed that more than one hit can be visualised, for instance, the signals detected by SiPM 6 array. This indicates that the 2D light maps obtained from such configuration provide a visualisation tool that can be used for detecting multiple hits inside the detector.

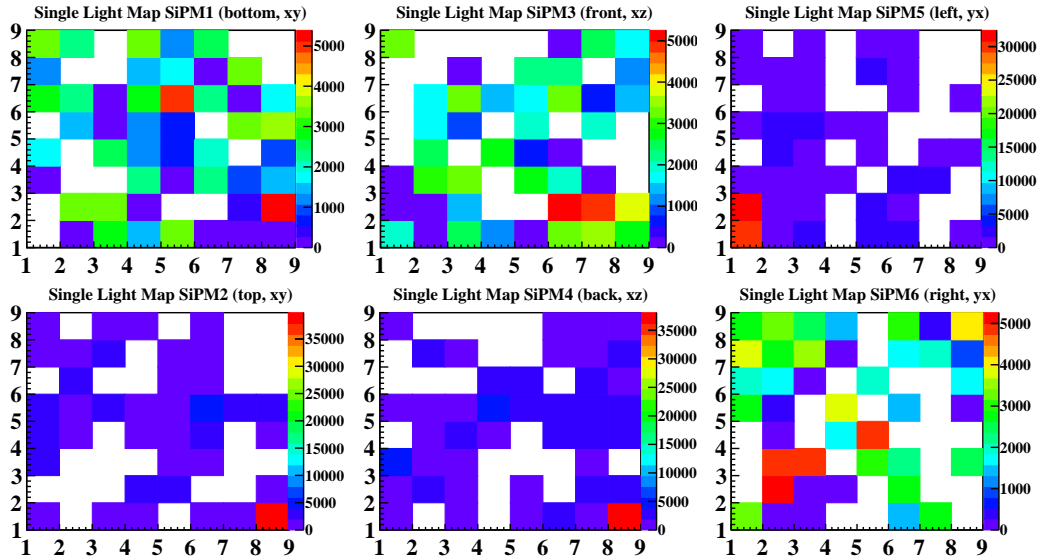


Figure 4.16: The light maps obtained for a single event at position $x = 5$, $y = 45$ mm and $z = 5$ mm for all SiPM arrays of the main detector with the coincidence condition after gain-matching correction was applied for the trigger and an energy cut on the coincidence events.

Interactions that are located further inside the detector (i.e. x , y and $z = 25$ mm) became less obvious and harder to distinguish as the scintillation light was shared between more pixels, as seen in Figure 4.17. In the selected event shown in Figure 4.17, SiPMs 3, 4 and 5 show multiple pixels with high intensity which may have been caused by a second γ ray's hit. In these plots, The threshold is at about 1000 ADC channels, which corresponds to 9-11 photons (for interactions near the top, front and left arrays) and 4-5 photons (for interactions near the bottom, back and right arrays).

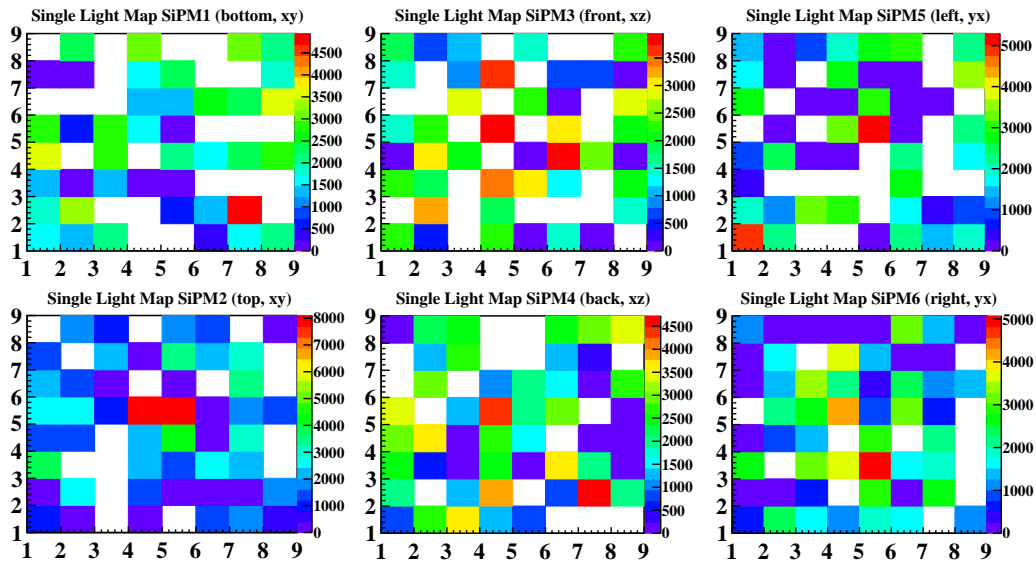


Figure 4.17: The light maps after gain-matching was applied were obtained for a single event at position $x = y = z = 25$ mm for all SiPM arrays of the main detector with the coincidence condition for the trigger and an energy cut on the coincidence events. SiPM 3, 4 and 5 show more than one γ ray's hit.

4.2.2 Simulation Results

Table 4.4 illustrates the interaction positions simulated in this work, which are spread over the entire detector volume. For each position, the γ rays were simulated, and the total number of the coincidence events that managed to go through the side collimator and be detected at the coincidence detector are also shown in Table 4.4.

By comparing the number of coincidence events shown in Table 4.3 and Table 4.4, it can be understood that both show a correlation between the number of recorded events and the locations of the interactions. Moreover, the further the incident or scattered γ rays have to travel through the crystal, the more likely they are to scatter again or be absorbed, and hence, the coincidence percentage reduces in these cases. Figure 4.18 shows the number of single coincidence events recorded at different interaction positions (Appendix Table A.6 has more details) throughout the main detector. Again, as seen in the experiment, it is clear that there is a correlation between the number of single coincidence events and the

4.2. 3D Detector Results

length of the path that the γ rays travel through the detector volume before being scattered to the coincidence detector.

Table 4.4: Number of coincidence events for a total number of 10^{10} simulated events at different x, y and z coordinates. x, y and z are in mm.

x	y	z	#coincidence events
5	5	5	539,912
5	5	25	364,898
5	5	45	193,629
5	25	5	546,728
5	25	25	379,302
5	25	45	204,152
5	45	5	540,025
5	45	25	365,084
5	45	45	193,416
25	5	5	136,165
25	5	25	115,775
25	5	45	73,731
25	25	5	138,602
25	25	25	125,977
25	25	45	83,024
25	45	5	136,059
25	45	25	116,026
25	45	45	73,764
45	5	5	35,050
45	5	25	37,000
45	5	45	28,174
45	25	5	33,276
45	25	25	37,966
45	25	45	30,951
45	45	5	34,793
45	45	25	36,877
45	45	45	28,058

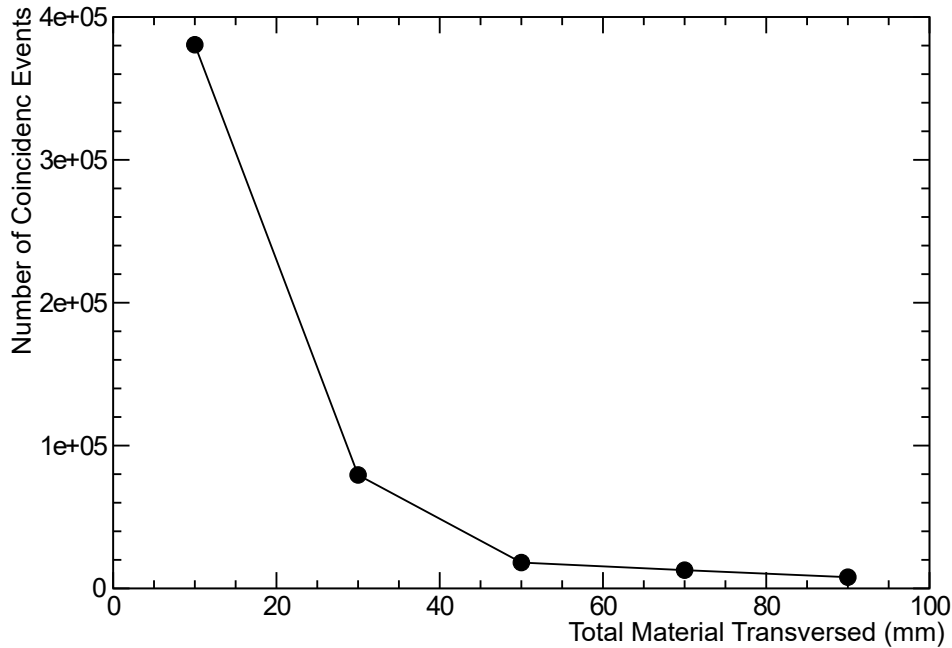


Figure 4.18: The image illustrates the number of simulated single scattering coincidence events recorded at different positions. It also shows that the longer the path traversed by a γ ray through the main detector before being detected at the coincidence detector for different $x+z$ coordinates, the fewer were single coincidence events that were recorded.

The energy sharing (2D-gated events) between the main and the coincidence detector were also examined for three different positions x , y and $z = 5$ mm, x , y and $z = 25$ mm and x , y and $z = 45$ mm as shown in Figure 4.19. The three plots show the 90° Compton scattered events which are represented by the “blob”, and as seen in the experimental results, other scattered events were also visible around the desired region. Moreover, looking at the plots from top to bottom the more material, the γ rays have to traverse through the main detector before interacting or escaping to the coincidence detector the less well-defined this Compton scattered events “blob” becomes. The bottom image shows two “blobs” at different energies, which indicates that there a second set of Compton scattered events. The simulated coincidence energy for the second “blob” was found to be around 297 keV, which is within the angular coverage measured from the experimental set up using the coincidence technique .

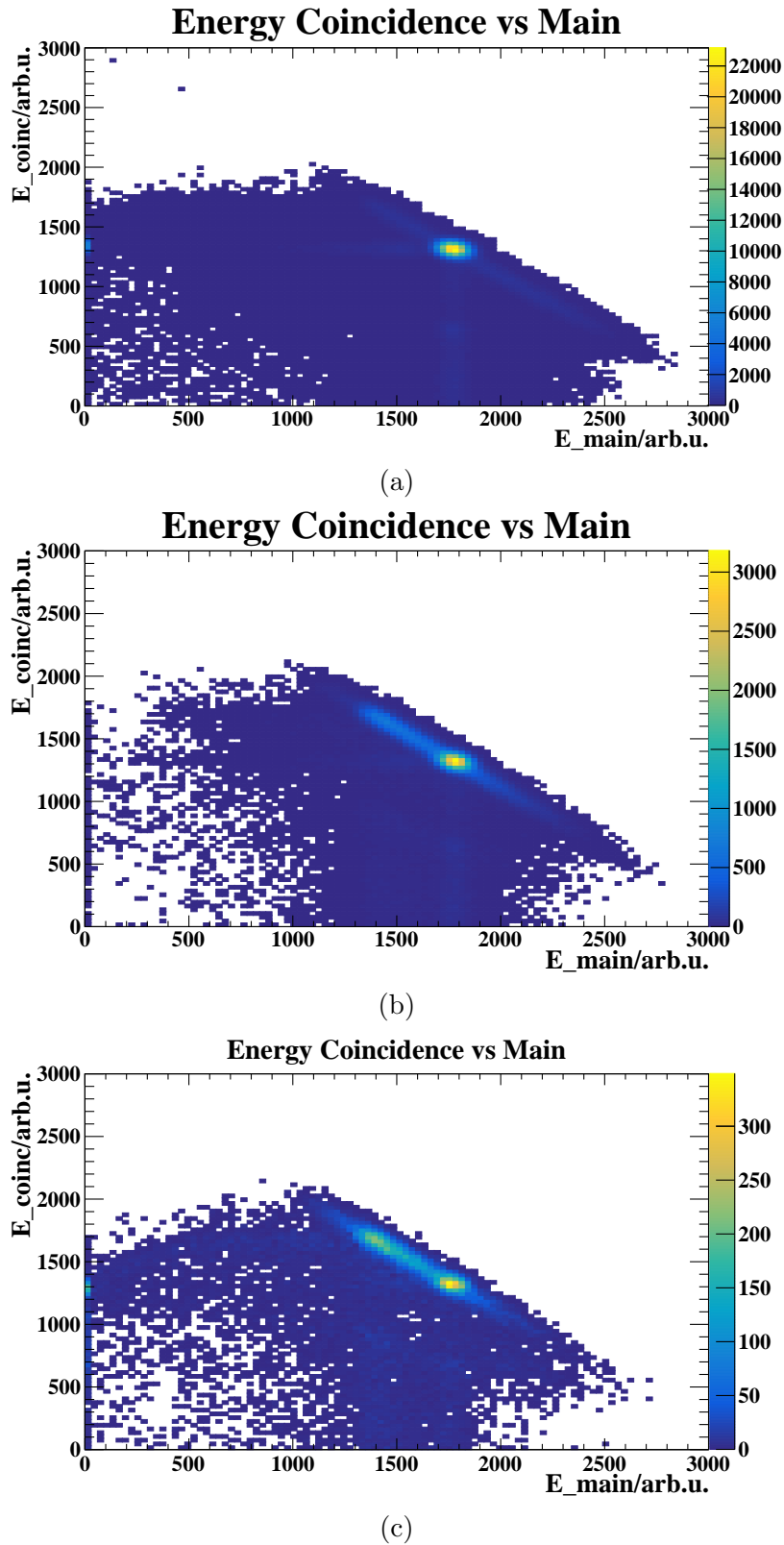


Figure 4.19: Energy deposited in the coincidence detector vs. energy deposited in the main detector for simulations of the position x , y and $z = 5$ mm (top), x , y and $z = 25$ mm (middle), and x , y and $z = 45$ mm (bottom). For interactions at x , y and $z = 45$ mm, the Compton scattered events “blob” becomes less well-defined.

4.2. 3D Detector Results

In Figure 4.20, the average light maps for the position $x, z = 5$ mm and $y = 45$ mm (simulation coordinates $x = 0$ mm, $z = -20$ mm and $y = -20$ mm) were examined and compared with the average light maps shown in Figure 4.15 (experimental results). Similarly, light maps that were a product of a single γ -ray interaction were also examined as shown in Figure 4.21 and were compared with Figure 4.16 obtained from the experimental results. Both simulated average and single light maps for different interaction positions are in good agreement with the light maps obtained from the experimental results. As speculated from the experimental results, the average light maps obtained from SiPM 2, 4 and 6, which are closer to the collimator show a more localised interaction position compared to the average light maps obtained from the opposite SiPM arrays.

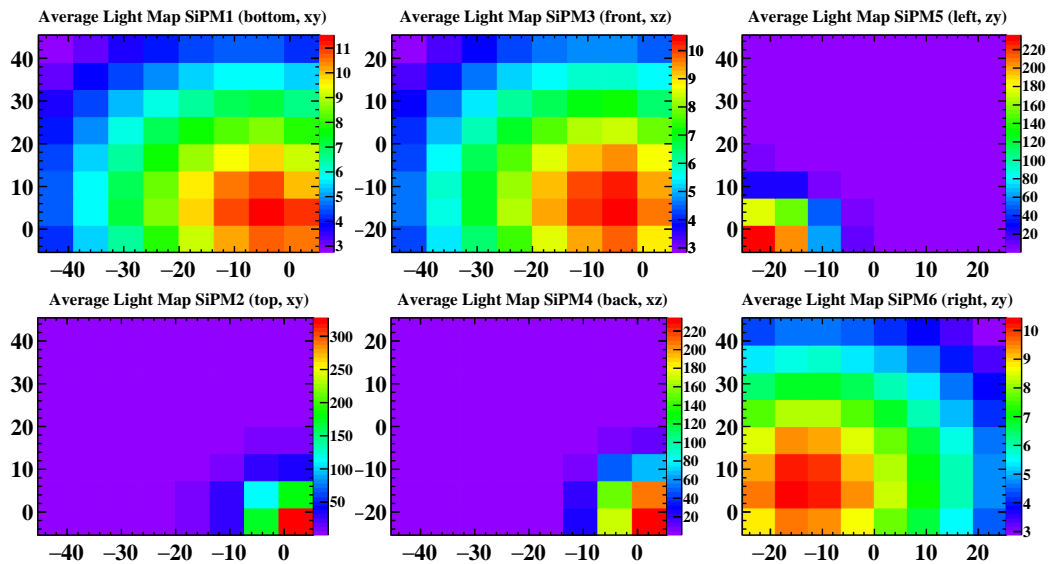


Figure 4.20: Simulated average light maps for all SiPM arrays of the main detector. The detector was hit at $x = 5$ mm, $y = 45$ mm and $z = 5$ mm (simulation coordinates $x = 0$ mm, $z = -20$ mm and $y = -20$ mm). Photons are represented in the colour code.

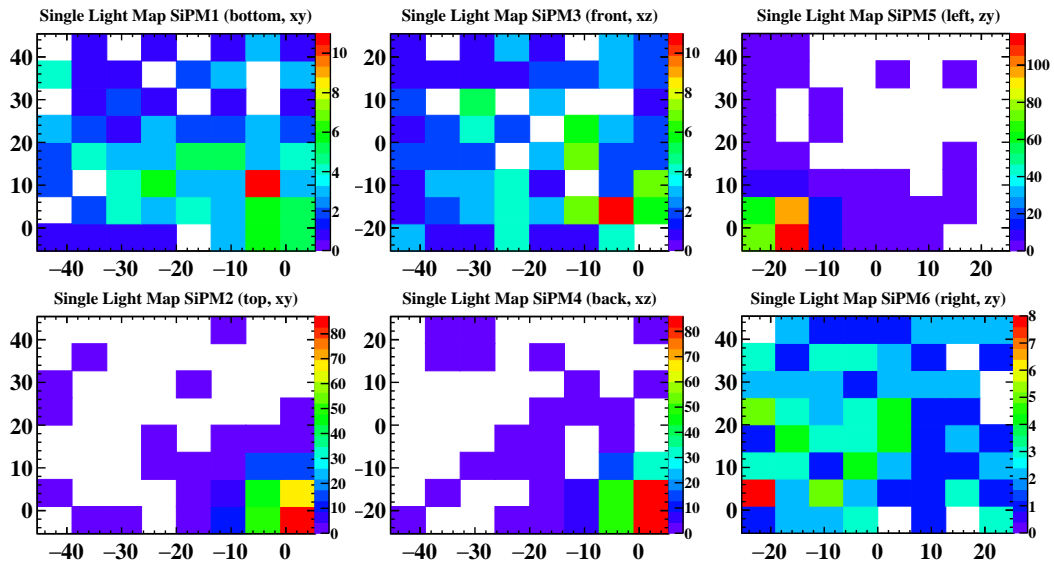
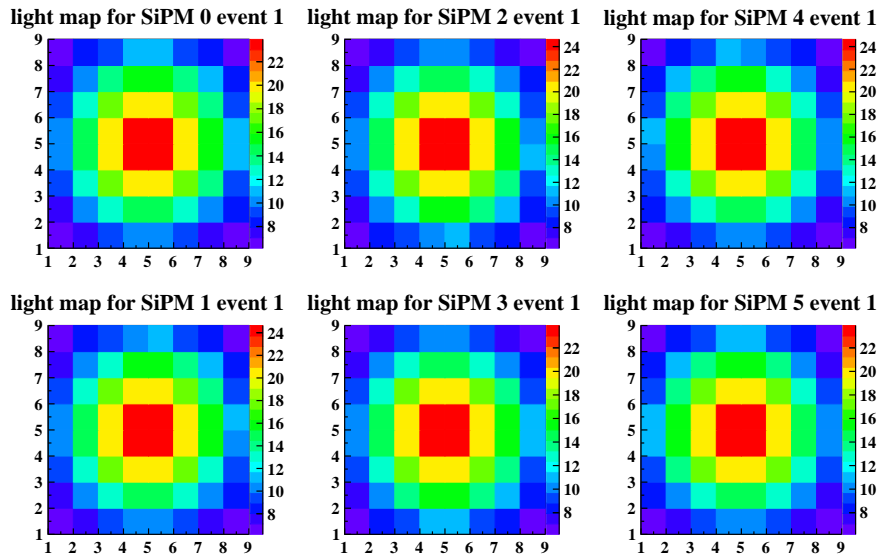


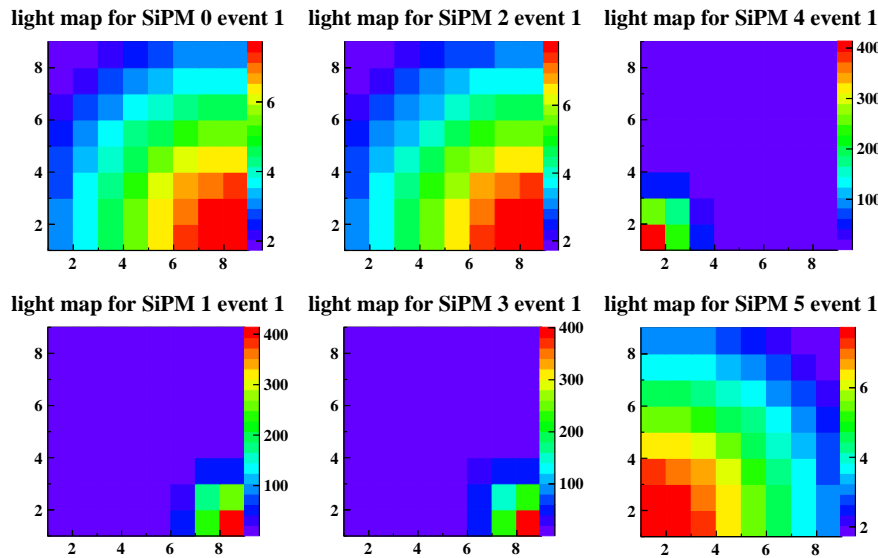
Figure 4.21: Simulated single-event light maps for all SiPM arrays of the main detector. The detector was hit on the back, left and top corner (position $x = 5$ mm, $y = 45$ mm and $z = 5$ mm). Photons are represented in the colour code.

4.2.3 Simplistic Model Results

In this simplistic geometric model, the light sharing between the SiPMs pixels was studied based on the solid-angle coverage of the pixel relative to the interaction point (distance r and angle between interaction and pixel). As mentioned in Section 3.1, Equation 3.6 was developed, which not only depends on the distances between the interaction position and the pixel location, but also takes into account other factors such as the number of photons that the scintillator yields and the fraction of light that the photo-detector can detect (PDE), and it adjusts for the non-perpendicular incident angles that impinge the pixels. The γ -rays interaction for x, y and $z = 25$ mm and $x, z = 5$ mm and $y = 45$ mm are shown in Figures 4.22a and 4.22b respectively, and the light maps generated certainly captured the dominant effect. The light maps generated by such a simplistic model were compared with both experimental and simulation results, and they showed that the light maps from interactions that occur in the middle and at the corner of the detector can be reproduced with this model and that this trend is the same as in the experimental and simulation light maps.



(a)



(b)

Figure 4.22: The images illustrate light maps generated from a single event interaction using the Simplistic Model for (a) position x , y and $z = 25$ mm and (b) for $x = 5$ mm $y = 45$ mm and $z = 5$ mm.

4.2.4 Experimental vs. Simulation and Simplistic Models Results

Figure 4.23 illustrates a comparison between the average number of photons detected by each SiPM, either experimentally or calculated from the simulation or

4.2. 3D Detector Results

the simplistic model. The interaction position coordinates x , y and z were set at 5 mm for all three methods. In each case, the top, front and left SiPM arrays detect a higher number of photons compared to the other opposite three arrays. This too relates to the distance that the photons have to travel inside the crystal to be detected, and in this case, the position of interaction is closer to the arrays as shown in Figure 4.23. The figure also shows that the minimum average number of photons detected experimentally are between 4-5. On the other hand, the minimum number of average photons predicted by the simulation and the simplistic model was approximately 1. This discrepancy may be a result of SiPM saturation, or it may be affected by the ADC range which, is not added to the models. Both simulation and simplistic models predicted a larger difference between the maximum pixels than was observed in the experimental data. Despite the differences described above, the general trends in the experimental light distribution are reasonably well reproduced by both the models.

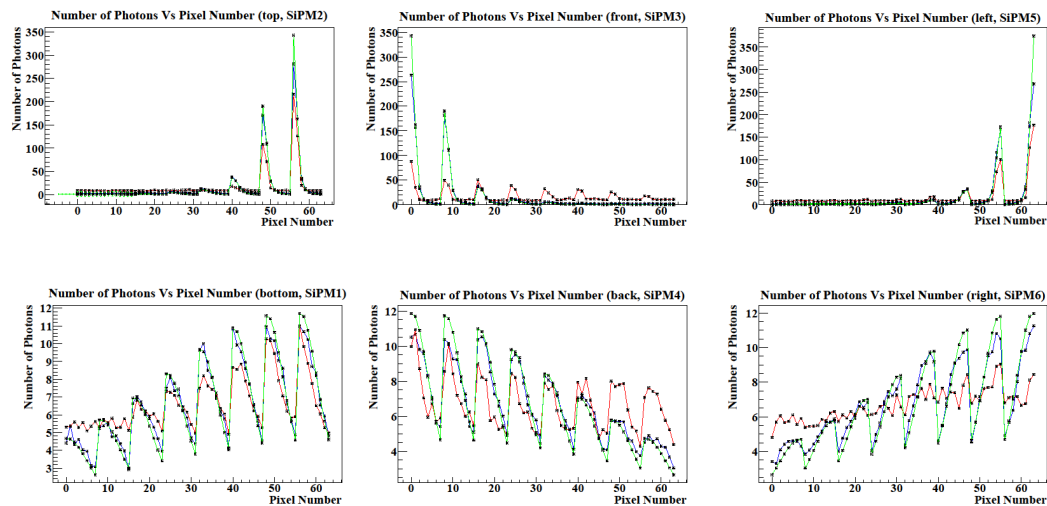


Figure 4.23: The images show the number of photons detected at each pixel of the six 8×8 SiPM arrays obtained from the simulation (blue), experimental (red) and simplistic (green) models data for position x , y and $z = 5$. Images at the top show the arrays that are near the interaction position. The images at the bottom show the arrays that are far away from the interaction position.

4.2.5 Position Reconstruction Methods

The light ratio method presented in Section 3.1 was used for the 3D detector for localising the γ -rays interaction positions by measuring the light ratio detected by the opposite SiPMs arrays using Equation 3.1. Figure 4.24 shows the simulated light ratio distribution detected by the opposite SiPM arrays at three different locations in the detector volume (left, middle and right). As a result of this method, the simulation indicated that there is a correlation between the interaction position and the estimated light ratio. As shown in the figure below, the Geant4 simulation model worked well in reconstructing the interaction positions using the ratio method. This adds to the confidence that the model's predictions can be used for reconstructing interaction positions.

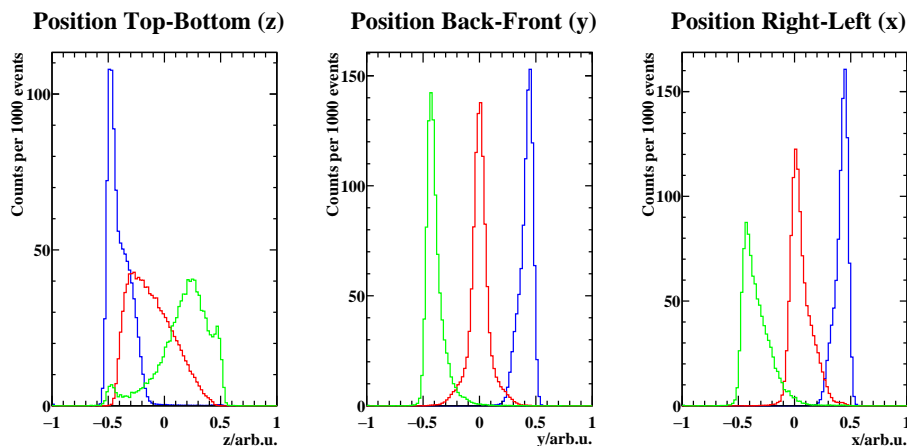


Figure 4.24: Simulation: z (left), y (middle) and x (right) position determined from the ratio of the light deposited in the two opposite SiPM arrays. The distributions are shown for the three positions as follows: interaction at x , y and $z = 5$ mm (blue), x , y and $z = 25$ mm (red) and x , y and $z = 45$ mm (green).

The same method was applied to the experimental data at two different interaction positions (x , y and $z = 25$ mm and $x = 5$ mm, $y = 45$ mm and $z = 5$ mm), and the results are shown in Figure 4.25. A discrepancy between the experiment and simulation was observed when using this method to reconstruct the interaction position. The light ratio method using the experimental measurements showed that there is a very weak dependency on where the γ -rays interaction po-

sition in the detector occurs. From a and b in Figure 4.25, it can be seen that the light ratio distribution measured at the different interaction sites is not sensitive to the interaction position, and thus, the position of interaction cannot be resolved when using such a method. For example, it was expected that an interaction at x , y and $z = 5$ mm would show that the bottom, front and left arrays detect a higher light fraction compared to the top, back and right arrays as in the case of the simulation model in Figure 4.24 (blue labeled). However, the light ratio measured by the three SiPM pairs is the same, and no change was observed. It is important to note here that there are some factors that accompany the experimental measurements that were not added to the simulated model such as the dark current and threshold effect. These factors can affect the comparison.

4.2. 3D Detector Results

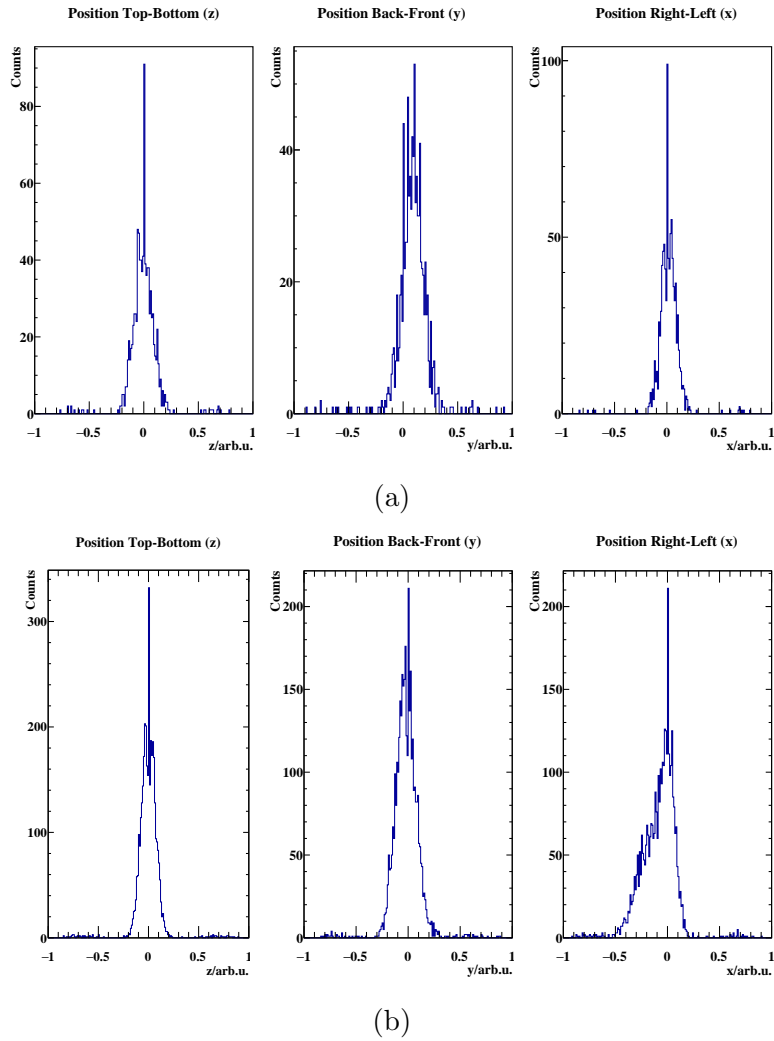


Figure 4.25: The light ratio distribution calculated from the total signal from the opposite SiPM arrays at (a) $x = y = z = 25$ mm and (b) $x = 5$ mm, $y = 45$ mm and $z = 5$ mm for z (top/bottom SiPMs), y (back/front SiPMs) and x (right/left SiPMs).

Due to this observed discrepancy, an alternative approach was adopted by taking the ratio of the individual pixels with the maximum detected light at opposite SiPM arrays. The outcome of this approach was successful, and the light ratio distribution using only the SiPMs pixels with the maximum light was found to be sensitive to the interaction position as shown in Figure 4.26.

4.2. 3D Detector Results

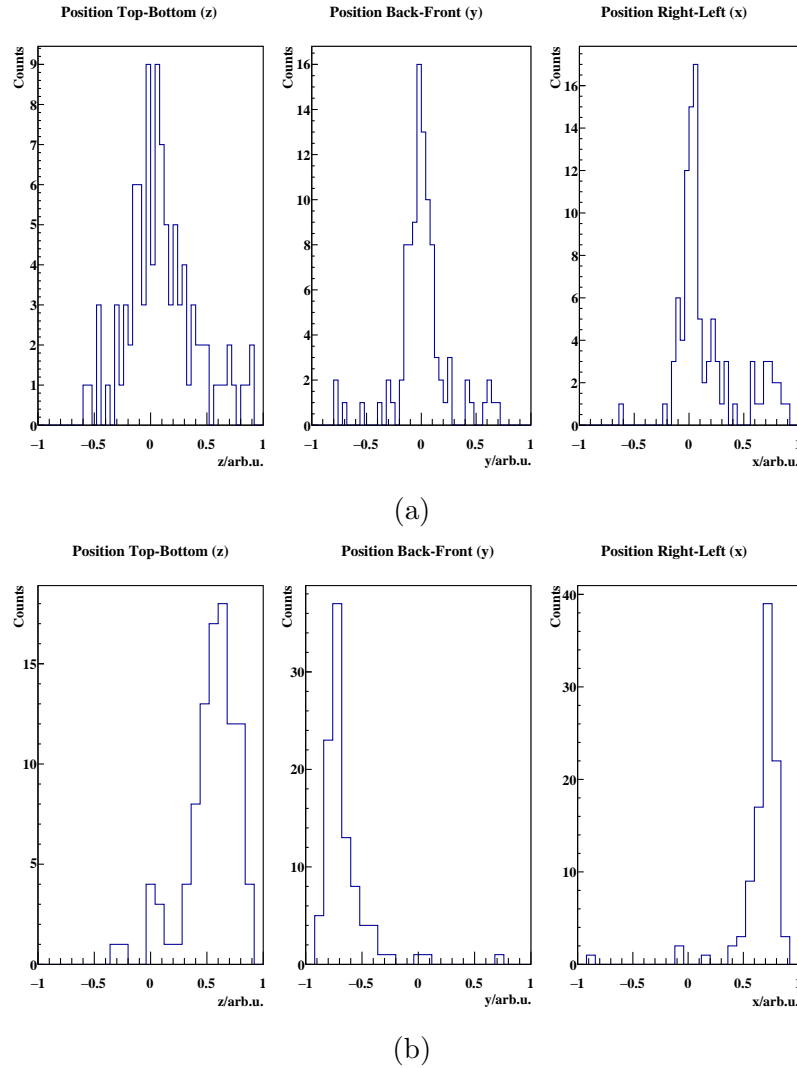


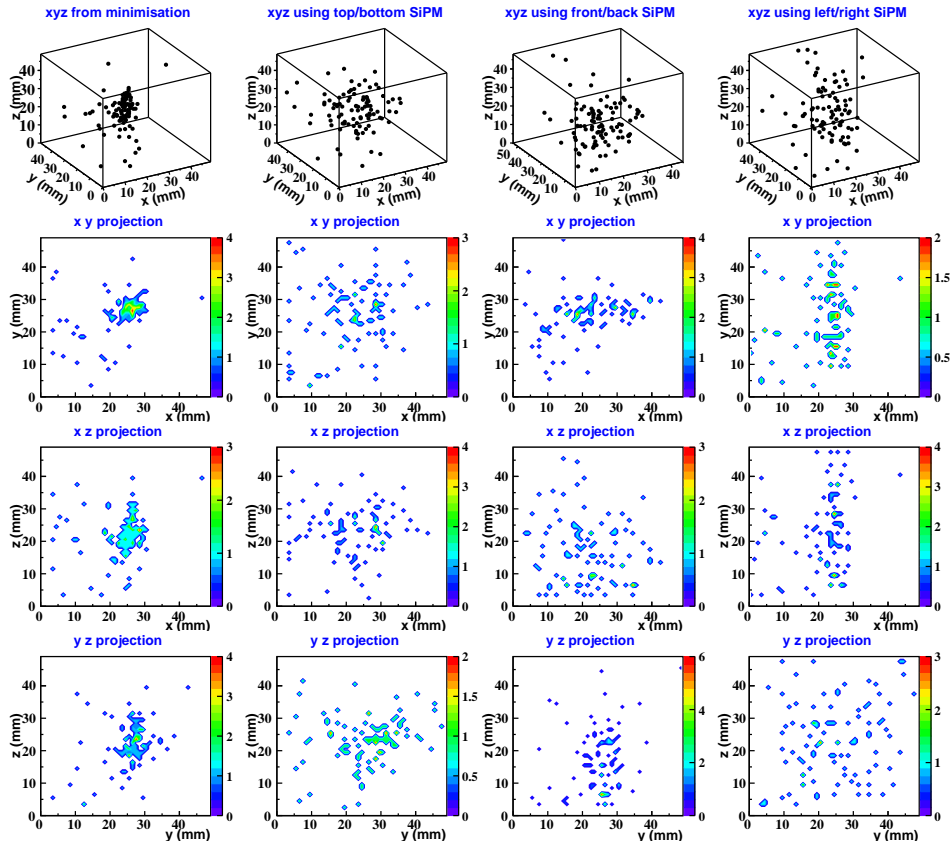
Figure 4.26: The light ratio distribution calculated from a single pixel from opposite SiPM arrays (a) at $x = y = z = 25$ mm and (b) at $x = 5$ mm, $y = 45$ mm and $z = 5$ mm. z (top/bottom SiPM max pixel), y (back/front SiPM max pixel) and x (right/left SiPM max pixel).

By applying light ratio method, using the pixels with maximum light in opposite SiPMs, it is possible to reconstruct the coordinates across the two opposite SiPMs. Moreover, by using the position of each maximum-light pixel on a given SiPM, the other two coordinates can also be reconstructed. Hence, from every pair of SiPMs one can extract all of the three coordinates. This is shown in the last three columns of Figures 4.27 and 4.28. Later a more sophisticated method was also applied, which entailed employing a χ^2 minimisation between the experimental and the predicted light maps as presented in Section 3.1. The output of the

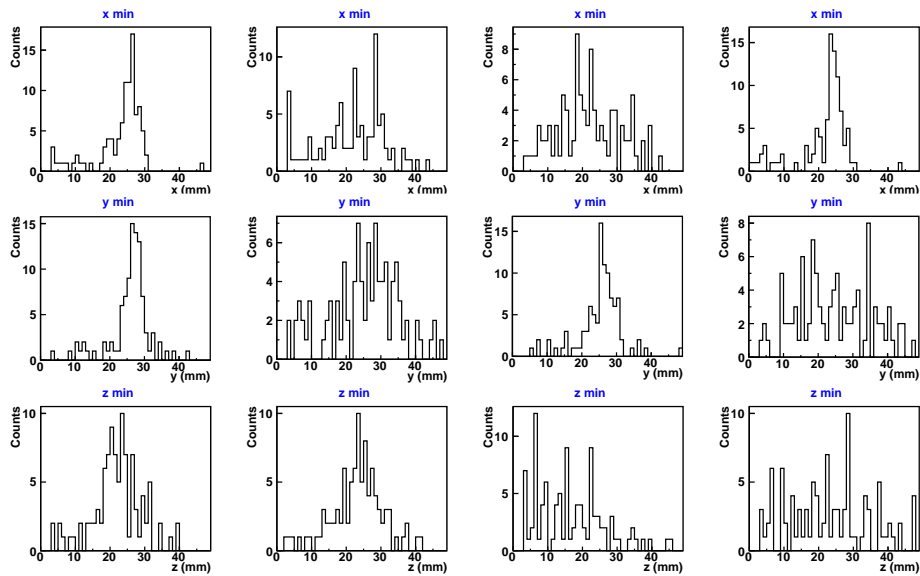
minimisation delivers the calculated x , y and z that matches best the experimental light maps. These three estimated coordinates are presented in the left column of Figures 4.27 and 4.28. The 2D projections for both the methods show that the interactions in the z direction spread slightly more than the interactions in the x and y directions. Figure 3.9 in Section 3.1 shows that position measurements in the z direction are restricted by a second slit collimator (4.5 mm wide). This is not the case for the measurements in the x and y directions. This may explain the slightly wider 2D projections seen in Figures 4.27 and 4.28 for interactions along the z axis.

In Figure 4.27 100 events were processed at x , y and $z=25$ mm, and by comparing both the methods, the χ^2 minimisation provided a more well-defined and narrower distribution for all of the three coordinates as shown in Figure 4.27a. In fact, the 1D projected positions from each method in Figure 4.27b show that for the x and y coordinates, the χ^2 minimisation provided a more Gaussian-like distribution, which was not observed while using the light ratio method. Looking at the top/bottom ratio in Figure 4.27a, a good position resolution in the z dimension can be achieved, but the resolution is poor in the x and y dimensions. Similarly, the front/back ratio works for the y but not for the x and z dimensions, whereas the left/right ratio works for the x but not for the y and z dimensions. This was expected as the light ratio method searches for the ratio of the most intense pixels in each of the pair's specific dimensions. On the other hand, the other two coordinates were calculated from the maximum light coordinates pixels.

4.2. 3D Detector Results



(a)



(b)

Figure 4.27: Event-by-event position reconstruction for the x, y and $z = 25$ mm position using the coordinates obtained from each of the pairs of SiPMs. The left column is the χ^2 minimisation method using the simplistic model. The next three columns are the coordinates obtained from each pair of SiPMs. SiPM top/bottom, front/back and left/right were obtained through the light ratio of the maximum pixel on opposite SiPMs.

The same methods were used for the 3D position reconstruction at $x = 5$ mm, $y = 45$ mm and $z = 5$ mm as shown in Figure 4.28. Again, the χ^2 minimisation provided a more narrow distribution compared to the light ratio method. This also shows that the interactions that are close to the edge of the detector are better reconstructed than interactions that occur far away from the coincidence detector (interactions further inside the detector volume) as shown in Figure 4.27. This can be attributed to the fact that interactions close to the edges take into account the position of the pixels with the maximum light intensity, which improves the reconstruction of the 3D interaction position. This can also be linked to the solid angle coverage where the closer the interactions are to the pixels the higher the solid angle coverage becomes, which increases the number of photons detected.

Figure 4.29 shows the reconstructed events for a γ ray pencil beam entering at $x = 45$ mm and $y = 5$ mm. The capability of the two methods to reconstruct the interaction position using the pencil runs data was tested where no coincidence condition was applied. The x and y coordinates are well reconstructed at the expected position throughout the depth of the crystal. The results show that the z coordinate spans almost throughout the entire crystal depth as expected from the pencil beam runs 2D lightmaps shown in Figure 4.10. It is important to note that the γ -ray attenuation length in CsI:Tl crystal is about 2.5 cm, which means most of the interactions occur at the top layer of the entrance, which explains the exponential attenuation observed.

4.2. 3D Detector Results

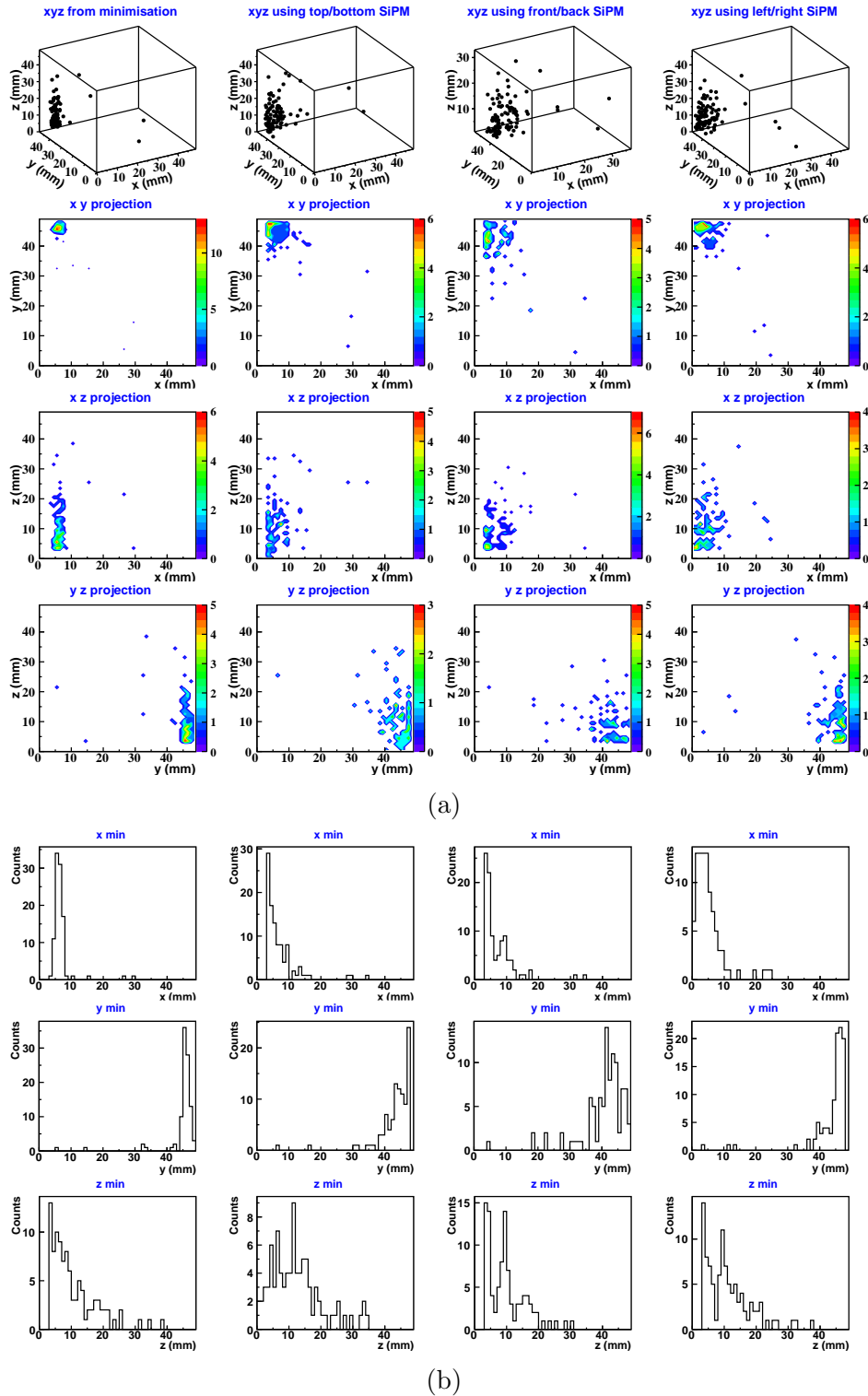
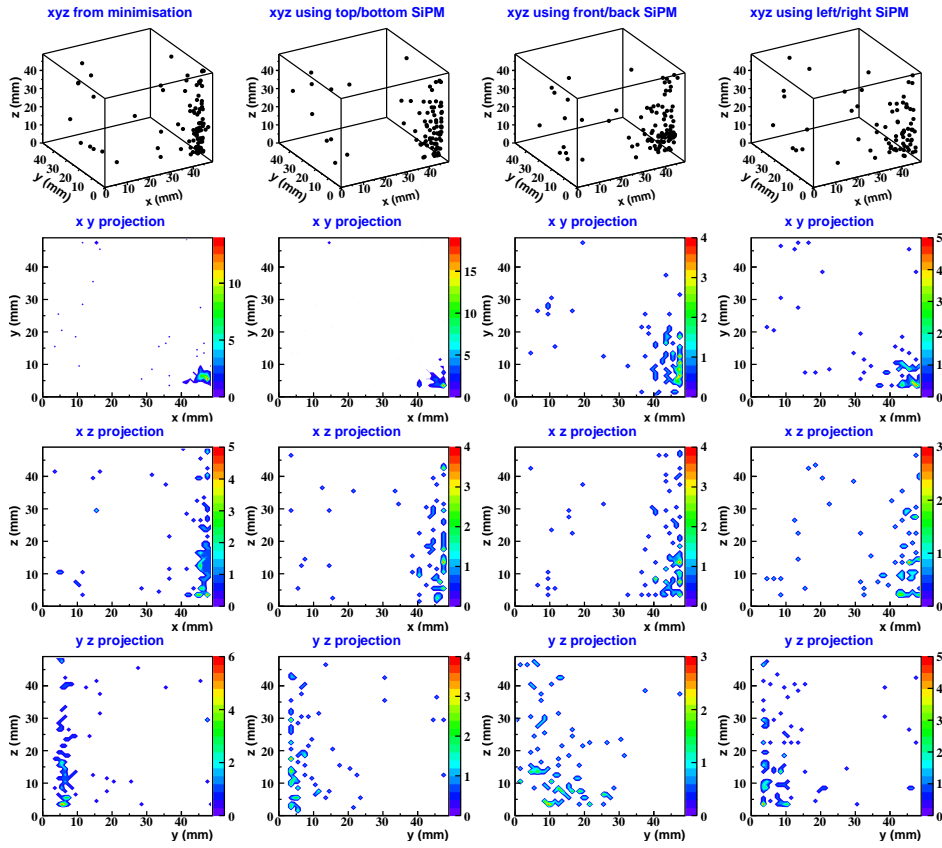
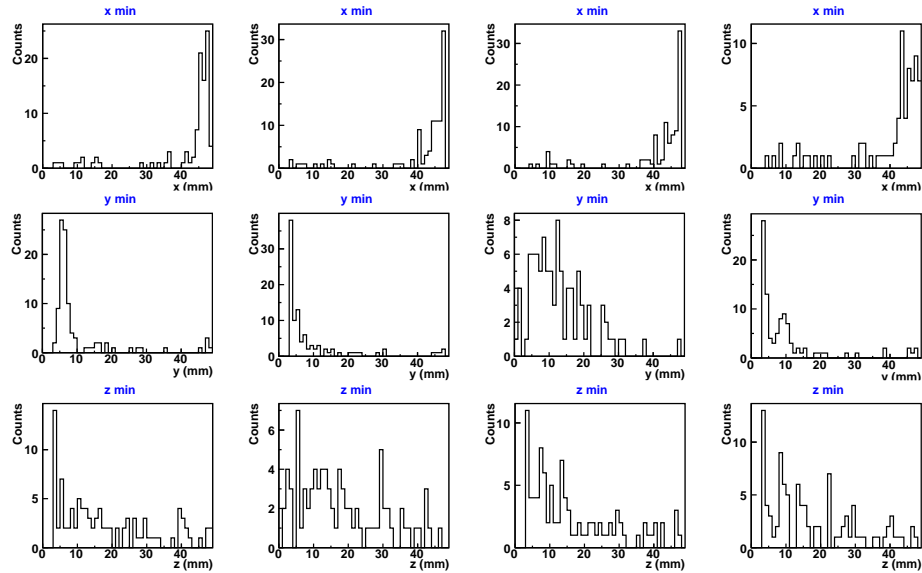


Figure 4.28: Event-by-event position reconstruction for the x, y and $z = 5$ mm and $x = 5$ mm, $y = 45$ mm and $z = 5$ mm positions using the coordinates obtained from each pair of SiPMs. The left column is the χ^2 minimisation method using the simplistic model. The next three columns are the coordinates obtained from each opposite SiPM pairs. SiPM top/bottom, front/back and left/right are obtained through the light ratio of the maximum pixel on opposite SiPMs.

4.2. 3D Detector Results



(a)



(b)

Figure 4.29: Event-by-event position reconstruction for a γ -ray pencil beam entering the crystal at $x = 45$ mm and $y = 5$ mm and interacting at any depth (any z) with different reconstruction methods. The left column is the minimisation using the simplistic model. The next three columns are the coordinates obtained from each opposite SiPM pairs, i.e. SiPM top/bottom, front/back and left/right through light ratio of the maximum pixel on opposite SiPMs and through its position on the SiPM.

4.2. 3D Detector Results

The position resolution was quantified by measuring the RMS width of light distribution for each of the reconstructed coordinates. Table 4.5 summarises the position resolution that is obtained when using the above methods at different interaction positions. The position resolution for χ^2 minimisation method was calculated to be 1.4 mm and 2.3 mm RMS at edges and the central region of the crystal respectively. The position resolution for the same regions when using the light ratio method was found to be 2.6 mm and 3.7 mm RMS respectively. Although the χ^2 minimisation method provided a better position resolution throughout the crystal volume, both the methods were in good agreement in identifying that the interactions near the edges of the detector are more trivial than the interactions that occur in the central region of the detector volume.

Table 4.5: Indicative position resolution values obtained by measuring the RMS of the light distribution for each of the reconstructed coordinates. The resolution was measured for both the χ^2 minimisation and the light ratio methods light distribution at different interaction positions.

Interaction position	χ^2 minimisation RMS	Light ratio RMS
Edges of the crystal	1.4 mm	2.6 mm
Center of the crystal	2.3 mm	3.7 mm

For both the light ratio and the χ^2 minimisation method, an offset of 1 and 2 mm at the edges and central region of the detector are observed for the reconstructed positions. In the case of the light ratio method, the positions were reconstructed based on the assumption that there is a linear relationship between the light ratio collected and the position of interaction. However, as seen in the 1D detector, there are other factors that can affect the position such as the polishing of the crystal's surface and the wrapping material used, and this may cause the said deviation. For the χ^2 minimisation method, the offset simply shows that the modelling is not perfect, but it can still reconstruct the actual position vary well. This is so because the values of the offset are well within the position resolution of both the light ratio and the χ^2 minimisation methods, which provide simple

4.2. 3D Detector Results

analytical position reconstruction methods that can be used to reconstruct the γ -rays interaction position inside the detector.

Chapter 5

Discussion

This chapter discusses the results obtained from the 1D and 3D detectors. In Section 5.1, the experimental and simulation model results for the 1D detector have been examined, compared and explained. In Section 5.2 the 3D detector performance has been discussed. Both the simulation and simplistic models outcomes have also been discussed. Further, 3D position reconstruction methods and the position resolution values obtained from these methods have been reviewed.

5.1 1D Detector

The results shown in Section 4.1 were obtained from a 1D CsI:Tl detector wrapped with three different materials for energy and position resolution measurements. The aim of this experiment was to understand the effect of the wrapping materials on the detectors performance, testing the accuracy and alignment of the scanning table station for the position resolution measurements and exploiting the light ratio method for reconstructing the γ -ray interaction positions along the long axis.

The results of the energy resolution for the three different wrapping scenarios (black tape, PTFE and 3M ESR sheet) showed that the black tape provided the worst energy resolution of $14.3 \pm 0.2 \%$ at 662 keV compared to the other two materials. This was expected, as black tape is an absorptive material meaning that the optical photons that escape the faces of the crystal and reach the black tape are absorbed and only those photons that exit forwards and backwards of the crystal are detected. As a result, a degradation in the energy resolution due to statistical fluctuation was observed. In the other two scenarios where PTFE and 3M ESR were used, the opposite effect was observed and energy resolutions of $7.3 \pm 0.1 \%$ and $6.8 \pm 0.2 \%$ respectively were measured. The improvement of the energy resolution can be attributed to the increase in the number of photons reflected back into the crystal which reduced the statistical fluctuation. In Ref [75], two different wrapping materials were compared, a reflective material and an absorptive material for a $50 \times 50 \times 30 \text{ mm}^3$ cubic LaBr3:Ce detector. They found that the average energy resolution measured for the absorptive wrapped detector ranged from 8-16% depending on the interaction position compared to an averaged relative energy resolution of $3.8 \pm 0.04\%$ for the reflective wrapped detector. This shows that reflective material provides better energy resolution than an absorptive material which agrees with the findings of the work presented in this thesis.

The third wrapping material, which was a highly reflective 3M ESR sheet, showed a slightly better energy resolution. This material has a reflectivity of > 98 for wavelengths > 400 nm. and the majority of the emission spectrum from CsI:Tl is above this limit, it was expected that this wrapping material will perform well.

The average position resolution for the three different wrappings were also evaluated by using the light ratio detected at each SiPM placed at the two ends of the 1D crystal. Figure 4.2 demonstrates that there is a correlation between the γ -rays interaction position and the number of photons reaching each SiPM (PTFE-wrapped detector). In Figure 4.3, the PTFE-wrapped and black-tape-wrapping materials used for the same detector showed that the light ratio varies as a function of the interaction position. However, the light ratio measured by the 3M-ESR-wrapped detector showed no dependence on the interaction position. It was unclear whether this bad resolution was caused by bad light coupling of the SiPM or whether the reason was the specular reflection of the 3M-ESR-sheet. All of the different wrapping techniques that were applied too did not improve the position resolution. The black-tape-wrapped detector produced the largest variation in the light ratio, as a function of interaction position. The PTFE-wrapped detector showed less variation in the light ratio measured at the different interaction positions, which may be caused by the high degree of diffusive reflection at the faces of the crystal [75].

The average position resolution obtained from the three differently wrapped detectors were compared, and it was expected that the black-tape-wrapped detector would provide the best position resolution value according to Refs [75] [76]. However, in the measurements presented here, an average position resolution of $7.0 \text{ mm} \pm 2.9 \text{ mm}$ was achieved with the PTFE-wrapped detector compared to $8.7 \text{ mm} \pm 3.6 \text{ mm}$ for the black-tape-wrapped detector. From Equation 3.2 it was found that a good position resolution value can be achieved by a narrow light ratio distribution (low FWHM value) and a steep line fit, which provides higher gradient (g) values. By considering these two parameters for all of the

three wrapped detectors, the g value was found to be 0.005 mm and 0.003 mm for the PTFE- and black-tape-wrapped detectors, whereas the FWHM was found to be 0.01 and 0.04 respectively. Although the slope of the black tape was higher than that of the PTFE slope, the less light detected by the former worsened the FWHM. This contributed to the slightly enhanced position resolution achieved by the PTFE-wrapped detector. The g value obtained from the linear fit for the 3M-ESR-wrapped detector was negligible, which lead to the worst position resolution measured among the other two detectors.

The PTFE-wrapped detector was modelled using the Geant4 simulation as shown in 4.1. In Figure 4.6, the simulation model showed that the light ratio varied depending on the interaction position and was in good agreement with the experimental data. However, the simulation model provided a finer position resolution of 5.3 ± 2.3 mm compared to the $7.0 \text{ mm} \pm 2.9$ mm measured experimentally. Although the detectors components, surface treatments and the scintillator properties were implemented in the code, some factors that could affect the position resolution measurements experimentally were not included in the code such as electronics noise. However, both the experiment-related and the simulation data showed that using the light sharing method for a 1D CsI:Tl double-sided read-out detector can also be used for reconstructing the γ -rays interaction position along the detectors long-axis.

Simulation was also used to examine the effect of roughened crystal surfaces on the position resolution. The faces of the CsI:Tl crystal used for the 1D detectors configuration were not roughened which increased the chance of photons being trapped and reflected back into the crystals where the incident angle equalled the reflected angle as shown in Figure 2.8. Several studies were carried out to investigate the effect of surface roughening finishes on the position resolution, and it was reported that improvements can be achieved in the position resolution using such methods [77, 78]. One such study showed that by using the bonds-etching method at the four sides of the crystal, the position resolution improved from

9.1 mm to 3.4 mm. Another group compared different crystal dimensions for two different roughening techniques. The saw cut and then mechanically etched the surfaces. They found that by increasing the depth of the roughening on the scintillator surface, an average position resolution of approximately 1.6 mm can be achieved [79]. However, their findings varied depending on the scintillator's cross-section and showed that the best position resolution can be obtained when using a small cross-sectional crystal.

This concept was tested using the PTFE-wrapped simulated detector by changing the smoothness of the crystal surface using the GLISUR model. The CsI:Tl scintillator surface roughening treatment was evaluated for its effect on the gradient of the light ratio distribution. It was found that the more the crystal's surface was roughened (changing the percentage of the polish), the g increased. As mentioned before, to obtain a good position resolution when using Equation 3.2, a high g value and a small FWHM value is required. Hence, based on the simulation findings, it can be said that using a roughed surface crystal wrapped with diffusive material enhances the gradient value, which, by default, enhances the position resolution.

A PTFE-wrapped detector with a roughened surface was modelled to compare its position resolution with a fully polished detector. Based on the simulation, the crystal with the roughened surface ($\sigma_\alpha=0.2$) provided a 2.3 ± 1 mm position resolution which outperformed the $5.3 \text{ mm} \pm 2.3$ mm position resolution obtained when using a fully polished crystal ($\sigma_\alpha=0.02$). This enhancement can be attributed to the increase in the gradient value where 0.003 and 0.05 mm values were obtained for the polished and the roughened crystal surface respectively.

The 1D detector provided a good estimation when measuring position resolution using the light sharing method. For both energy and position resolution measurements, the PTFE wrapped detector provided better performance compared to the other two detectors. The simulated model showed good agreement with the experimental position resolution measurements as shown in 4.1. This shows that

the model can be used for estimating the γ -rays interaction positions, and its flexibility for modifications can be used for modelling and optimising different detector models. As shown in 4.1 the PTFE-modelled detector showed that roughening the crystal surface improved the position resolution by the same factor reported in [77] and gave a lot of confidence that the simulation model reproduces the improvement in the position resolution. Although the PTFE-roughened surface detector provided a better position resolution value, an experimental validation is required to find the best surface-roughening technique.

The 1D experimental tests and simulation model have helped in the designing and modelling of the 3D detector. The simple configuration of the 1D detector has provided an understanding of the effects of the wrapping material on both energy and position resolution. It has also provided a basic understanding about the light sharing method that was used for 3D position-reconstruction for γ -rays interactions in the 3D detector.

5.2 3D Detector

The use of a monolithic 3D cubic detector for resolving the γ -ays interaction position inside a CsI:Tl crystal was tested using different reconstruction methods. By summing the signals from all of the faces, the detector measured a modest energy resolution of 9.0% at 662 keV. In Figure 4.9, not all photopeaks are resolved compared to the coincidence detector. For the coincidence detector, only one SiPM array is attached to one face of the crystal, and the remaining faces are wrapped with PTFE, which increases the number of photons reflected back to the crystal-minimising statistical fluctuations. In the main detector case, all of the faces of the crystal are covered with SiPM arrays, and the photons that are generated are shared between all six arrays which adds contribution from the dark counts and possible gain mismatch between different SiPM arrays. The photons generated inside the crystal are distributed across a large number of pixels and the

total energy signal from each array is read out and processed individually which introduces a larger noise contribution that degrades the energy resolution.

Figure 4.10 depicting the distribution of the average light across the six arrays show that the information about the x and y position of interaction can be resolved when using the pencil beam runs. In these runs, no coincidence condition was applied meaning that the γ rays DOI are not constrained and the average light distribution spreads along the z axis. However, these runs provided valuable preliminary information regarding the detectors functionality and was also used to correct for any gain mismatch between the pixels.

A symmetrical light distribution was expected to be detected by all 4 SiPM arrays placed at the sides of the crystal for γ rays entering from the top-middle of the detector. However, a variation was observed in the number of the photons detected at each pixel of the six arrays, which may be caused by an unevenly spread optical grease applied between the SiPM arrays and the crystal. This can also be a result of the read-out mechanism where, in this study, each pixel was read-out and processed individually, which may lead to gain variation. However, by implementing a gain-matching factor, this effect was minimised, and the localisation of the interaction position becomes more evident.

Looking at both the average and single events and the light maps that were obtained from the experimental measurements and the simulation model, it is observed that the light maps provide a good 3D estimation of the interaction position when using such a detector configuration. The maps also show that the number of events vary depending on how far the interaction position is from the SiPM array. Table 4.3 and 4.4 present the number of coincidence events obtained from both experimental and the simulation data and show that the number of coincidence events that reach the coincidence detector decrease as the interaction position is further inside the crystal volume. This can be explained with reference to the distance that the γ rays have to propagate through the crystal volume before being absorbed or undergoing multiple interactions, which can degrade the

number of photons generated while reaching the SiPM arrays.

As each γ -ray interaction position within the crystal can be approximated as a point-like source of photons, the solid angle covered by each pixel can be used to estimate the number of photons detected at the SiPMs, and this can provide information about the x, y and z interaction position coordinates [33]. The developed simplistic model which was based on calculating the solid angle coverage at different interaction positions showed that the closer the interaction location is to one of the arrays, the higher is the solid angle coverage, which increases the number of photons detected. Both the simplistic and simulation models were in agreement with the experimental data. However, the simplistic and the simulation model showed higher number of photons from events taking place close to the SiPM arrays, compared to the experimental data. This discrepancy can be attributed to the fact that some factors such as the dark count that affects the detection process is not included in the models. The comparison also shows that the minimum number of photons that can be measured experimentally is 4-5 or 9-11 photons (depending on which array is close to the interaction site) due to the preset threshold, which is not applied to the models allowing them to detect lower values. Another important factor that must be taken into account is the photons behaviour at the boundaries between the media such as the one between the crystal and the SiPM arrays. As discussed in Section 2.3, the photons that travel between two different media with different refractive indexes may not all be transmitted but can be reflected, refracted or undergo total internal reflection depending on the incident angle. These interactions were included in the simulation model but were not included in the simplistic model, which may explain the slight difference between the two models concerning the number of photons detected.

In terms of 3D reconstruction, a χ^2 minimisation and the light ratio methods were tested, and their outcomes were compared. As mentioned in Section 5.1, the light ratio method depends on the signals detected by opposite SiPM arrays. This was first examined by the simulation model, which showed that the average

light ratio detected by SiPM arrays depends on the γ -rays interaction positions as shown in Figure 4.24. However, this dependency was not observed when implementing the same method on the experimental data as shown in Figure 4.25. As mentioned before, in Section 2.2, the CsI:Tl crystal has a slow decay time requiring the use of long integration time, making the detector system more prone to the SiPMs dark counts that are integrated together with the actual photons, which causes a discrepancy between the simulation model and the experimental data. To overcome this problem, the light ratio between two pixels that detect the maximum light and are located at opposite SiPM arrays are used to reconstruct the 3D interaction position, which provides a good interaction position estimation as shown in Figure 4.26.

To compare both the χ^2 minimisation and the light ratio methods, an event-by-event-position reconstruction was carried out for all three coordinates by processing 100 events from each run. In general, the two reconstruction routines proved to be effective and simple methods for reconstructing 3D position interactions in monolithic crystals. For the χ^2 minimisation method, the minimisation process was executed by using the simplistic model data, which showed that it can reproduce the actual γ -rays interaction position. However, it is important to note that it is essential to implement the correct detector dimensions and configuration to accurately mimic the actual detector response. Further improvements also require including photons that reflect back from the crystal surfaces and dark counts and setting minimum thresholds equal to the thresholds values of the experimental data. However, the effect of this is expected to be of secondary order compared to the solid angle effect which is already taken into account. The former effect can vary depending on temperature and the electronics used which can be adjusted and controlled. For the solid angle effect the coverage depends on the distance between the interaction position and the position of the pixel.

As mentioned in Section 4.2, the χ^2 minimisation method showed a more confined distribution compared to the light ratio method as shown in Figures 4.27

and 4.28. In fact, the same outcome is also observed when using the pencil beam measurements (no coincidence condition applied) as shown in Figure 4.29. This can be explained by the number of pixels that are used for each calculation method, where for the latter the light ratio is taken from two pixels with maximum light detected located in opposite SiPM arrays. The χ^2 minimisation uses signals that are detected by up to 384 pixels. Looking at the z coordinates for the non-pencil beams, a wider span was observed compared to the x and y coordinates, which may be an effect that arises from the side collimator. The side collimator was used for defining the depth of the interaction in the crystal volume as shown in Figure 3.9. As the width of the side collimator was measured to be 4.5 mm, there is a high probability of multiple scattered events that pass through the side collimator and reach the coincidence detector. This also explains the increase in the width of the reconstructed light distribution obtained along the detector's z axis.

The position resolution for both the methods were quantitatively compared, and it was found that the values differ depending on the interaction position. Interactions that occurred near the edges of the crystals were found to be 1.4 and 2 mm RMS for the χ^2 minimisation and the light ratio methods respectively. On the other hand, interactions that occurred at the central region of the detector were found to be 2.3 and 3.7 mm RMS respectively. From both the reconstruction methods, the best position resolution was obtained for interaction was the one that was near the SiPM arrays. This was expected, and it shows the same trend that was observed in the 2D light maps obtained from the experimental, simulation and simplistic models. The light ratio method provided the worst position resolution which attributes to the wider reconstructed light distribution when using such a method.

As mentioned in Section 1.2, there are many studies on 3D interaction position reconstruction methods that can be extracted from monolithic crystals, which provide different position sensitivities. These methods can vary from using different fitting methods to artificial intelligence (AI) such as neural network using

experimental or simulation data [80] [81]. Moreover, the use of different crystals, photo-detectors and configurations makes it difficult to carry out a comparison between these approaches. For example, in [69], an ANN was used to extract the 3D interaction position coordinates by examining the light ratio detected by individual SiPM pixels divided by the total signal of the whole array for two different types of scintillator detectors. They reported that for a 356 keV γ ray, an average position resolution of 2.9 mm for x and y coordinates and 5.2 mm FWHM for z coordinates can be achieved for a CeBr₃ crystal coupled to an array of 4×4 mm² SiPM 25×25×10 mm³ when using such method. They also measured the position resolution of a 28×28 LaBr₃:Ce based detector with the same thickness of the CeBr₃ scintillator and found it to be 8.0 mm FWHM for x and y coordinates, whereas for the z coordinate, the position resolution was 11.0 mm FWHM. Another group measured the average position resolution for a 33×33×10 mm³ GAGG (Ce) crystal coupled to an 8×8 SiPM array. They reported that a 1.7 mm FWHM for the x, y coordinates and 2.5 mm FWHM for the z coordinate can be achieved using the convolutions neural network (CNN) algorithm [82].

To our knowledge, to this date, this is the first device to use a six-sided SiPM-based read-out 50.44×50.44×50.44 mm³ cubic CsI:Tl crystal for extracting 3D γ -rays interaction position information. One advantage of covering all six sides of the cuboid CsI:Tl crystal with SiPM arrays was that with the use of such simple and quick reconstruction methods, the γ -rays interaction positions in all three dimensions were located. Another advantage is the absence of a reflective material that may reflect back any photons that escape the crystal which improves the energy resolution but can worsen the position resolution [75]. The use of black paint on some of the surfaces or an absorptive material were suggested by other groups to improve the position resolution measurements [75, 83]. However, such approaches degrade the energy resolution of the detector, as the photons are being absorbed by the black tape. This shows that there is a trade-off between the energy and the position resolution that must be taken into account when choosing the type of the wrapping material.

Although the position-reconstruction methods used for this research focused on searching single hits per event, the use of a six-sided readout system provided some redundancy in the sense that the same coordinate can be measured in three different independent ways and correlations between the different position-reconstruction methods show the possibility that this could be used for identifying multi-hit events. On the other hand, two-hit identification can be achieved by visually inspecting the SiPM arrays light maps as shown in Figure 4.17.

The developed 3D detector has shown that it can identify and resolve γ -rays interaction positions for both average- and single-interaction positions. The identification of the single-interaction events are of great interest when designing a Compton imaging device that can be used in the medical field, for nuclear security and in astronomy for localising the source position [84] [85] [86]. Both the Geant4 simulation and the simplistic model showed to be in good agreement with the experimental data which indicated that they can be used as reference grids and can be easily modified to explore and design future detection systems. Besides, the light-hit pattern of detected by the SiPM arrays, the light ratio method and the χ^2 analysis minimisation method also seem to be rather sensitive. Given that the position-reconstruction algorithms agree quantitatively with the experiment and provide simple and effective methods for position-resolution calculations, these methods can replace the experimental measurements, and this would save precious experiment-measurement time.

Chapter 6

Conclusion and outlook

In summary, two types of CsI:Tl detectors for γ -ray detection were developed and tested for position determination measurements. The $6\times 6\times 76.2$ mm CsI:Tl polished crystal coupled to 6×6 mm² SiPM at both extremities was tested for both energy and position resolution using three different types of wrapping materials. Of the three configurations, the 3M ESR coating exhibited the best energy resolution due to the increase in the statistical resolution that arises from the increased number of reflected photons. The position resolutions were obtained using the light sharing method, and it was found that there is a strong correlation between the interaction position and the light ratio that was detected. However, this correlation is directly affected by the type of the wrapping material. The position resolution was calculated for all three different wrapped detectors using the gradient from the linear fit line and the FWHM of the light ratio distribution. For the PTFE and black-tape-wrapped detectors, the position resolutions were found to be $7.0 \text{ mm} \pm 2.9 \text{ mm}$ and $8.7 \text{ mm} \pm 3.6 \text{ mm}$ respectively. For the 3M-ESR-wrapped detector, the interaction positions were not determined as there was no variation in the light ratio measured at the different interaction sites along the detector's x-axis. To achieve a good position resolution for such a detector's configuration, a narrow light ratio distribution (FWHM) and a high gradient value (g) are required. To

show a proof-of-concept of these two parameters the PTFE wrapped detector (with polished surfaces) was simulated using Geant4, and the model provided a 5.3 ± 2.3 mm average position resolution. The model also showed that by increasing the roughness of the crystal's surface, the position resolution can be improved. Approximately a 2 mm position resolution was achieved for a $\sigma_\alpha = 0.2 \text{ m}^{-1}$, which improved the gradient value from 0.003 mm for the polished surface to 0.05 mm for the unpolished surface.

The 3D detector, consisting of a $50.44 \times 50.44 \times 50.44 \text{ mm}^3$ cubic CsI:Tl crystal coupled to six 8×8 SiPMs arrays, was developed to be used for reconstructing the 3D γ -rays interaction positions inside the crystal volume using different reconstruction methods. The use of the 6-sided read-out showed that the 3D γ -rays interaction positions at different sites of the crystal can be simply resolved from the 2D light maps obtained from the single-hit events. Moreover, the Geant4 simulation and the developed Simplistic model provided similar results and showed high accuracy in localising the γ -rays interaction positions inside the detector volume.

The χ^2 minimisation and the light ratio methods worked well in reconstructing the γ -rays interaction positions in all of the three coordinates. Both methods showed that there is a correlation between the position of interaction and the reconstructed light distribution. The position-resolution was obtained by measuring the RMS of the σ of the light distribution. It was found to be 1.4 mm RMS for the χ^2 minimisation and 2 mm RMS for the light ratio method at the edges of the detector. On the other hand, 2.6 and 3.7 mm RMS position resolutions were measured in the central region of the detector using the χ^2 minimisation and light ratio methods respectively. While it is definitely possible to improve upon this result, both, in terms of a more sophisticated post-processing and an improved experimental setup, we do not anticipate a drastic improvement in the position-reconstruction itself. Nevertheless, the reconstruction will become more robust and straight forward.

In this work, the benefits of using such a configuration and a proof-of-concept of the models developed and the 3D reconstructing methods implemented have been described. Overall, the results are exciting, and the project has shown that the concept of position-reconstruction using both the methods for a six-sided read-out monolithic crystal is achievable. It has also provided quantitative information on the obtainable position resolution and extended the corresponding simulation and the simplistic model that can be used reliably to explore and design future detection systems. Such a detector can be used in many applications where the main goal is to localise the actual position of the source. For example, in nuclear security, this technology can deliver a compact and robust device with a very large field-of-view for a Compton Gamma Camera. In nuclear physics experiments, such a device can be of interest for Doppler-broadening corrections where it offers at least three independent ways to measure the same coordinate.

Following this work, there certainly is room for more testing and improvements. In particular, using other crystal materials that exhibit faster decay times for shorter integration time, which makes it less prone to SiPM dark counts and offers better energy resolution for more selective multiple scattering analysis. Other improvements include cooling of the detector to reduce SiPM dark counts, minimising the width of the side collimator, adding additional coincidence detectors (at different angles) to increase statistics and getting better databases and using a new, dedicated ASIC read-out system that allows to set the single pixel threshold even lower than the current level of 4-5 photons. The Geant4 simulation data can be used to construct a grid to optimise the position-reconstruction methods, which can then be used for a linear combination of more than one interaction to be implemented in the minimisation process. The light maps that were presented in this work are very suitable and can be used for Machine learning and AI methods for 3D position-reconstruction calculations.

References

- [1] Rodney J Hicks, Guy C Toner, and PETER FM Choong. Clinical applications of molecular imaging in sarcoma evaluation. *Cancer Imaging*, 5(1):66, 2005.
- [2] Sam T Donta, Richard B Noto, and John A Vento. Spect brain imaging in chronic lyme disease. *Clinical Nuclear Medicine*, 37(9):e219–e222, 2012.
- [3] Matthias Brendel, Federico Probst, Anna Jaworska, Felix Overhoff, Viktoria Korzhova, Nathalie L Albert, Roswitha Beck, Simon Lindner, Franz-Josef Gildehaus, Karlheinz Baumann, et al. Glial activation and glucose metabolism in a transgenic amyloid mouse model: a triple-tracer pet study. *Journal of Nuclear Medicine*, 57(6):954–960, 2016.
- [4] Multimodal neuroimaging analysis. <https://www.multimodalneuroimaging.wordpress.com/2015/04/28/c-positron-emission-tomography>. Accessed April 6, 2020.
- [5] Christian Ritzer, Patrick Hallen, David Schug, and Volkmar Schulz. Inter-crystal scatter rejection for pixelated pet detectors. *IEEE Transactions on Radiation and Plasma Medical Sciences*, 1(2):191–200, 2017.
- [6] T Omura, T Moriya, R Yamada, H Yamauchi, A Saito, T Sakai, T Miwa, and M Watanabe. Development of a high-resolution four-layer doi detector using mppcs for brain pet ieec nss and mic conf. *Record (Anaheim,)*, 2012.
- [7] Antonio J Gonzalez, Filomeno Sánchez, Pablo Conde, Sebastian Aussenhofer, Daniel Gareis, Roberto Pani, Rossana Pellegrini, Marco Bettiol, Andrea Fabri, Stan Majewski, et al. A novel brain pet insert for the mindview project. In *2014 IEEE Nuclear Science Symposium and Medical Imaging Conference (NSS/MIC)*, pages 1–4. IEEE, 2014.
- [8] Todd E PETERson and Lars R Furenlid. Spect detectors: the anger camera and beyond. *Physics in Medicine & Biology*, 56(17):R145, 2011.
- [9] Qingyang Wei, Shi Wang, Tianyu Ma, Lingjun Lu, Tiantian Dai, and Yaqiang Liu. Design of a high resolution phoswich pet detector. In *2011 IEEE Nuclear Science Symposium Conference Record*, pages 2874–2876. IEEE, 2011.

- [10] G Llosá. Sipm-based compton cameras. *Nuclear Instruments and Methods in Physics Research Section A: Accelerators, Spectrometers, Detectors and Associated Equipment*, 926:148–152, 2019.
- [11] Si Chen, Tianyu Ma, Feng He, Yaqiang Liu, and Shi Wang. A new compact gamma camera with super resolution capability and high sensitivity for monitoring sparse radioactive sources in large area. In *2013 IEEE Nuclear Science Symposium and Medical Imaging Conference (2013 NSS/MIC)*, pages 1–4. IEEE, 2013.
- [12] Wonho Lee and Taewoong Lee. 4π fov compact compton camera for nuclear material investigations. *Nuclear Instruments and Methods in Physics Research Section A: Accelerators, Spectrometers, Detectors and Associated Equipment*, 652(1):33–36, 2011.
- [13] A Nikitin and S Bliven. Needs of well logging industry in new nuclear detectors, iee nucl. In *Sci. Symp. Conf. Rec*, volume 1214, 2010.
- [14] PF Bloser, JS Legere, CM Bancroft, JM Ryan, and ML McConnell. Balloon flight test of a compton telescope based on scintillators with silicon photomultiplier readouts. *Nuclear Instruments and Methods in Physics Research Section A: Accelerators, Spectrometers, Detectors and Associated Equipment*, 812:92–103, 2016.
- [15] Antonio Ereditato, Martin Hierholzer, Marcello Messina, Martti Nirkko, Ciro Pistillo, Asmita Ajit Redij, and Biagio Rossi. Na61/shine facility at the cern sps: beams and detector system. *Journal of instrumentation*, 9:P06005, 2014.
- [16] N Blasi, A Giaz, C Boiano, S Brambilla, F Camera, B Million, and S Riboldi. Position sensitivity in large spectroscopic labr3: Ce crystals for doppler broadening correction. *Nuclear Instruments and Methods in Physics Research Section A: Accelerators, Spectrometers, Detectors and Associated Equipment*, 839:23–28, 2016.
- [17] MT Gericke, C Blessinger, JD Bowman, RC Gillis, J Hartfield, T Ino, M Leuschner, Y Masuda, GS Mitchell, S Muto, et al. A current mode detector array for γ -ray asymmetry measurements. *Nuclear Instruments and Methods in Physics Research Section A: Accelerators, Spectrometers, Detectors and Associated Equipment*, 540(2-3):328–347, 2005.
- [18] Euclid Seeram. Digital mammography: an overview. *Canadian Journal of Medical Radiation Technology*, 36(4):15–23, 2005.
- [19] M Kagaya, H Katagiri, R Enomoto, R Hanafusa, M Hosokawa, Y Itoh, H Muraishi, K Nakayama, K Satoh, T Takeda, et al. Development of a low-cost-high-sensitivity compton camera using csi (tl) scintillators (γ i). *Nuclear Instruments and Methods in Physics Research Section A: Accelerators, Spectrometers, Detectors and Associated Equipment*, 804:25–32, 2015.

- [20] Manhee Jeong, Benjamin Van, Byron T Wells, Lawrence J D'Aries, and Mark D Hammig. Scalable gamma-ray camera for wide-area search based on silicon photomultipliers array. *Review of Scientific Instruments*, 89(3):033106, 2018.
- [21] C Aa Diget, SP Fox, A Smith, S Williams, M Porter-Peden, L Achouri, P Adsley, H Al-Falou, RAE Austin, GC Ball, et al. Sharc: Silicon highly-segmented array for reactions and coulex used in conjunction with the tigris γ -ray spectrometer. *Journal of Instrumentation*, 6(02):P02005, 2011.
- [22] S Paschalis, IY Lee, AO Macchiavelli, CM Campbell, M Cromaz, S Gros, J Pavan, J Qian, RM Clark, HL Crawford, et al. The performance of the gamma-ray energy tracking in-beam nuclear array gretina. *Nuclear Instruments and Methods in Physics Research Section A: Accelerators, Spectrometers, Detectors and Associated Equipment*, 709:44–55, 2013.
- [23] H Suzuki, S Nakamura, M Hirayanagi, S Adachi, T Uchiyama, S Ohsuka, K Nakamoto, J Kataoka, T Nishiyama, T Fujita, et al. Gamma-ray visualization module. In *2013 IEEE Nuclear Science Symposium and Medical Imaging Conference (2013 NSS/MIC)*, pages 1–3. IEEE, 2013.
- [24] Naoko Inadama, Yoshiyuki Hirano, Fumihiko Nishikido, Hideo Murayama, and Taiga Yamaya. Development of a doi pet detector having the structure of the x'tal cube extended in one direction. *IEEE Transactions on Nuclear Science*, 63(5):2509–2516, 2016.
- [25] Herman T Van Dam, Stefan Seifert, Ruud Vinke, PETER Dendooven, Herbert Löhner, Freek J Beekman, and Dennis R Schaart. A practical method for depth of interaction determination in monolithic scintillator pet detectors. *Physics in Medicine & Biology*, 56(13):4135, 2011.
- [26] Radosław Marcinkowski, Pieter Mollet, Roel Van Holen, and Stefaan Vandenberghe. Sub-millimetre doi detector based on monolithic lyso and digital sipm for a dedicated small-animal pet system. *Physics in Medicine & Biology*, 61(5):2196, 2016.
- [27] Hal O Anger. Scintillation camera. *Review of scientific instruments*, 29(1):27–33, 1958.
- [28] Hal O Anger. Sensitivity, resolution, and linearity of the scintillation camera. *IEEE Transactions on nuclear science*, 13(3):380–392, 1966.
- [29] Zhonghua Kuang, Xiaohui Wang, Xin Fu, Ning Ren, Qian Yang, Binqing Zhao, Chunhui Zhang, San Wu, Ziru Sang, Zhanli Hu, et al. Dual-ended readout small animal pet detector by using 0.5 mm pixelated lyso crystal arrays and sipms. *Nuclear Instruments and Methods in Physics Research Section A: Accelerators, Spectrometers, Detectors and Associated Equipment*, 917:1–8, 2019.

- [30] K Doroud, Z Liu, and MCS Williams. A new geometry of scintillating crystals with strip sipms: a pet detector with precise position and time determination. *Journal of Instrumentation*, 14(01):P01016, 2019.
- [31] Matteo Morrocchi, Giovanni Ambrosi, Maria Giuseppina Bisogni, Filippo Bosi, Marco Boretto, Piergiorgio Cerello, Maria Ionica, Ben Liu, Francesco Pennazio, Maria Antonietta Piliero, et al. Depth of interaction determination in monolithic scintillator with double side sipm readout. *EJNMMI physics*, 4(1):1–25, 2017.
- [32] Ch W Lerche, JM Benloch, F Sánchez, N Pavón, N Gimenez, M Fernández, M Giménez, A Sebastiá, J Martínez, and FJ Mora. Depth of interaction detection with enhanced position-sensitive proportional resistor network. *Nuclear Instruments and Methods in Physics Research Section A: Accelerators, Spectrometers, Detectors and Associated Equipment*, 537(1-2):326–330, 2005.
- [33] Zhi Li, M Wedrowski, P Bruyndonckx, and G Vandersteen. Nonlinear least-squares modeling of 3d interaction position in a monolithic scintillator block. *Physics in Medicine & Biology*, 55(21):6515, 2010.
- [34] Alexei Ulyanov, Oran Morris, Lorraine Hanlon, Sheila McBreen, Suzanne Foley, Oliver J Roberts, Isaac Tobin, David Murphy, Colin Wade, Nick Nelms, et al. Performance of a monolithic labr3: Ce crystal coupled to an array of silicon photomultipliers. *Nuclear Instruments and Methods in Physics Research Section A: Accelerators, Spectrometers, Detectors and Associated Equipment*, 810:107–119, 2016.
- [35] Florian Müller, David Schug, Patrick Hallen, Jan Grahe, and Volkmar Schulz. A novel doi positioning algorithm for monolithic scintillator crystals in pet based on gradient tree boosting. *IEEE Transactions on Radiation and Plasma Medical Sciences*, 3(4):465–474, 2018.
- [36] Amirhossein Sanaat and Habib Zaidi. Depth of interaction estimation in a preclinical pet scanner equipped with monolithic crystals coupled to sipms using a deep neural network. *Applied Sciences*, 10(14):4753, 2020.
- [37] P Bruyndonckx, S Leonard, C Lemaitre, S Tavernier, and Y Wu. Performance study of a pet detector module based on a continuous scintillator. *IEEE transactions on nuclear science*, 53(5):2536–2542, 2006.
- [38] T Ling, TK Lewellen, and RS Miyaoka. Depth of interaction decoding of a continuous crystal detector module. *Physics in Medicine & Biology*, 52(8):2213, 2007.
- [39] Silvia Liprandi, Michael Mayerhofer, Saad Aldawood, Tim Binder, George Dedes, Agnese Miani, Dennis R Schaart, Ingrid I Valencia Lozano, Katia Parodi, and Peter G Thirolf. Sub-3mm spatial resolution from a large monolithic labr3 (ce) scintillator. *Current Directions in Biomedical Engineering*, 3(2):655–659, 2017.

- [40] Ch W Lerche, Michael Döring, Ana Ros, V Herrero, Rafael Gadea, RJ Aliaga, Ricardo Colom, F Mateo, JM Monzó, Néstor Ferrando, et al. Depth of interaction detection for γ -ray imaging. *Nuclear Instruments and Methods in Physics Research Section A: Accelerators, Spectrometers, Detectors and Associated Equipment*, 600(3):624–634, 2009.
- [41] R Pani, S Nourbakhsh, P Pani, P Bennati, R Pellegrini, MN Cinti, R Scaf e, B Cassano, F Navarria, S Lo Meo, et al. Doi position resolution in a continuous labr3 (ce) scintillation crystal for γ -ray imaging. *Nuclear Physics B-Proceedings Supplements*, 215(1):324–327, 2011.
- [42] Roberto Pani, Marco Bettiol, Enrico Preziosi, Cristian Borrazzo, Rosanna Pellegrini, Antonio J Gonz alez, Pablo Conde, Maria Nerina Cinti, Andrea Fabbri, Elisabetta Di Castro, et al. A novel method for γ -photons depth-of-interaction detection in monolithic scintillation crystals. *IEEE Transactions on Nuclear Science*, 63(5):2487–2495, 2016.
- [43] Alberto Del Guerra, Nicola Belcari, and M Bisogni. Positron emission tomography: its 65 years. *La Rivista del Nuovo Cimento*, 39:155–223, 2016.
- [44] Marc AN Korevaar, Jan WT Heemskerk, Marlies C Goorden, and Freek J Beekman. Multi-scale algorithm for improved scintillation detection in a ccd-based gamma camera. *Physics in Medicine & Biology*, 54(4):831, 2009.
- [45] D Brillantino, T Ferro, C Brillantino, E Rossi, R Minelli, E Bignardi, A Tufano, R Zeccolini, and M Zeccolini. Clinical pharmacology, use, and adverse reactions of intravenous iodinated contrast media in computed tomography. *J Radiol Imaging*, 4(1):1–6, 2020.
- [46] William R Leo. *Techniques for nuclear and particle physics experiments: a how-to approach*. Springer Science & Business Media, 2012.
- [47] Radioisotopes and Radiation Methodology. https://science.mcmaster.ca/radgrad/images/6R06CourseResources/4R6Notes4_ScintillationDetectors.pdf. Accessed June 19, 2020.
- [48] SCIONIX. <https://scionix.nl/scintillation-crystals/#tab-id-9>. Accessed April 19, 2020.
- [49] Nikola Vukašinović, Drago Bračun, Janez Možina, and Jože Duhovnik. The influence of incident angle, object colour and distance on cnc laser scanning. *The International Journal of Advanced Manufacturing Technology*, 50(1-4):265–274, 2010.
- [50] John R Quinn. Development of a pattern recognition approach for analyzing flow cytometric data. 2006.
- [51] Roger Lecomte. Novel detector technology for clinical pet. *European journal of nuclear medicine and molecular imaging*, 36(1):69–85, 2009.

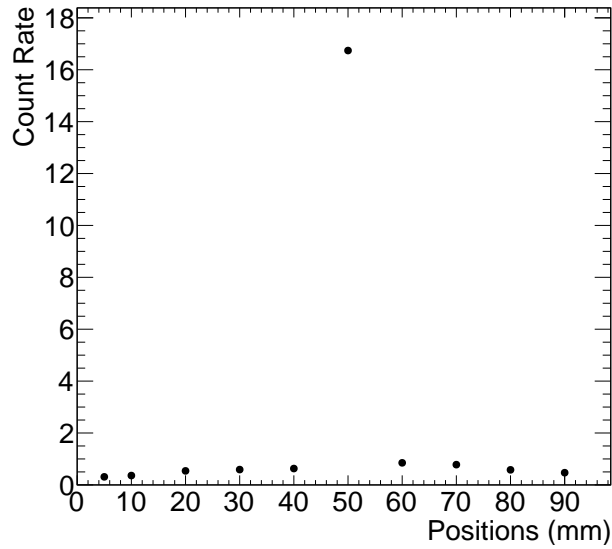
- [52] NL Christensen, Bruce E Hammer, BG Heil, and K Fetterly. Positron emission tomography within a magnetic field using photomultiplier tubes and light-guides. *Physics in Medicine & Biology*, 40(4):691, 1995.
- [53] Difference between pn junction diode and photo diode. <https://www.polytechnichub.com/wp-content/uploads/2017/04/P-N-Junction-Diode.jpg>. Accessed June 26, 2020.
- [54] Tom K Lewellen. Recent developments in pet detector technology. *Physics in Medicine & Biology*, 53(17):R287, 2008.
- [55] Giancarlo Barbarino, Riccardo De Asmundis, Gianfranca De Rosa, Carlos Maximiliano Mollo, Stefano Russo, and Daniele Vivolo. Silicon photo multipliers detectors operating in geiger regime: an unlimited device for future applications. In *Photodiodes- World Activities in 2011*. InTechOpen, 2011.
- [56] Azosensors.com. <https://www.azosensors.com/article.aspx?ArticleID=865>. Accessed October 7, 2020.
- [57] An introduction to the silicon photomultiplier. <https://www.sensl.com/downloads/ds/TN%20-%20Intro%20to%20SPM%20Tech.pdf>. Accessed June 26, 2020.
- [58] P Buzhan, B Dolgoshein, L Filatov, A Ilyin, V Kantzerov, V Kaplin, A Karakash, F Kayumov, S Klemin, E Popova, et al. Silicon photomultiplier and its possible applications. *Nuclear Instruments and Methods in Physics Research Section A: Accelerators, Spectrometers, Detectors and Associated Equipment*, 504(1-3):48–52, 2003.
- [59] Caen nuclear physics. https://www.caen.it/documents/News/20/WP2081_DigitalPulseProcessing_Rev_2.1.pdf. Accessed October 10, 2020.
- [60] F. J. Ramírez-Jiménez. X-Ray Spectroscopy with PIN diodes. In Adnan Bashir, Victor Villanueva, and Luis Villaseqor, editors, *Particles and Fields: X Mexican Workshop*, volume 857 of *American Institute of Physics Conference Series*, pages 121–133, September 2006.
- [61] M Moszynski. Energy resolution of scintillation detectors. In *Hard X-Ray and Gamma-Ray Detector Physics VII*, volume 5922, page 592205. International Society for Optics and Photonics, 2005.
- [62] C-series low noise, blue-sensitive silicon photomultipliers. <http://sensl.com/downloads/ds/DS-MicroCseries.pdf>. Accessed April, 2018.
- [63] Arrayj,user manual. <http://sensl.com/downloads/ds/UM-ArrayTSV.pdf>. Accessed 2 November, 2019.
- [64] Febex3b, specification. <https://www.gsi.de/fileadmin/EE/Module/FEBEX/febex3b.pdf>. Accessed 16 March, 2019.

- [65] Exploder3, preliminary specification. https://www.gsi.de/fileadmin/EE/Module/EXPLODER/exploder3_v4.pdf. Accessed 30 July 2019.
- [66] The general purpose data acquisition system mbs at gsi. <https://indico.cern.ch/event/617177/attachments/1424870/2185375/mbs-febex.pdf>. Accessed 20 July 2019.
- [67] H Gotoh and H Yagi. Solid angle subtended by a rectangular slit. *Nuclear Instruments and Methods*, 96(3):485–486, 1971.
- [68] Sea Agostinelli, John Allison, K al Amako, John Apostolakis, H Araujo, P Arce, M Asai, D Axen, S Banerjee, G 2 Barrand, et al. Geant4—a simulation toolkit. *Nuclear instruments and methods in physics research section A: Accelerators, Spectrometers, Detectors and Associated Equipment*, 506(3):250–303, 2003.
- [69] Alexei Ulyanov, Oran Morris, Oliver J Roberts, Isaac Tobin, Lorraine Hanlon, Sheila McBreen, David Murphy, Nick Nelms, and Brian Shortt. Localisation of gamma-ray interaction points in thick monolithic cebr3 and labr3: Ce scintillators. *Nuclear Instruments and Methods in Physics Research Section A: Accelerators, Spectrometers, Detectors and Associated Equipment*, 844:81–89, 2017.
- [70] John Allison, Katsuya Amako, JEA Apostolakis, HAAH Araujo, P Arce Dubois, MAAM Asai, GABG Barrand, RACR Capra, SACS Chauvie, RACR Chytracek, et al. Geant4 developments and applications. *IEEE Transactions on nuclear science*, 53(1):270–278, 2006.
- [71] Jenny Nilsson, Vesna Cuplov, and Mats Isaksson. Identifying key surface parameters for optical photon transport in geant4/gate simulations. *Applied radiation and isotopes : including data, instrumentation and methods for use in agriculture, industry and medicine*, 103:15–24, September 2015.
- [72] Book for application developers. <https://geant4-userdoc.web.cern.ch/UsersGuides/ForApplicationDeveloper/html/>. Accessed February 2, 2018.
- [73] Viking cluster - IT Services, University of York. <http://www.york.ac.uk/it-services/research-computing/viking-cluster/>. Accessed June 27, 2020.
- [74] Jae Hyeon Kim, Young-Su Kim, Hyun Su Lee, Hee Seo, and Chan Hyeong Kim. Optimization of dpc dsipm-based doi compton camera by monte carlo simulation. *IEEE Transactions on Nuclear Science*, 65(7):1424–1431, 2018.
- [75] Saad Aldawood, Ines Castelhana, Roman Gernhäuser, Hugh Van Der Kolff, Christian Lang, Silvia Liprandi, Rudolf Lutter, Ludwig Maier, Tim Marinšek, Dennis R Schaart, et al. Comparative characterization study of a labr3 (ce) scintillation crystal in two surface wrapping scenarios: Absorptive and reflective. *Frontiers in oncology*, 5:270, 2015.

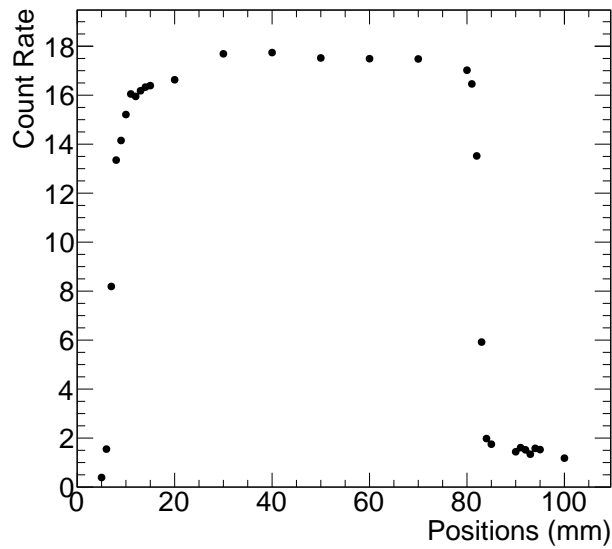
- [76] Rita Ricci, Theodora Kostou, Konstantinos Chatzipapas, Eleftherios Fysikopoulos, George Loudos, Luigi Montalto, Lorenzo Scalise, Daniele Rinaldi, and Stratos David. Monte carlo optical simulations of a small fov gamma camera. effect of scintillator thicknesses and septa materials. *Crystals*, 9(8):398, 2019.
- [77] Yuan-Chuan Tai, Andrew L Goertzen, et al. Use of systematic surface roughing to enhance the spatial resolution of the dual-ended readout of axially-oriented 100 mm long lyso crystals. *Physics in Medicine & Biology*, 57(24):N501, 2012.
- [78] Silin Ren, Yongfeng Yang, and Simon R Cherry. Effects of reflector and crystal surface on the performance of a depth-encoding pet detector with dual-ended readout. *Medical Physics*, 41(7):072503, 2014.
- [79] Chad Bircher and Yiping Shao. Investigation of crystal surface finish and geometry on single lyso scintillator detector performance for depth-of-interaction measurement with silicon photomultipliers. *Nuclear Instruments and Methods in Physics Research Section A: Accelerators, Spectrometers, Detectors and Associated Equipment*, 693:236–243, 2012.
- [80] Victor Babiano, Luis Caballero, David Calvo, Ion Ladarescu, Pablo Olleros, and César Domingo-Pardo. γ -ray position reconstruction in large monolithic lacl3 (ce) crystals with sipm readout. *Nuclear Instruments and Methods in Physics Research Section A: Accelerators, Spectrometers, Detectors and Associated Equipment*, 931:1–22, 2019.
- [81] A Iborra, AJ González, A González-Montoro, A Bousse, and Dimitris Visvikis. Ensemble of neural networks for 3d position estimation in monolithic pet detectors. *Physics in Medicine & Biology*, 64(19):195010, 2019.
- [82] Wen He, Xianchao Huang, Yingjie Wang, Baotong Feng, Meiling Zhu, Shuangquan Liu, Zhiming Zhang, and Long Wei. A preliminary study on 3d position reconstruction of monolithic crystal readout. *Radiation Detection Technology and Methods*, pages 1–8, 2020.
- [83] Matteo Morrocchi, Giovanni Ambrosi, Maria Giuseppina Bisogni, Piergiorgio Cerello, Francesco Corsi, Maria Ionica, Naema Marino, Cristoforo Marzocca, Francesco Pennazio, Giovanni Pirrone, et al. Development of a pet detector module with depth of interaction capability. *Nuclear Instruments and Methods in Physics Research Section A: Accelerators, Spectrometers, Detectors and Associated Equipment*, 732:603–606, 2013.
- [84] Akihisa Omata, Jun Kataoka, Kazuya Fujieda, Shogo Sato, Eri Kuriyama, Hiroki Kato, Atsushi Toyoshima, Takahiro Teramoto, Kazuhiro Ooe, Yuwei Liu, et al. Performance demonstration of a hybrid compton camera with an active pinhole for wide-band x-ray and gamma-ray imaging. *Scientific Reports*, 10(1):1–9, 2020.

- [85] Qing Ye, Peng Fan, Rui Wang, Zhenlei Lyu, Ankang Hu, Qingyang Wei, Yan Xia, Rutao Yao, Yaqiang Liu, and Tianyu Ma. A high sensitivity 4π view gamma imager with a monolithic 3d position-sensitive detector. *Nuclear Instruments and Methods in Physics Research Section A: Accelerators, Spectrometers, Detectors and Associated Equipment*, 937:31–40, 2019.
- [86] Hiroki Hosokoshi, Jun Kataoka, Saku Mochizuki, Masaki Yoneyama, Soichiro Ito, Hiroaki Kiji, Fumiya Nishi, Shuji Miyamoto, and Tatsushi Shima. Development and performance verification of a 3-d position-sensitive compton camera for imaging mev gamma rays. *Scientific Reports*, 9(1):1–9, 2019.

Appendix A



(a)



(b)

Figure A.1: Images illustrating the 2D profiles obtained to find the beam position for the 1D detector in (a) the y and (b) the x axis. The detector was moved in 10 mm steps and the count rates were measured at different interaction positions and recorded

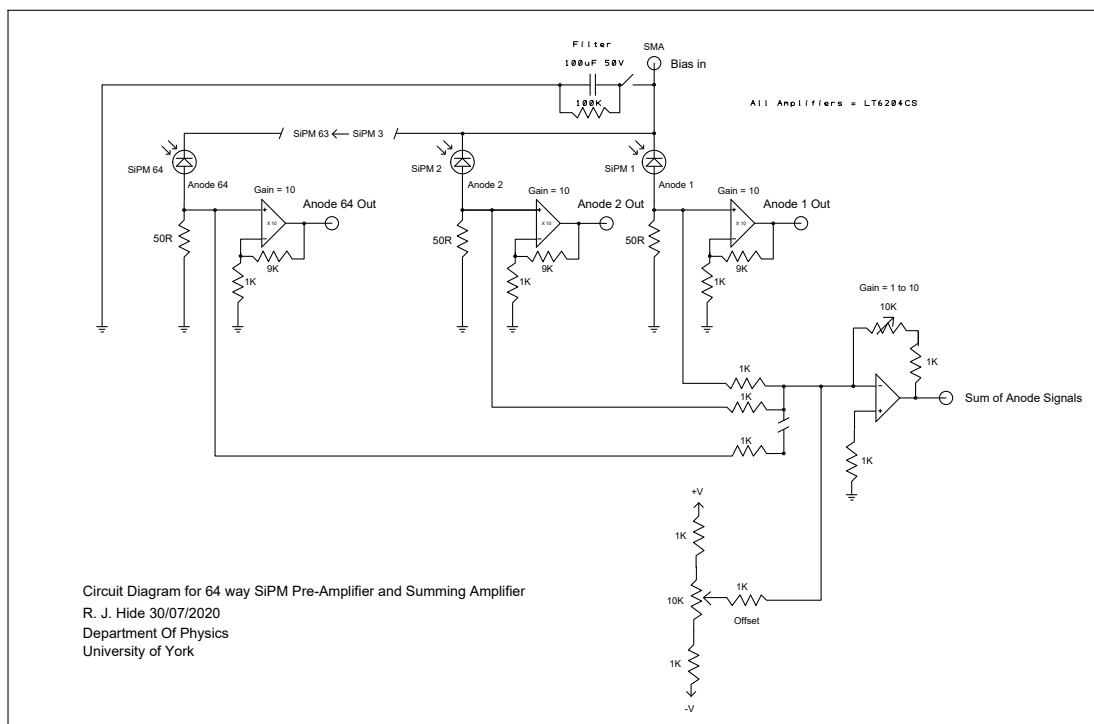


Figure A.2: Circuit Diagram for 64 way SiPM Pre-Amplifier and Summing Amplifier

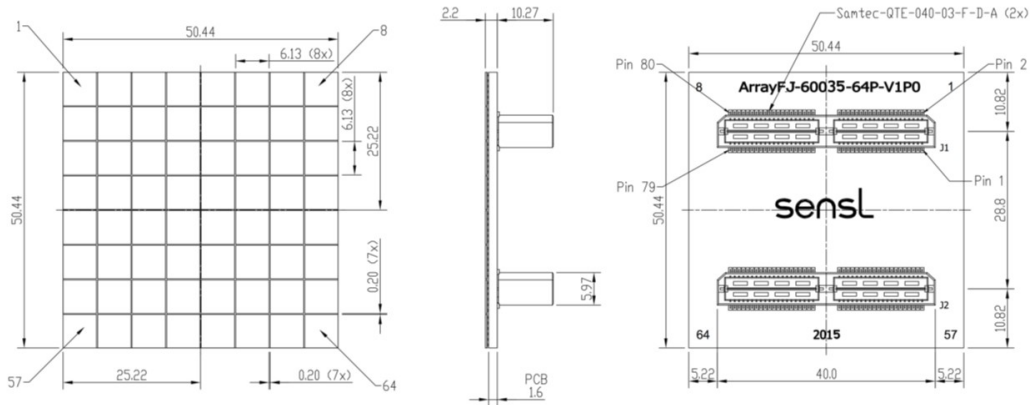


Figure A.3: Illustration of an 8×8 J-series array by Sensl. The diagram also shows the dimensions of each component of the array (front, side and back). Adapted from [63]

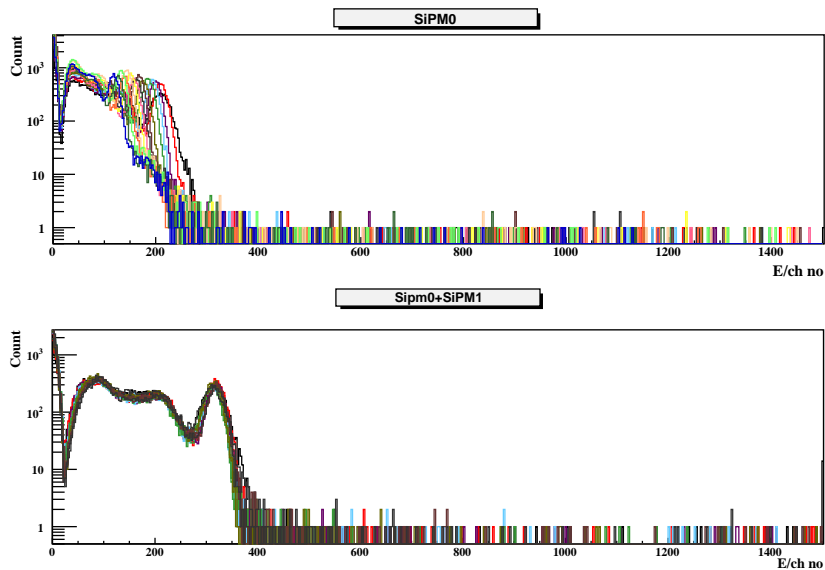


Figure A.4: An example of the spectra measured at one end of the black tape wrapped detector crystal (SiPM0,top) and the light measured by summing both SiPMs (SiPM0+SiPM1, bottom) at different illumination interaction points along the long-axis of the 1D detector. The different colours represent the different interaction point.

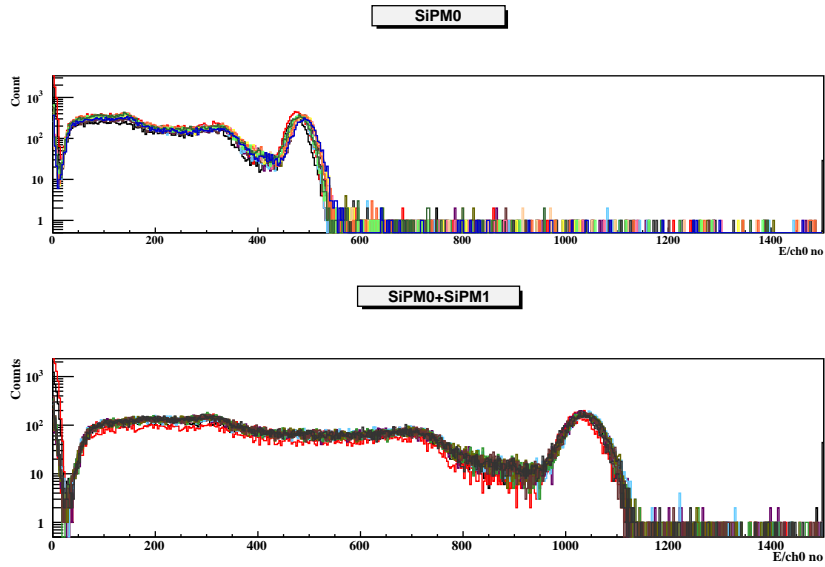


Figure A.5: An example of the spectra measured at one end of the 3M ESR wrapped detector crystal (SiPM0,top) and the light measured by summing both SiPMs (SiPM0+SiPM1, bottom)at different illumination interaction points along the long-axis of the 1D detector.The different colours represent the different interaction point

x	y	z	x+z	# of simulated events	# of coincidence events	# of single events %
5	5	5	10	539912	380570	70
5	25	5	10	546728	379608	69
5	45	5	10	540025	380496	70
5	5	25	30	364898	235752	65
5	25	25	30	379302	233844	62
5	45	25	30	365084	235708	65
25	5	5	30	136165	79445	58
25	25	5	30	138602	77571	56
25	45	5	30	136059	79269	58
5	5	45	50	193629	116839	60
5	25	45	50	204152	116198	57
5	45	45	50	193416	116768	60
25	5	25	50	115775	50354	43
25	25	25	50	125977	47254	38
25	45	25	50	116026	50373	43
45	5	5	50	35050	18106	52
45	25	5	50	33276	16316	49
45	45	5	50	34793	17972	52
25	5	45	70	73731	27261	37
25	25	45	70	83024	25646	31
25	45	45	70	73764	27124	37
45	5	25	70	37000	12780	35
45	25	25	70	37966	10304	27
45	45	25	70	36877	12781	35
45	5	45	90	28174	7898	28
45	25	45	90	30951	6299	20
45	45	45	90	28058	7813	28

Figure A.6: Number/Percentage of single coincidence events in the simulation. A longer path through the detector ($x+z$) leads to more multiple scattering events.